AEDC-TR-05-1

Facility Unsteadiness Research
Final Report

Dr. Christopher C. Nelson
Innovative Technology Applications Company
P.O. Box 6971
Chesterfield, MO 63006-6971

November 2004

Final Report for Period February 2002 — September 2004

ARNOLD ENGINEERING DEVELOPMENT CENTER
ARNOLD AIR FORCE BASE, TENNESSEE
AIR FORCE MATERIEL COMMAND
UNITED STATES AIR FORCE

DESTRUCTION NOTICE

For unclassified documents, destroy by any method that will prevent disclosure or reconstruction of the document.
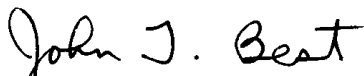
APPROVAL STATEMENT

This report has been reviewed and approved.

STEVEN A. BANCROFT
Applied Technology Division
Operations Directorate

Approved for publication:

FOR THE COMMANDER

JOHN T. BEST
Director, Applied Technology Division
Operations Directorate

1. REPORT DATE *(DD-MM-YYYY)* 00-11-2004	2. REPORT TYPE Final	3. DATES COVERED *(From – To)* February 2002-September 2004	
4. TITLE AND SUBTITLE Facility Unsteadiness Research Final Report		**5a. CONTRACT NUMBER** ATA-03-034	
		5b. GRANT NUMBER	
		5c. PROGRAM ELEMENT NUMBER 61102F	
6. AUTHOR(S) Dr. Christopher C. Nelson		**5d. PROJECT NUMBER** 00009828	
		5e. TASK NUMBER	
		5f. WORK UNIT NUMBER	
7. PERFORMING ORGANIZATION NAME(S) AND ADDRESS(ES) Arnold Engineering Development Center/DOT 1099 Avenue C Arnold Air Force Base, TN 37389-9011 Innovative Technology Applications Company PO Box 6971 Chesterfield, MO 63006-6971		**8. PERFORMING ORGANIZATION REPORT NO.** AEDC-TR-05-1	
9. SPONSORING/MONITORING AGENCY NAME(S) AND ADDRESS(ES) Neal Glassman Air Force Office of Scientific Research 4015 Wilson Boulevard, Room 713 Arlington, VA 22203-1954		**10. SPONSOR/MONITOR'S ACRONYM(S)** AFOSR	
		11. SPONSOR/MONITOR'S REPORT NUMBER(S)	

12. DISTRIBUTION/AVAILABILITY STATEMENT
STATEMENT A: Approved for public release; distribution unlimited.

13. SUPPLEMENTARY NOTES
Available in the Defense Technical Information Center (DTIC).

14. ABSTRACT
This report summarizes work that was performed in fiscal years 2002 through 2004 on or related to the "Facility Unsteadiness Research" project sponsored by the Air Force Office of Scientific Research (AFOSR). Many ground test facilities experience some form of flow unsteadiness at various points in their operational envelope. This unsteadiness can at times cause significant problems in the quality of data obtained, the structural integrity of the facility, or both. Conventional simulation techniques, which do quite well for steady-state simulations, have been found to be deficient in many cases when applied to unsteady flows. The current project attempts to address these problems. This work has focused on three areas: building up the computational infrastructure of a production CFD code to be able to tackle large scale unsteady problems, developing a rigorous code verification capability in order to ensure continued reliability of the results in the face of extensive code modification, and the running of test cases leading toward the ultimate objective of being able to simulate full scale facilities. The Detached Eddy Simulation model and the hybrid model of Nichols and Nelson were found to offer improved results over conventional turbulence models for unsteady flows. The Method of Manufactured Solutions was employed to verify several of the numerical methods available in the Wind-US code. The algorithm improvements to the Wind-US code have now made it possible to begin to model large ground test facilities and resolve medium and large-scale instabilities within them.

15. SUBJECT TERMS
unsteady turbulence modeling, Navier-Stokes, Detached Eddy Simulation, ground test facility, method of manufactured solutions

16. SECURITY CLASSIFICATION OF:			17. LIMITATION OF ABSTRACT	18. NUMBER OF PAGES	19a. NAME OF RESPONSIBLE PERSON
a. REPORT	b. ABSTRACT	c. THIS PAGE			Steve Bancroft
U	U	U	SAR	140	19b. TELEPHONE NUMBER *(Include area code)* 931-454-6418

Abstract

This report summarizes work that was performed in fiscal years 2002 through 2004 on or related to the "Facility Unsteadiness Research" project sponsored by the Air Force Office of Scientific Research (AFOSR). Many ground test facilities experience some form of flow unsteadiness at various points in their operational envelope. This unsteadiness can at times cause significant problems in the quality of data obtained, the structural integrity of the facility, or both. Conventional simulation techniques, which do quite well for steady-state simulations, have been found to be deficient in many cases when applied to unsteady flows. The current project attempts to address these problems. This work has focused on three areas: building up the computational infrastructure of a production CFD code to be able to tackle large scale unsteady problems, developing a rigorous code verification capability in order to ensure continued reliability of the results in the face of extensive code modification, and the running of test cases leading toward the ultimate objective of being able to simulate full scale facilities. The Detached Eddy Simulation model and the hybrid model of Nichols and Nelson were found to offer improved results over conventional turbulence models for unsteady flows. The Method of Manufactured Solutions was employed to verify several of the numerical methods available in the Wind-US code. The algorithm improvements to the Wind-US code have now made it possible to begin to model large ground test facilities and resolve medium and large-scale instabilities within them.

Contents

List of Tables

List of Figures

Chapter 1

Introduction

Currently, state of the art production CFD codes solve the Reynolds Averaged Navier-Stokes (RANS) equations using implicit schemes which are, typically, second order (or sometimes third) in space and first order (sometimes second) in time. Turbulent closure is typically obtained by using a one or two-equation model. This combination is generally quite successful for steady state simulations. As more unsteady simulations have been attempted, however, the limitations of the these codes have become apparent. The sources of difficulty can be broken into two basic categories: the numerical scheme employed, and the turbulence model. In order to be successful, the current project must address both issues.

In the area of of numerical scheme problems, the major limitation lies in the tendency of the methods used in production solvers to excessively dissipate the unsteady fluctuations in the flow. Furthermore, even when dissipation is within limits, dispersion errors may be significant, resulting in improper prediction of wave shapes and propagation speeds. Thus, the challenge is to find a scheme which is stable enough to be used in a production setting, but accurate enough to correctly propagate the unsteady disturbances from their source to the region of interest, which in a large facility may be hundreds of feet removed.

Turbulence model limitations typically arise because most production model were designed and calibrated for RANS solutions. Thus, by design, these schemes attempt to model all turbulent fluctuations, whatever the length or time scale. Obviously, in an unsteady simulation of a large scale test facility, some of the fluctuations which one would like to resolve are turbulent. Therefore, RANS models tend to be overly dissipative in these situations, resulting in an inability to accurately propagate the fluctuations in the flow. In recent years, several researchers have attempted to overcome this limitation by combining RANS turbulence models with Large Eddy Simulation (LES) models, using the former in regions where grid resolution is insufficient for capturing the unsteady fluctuations and the latter in denser portions of the flow domain. These models are finding increased application, but because their strengths, weaknesses, and failure modes have not been fully mapped, they are not yet generally used in production CFD environments.

The aforementioned shortcomings can be a substantial barrier to the successful

1

simulation of unsteady flows in ground test facilities. For example, the 16-S supersonic wind tunnel at AEDC has a known problem with oscillating flow angularity in the test section.

There is an ongoing effort to re-activate and upgrade the tunnel. Included in this effort are fixes addressing the flow quality problem. This required an understanding of the physics involved in the observed unsteadiness so as to be able to prevent/correct it in a reasonably efficient manner.

Because the capability to simulate the large-scale unsteadiness in a facility as sizable as the 16-S tunnel, the investigators working on the flow quality problem were forced to construct a subscale model of portions of the larger tunnel. While they believe that they have correctly identified the problem and have a solution for it, the process has been slow and expensive. It is believed that a capability to numerically simulate the facility could have saved much time and money, had it been available. The current work is an attempt to develop such a capability. The work encompassed several different (albeit related) areas: investigating two approaches to hybrid RANS/LES turbulence modeling, building up of code infrastructure to better handle unsteady flows, developing code verification capabilities, and running test cases to establish the ability of the code to capture the necessary physics. One of the decisions made early in this work was that a great deal of emphasis was to be placed on the transfer of the resulting technology into a production environment. For this reason, as well as the overall complexity of the problem being tackled, most of the work was performed using a modified production flow solver, rather than the more conventional (and simpler, if less flexible) research codes. Also, much of this work has been funded by sources other than AFOSR, but it is discussed here in relation to the Facility Unsteadiness Research project.

Chapter 2

Theory of Hybrid RANS/LES Turbulence Models

The first major thrust of the Facility Unsteadiness research project was to investigate two different approaches to hybrid RANS/LES turbulence modeling. The purpose was to begin to map the strengths and weaknesses of such methods, as well as gaining experience in running the particular models chosen.

Hybrid RANS/LES turbulence models can be approached theoretically in many ways. One way is to see them as derivatives of the multi-scale turbulence models developed by Hanjalic, Launder, and Schiestel[1], Kim and Chen[2], and Duncan and Liou[3]. These turbulence models all have the form

$$\frac{\partial k_p}{\partial t} + u_j \frac{\partial k_p}{\partial x_j} - \frac{\partial}{\partial x_j} \left(\left(\nu + \frac{\nu_t}{\sigma_{k_p}} \right) \frac{\partial k_p}{\partial x_j} \right) = P_r - \varepsilon_p \tag{2.1}$$

$$\frac{\partial \varepsilon_p}{\partial t} + u_j \frac{\partial \varepsilon_p}{\partial x_j} - \frac{\partial}{\partial x_j} \left(\left(\nu + \frac{\nu_t}{\sigma_{\varepsilon_p}} \right) \frac{\partial \varepsilon_p}{\partial x_j} \right) = c_{p_1} \frac{P_r^2}{k_p} - c_{p_3} \frac{\varepsilon_p^2}{k_p} \tag{2.2}$$

$$\frac{\partial k_t}{\partial t} + u_j \frac{\partial k_t}{\partial x_j} - \frac{\partial}{\partial x_j} \left(\left(\nu + \frac{\nu_t}{\sigma_{k_t}} \right) \frac{\partial k_t}{\partial x_j} \right) = \varepsilon_p - \varepsilon_t \tag{2.3}$$

$$\frac{\partial \varepsilon_t}{\partial t} + u_j \frac{\partial \varepsilon_t}{\partial x_j} - \frac{\partial}{\partial x_j} \left(\left(\nu + \frac{\nu_t}{\sigma_{\varepsilon_t}} \right) \frac{\partial \varepsilon_t}{\partial x_j} \right) = c_{t_1} \frac{\varepsilon_p^2}{k_t} - c_{t_3} \frac{\varepsilon_t^2}{k_t} \tag{2.4}$$

where

$$\nu_t = c_\mu \frac{(k_p + k_t)^2}{\varepsilon_p} \tag{2.5}$$

Equations 2.1 and 2.2 correspond to the large-scale turbulence. Equations 2.3 and 2.4 represent the smaller more dissipative turbulent scales. The large-scale dissipation, ε_p, is generally the same size as the small-scale dissipation, ε_t, for these multi-scale models. The large-scale turbulent kinetic energy, k_p, is generally an order of magnitude larger than the small-scale turbulent scale energy, k_t.

These equations suggest two possibilities for extension to unsteady flows. A first approach would be to solve equations 2.3 and 2.4 for the small-scale turbulent kinetic

energy (k_t). To implement this method, the source terms in equations 2.3 and 2.4 would require a blending function based on the filter function to allow them to be used when the turbulent length scale is below the grid resolution. This approach would also require some formulation for the large-scale dissipation ε_p. This approach could require a good deal of tuning to be applicable over a wide range of problems.

A second approach would be to solve equations 2.1 and 2.2 to find the large-scale turbulence parameters. The large-scale turbulent kinetic energy (k_p) could then be spatially filtered assuming that a relationship between turbulent kinetic energy and the turbulent length scale could be established. The eddy viscosity for the mean flow equations would then be calculated using Equation 2.5 with the filtered turbulent kinetic energy. This approach requires that the turbulence equations be solved with the unfiltered eddy viscosity and the mean flow equations be solved with the filtered value of eddy viscosity.

Both approaches have been applied to unsteady flows. One example of the first form is a Detached Eddy Simulation (DES) turbulence model based on the Spalart-Allmaras one-equation turbulence model[4] proposed by Spalart *et al.*[5]. The standard Spalart-Allmaras turbulence model contains a destruction term for eddy viscosity that is inversely proportional to the square of the distance from the wall (d). The hybrid version replaces the wall distance with

$$\widetilde{d} = \min\left(d, C_{DES}\Delta\right) \tag{2.6}$$

where C_{DES} is 0.65 and Δ is a characteristic grid length scale. The modified destruction term has the effect of decreasing the eddy viscosity in regions not in the immediate vicinity of walls. A similar modification to Menter's Shear Stress Transport Model (SST) two-equation model[6] was proposed by Strelets[7].

The model developed by Nichols and Nelson[8] uses the second approach discussed above. Equations are solved for the large scale turbulent parameters, and then an estimate is made as to how much of the turbulence is being resolved and how much must be modeled. In practice, the hybrid model is implemented by modifying the eddy viscosity:

$$\nu_t = \Lambda\nu_{t_{RANS}} + (1 - \Lambda)\nu_{t_{LES}} \tag{2.7}$$

In the above equation, $\nu_{t_{RANS}}$ is the standard eddy viscosity from the base RANS turbulence model. For the current work, both the Menter SST model[9] (RANS regime cases) and the Jones-Launder $k - \varepsilon$ model[10] (LES regime cases) have been adapted. The other eddy viscosity ($\nu_{t_{LES}}$) is computed based on a form taken from an LES k-equation model[11]:

$$\nu_{t_{LES}} = \min\left(c_{\mu_{LES}}\Delta\sqrt{k_{LES}}, \nu_{t_{RANS}}\right) \tag{2.8}$$

For the current work, a value of 0.0854 was used for the LES model coefficient ($c_{\mu_{LES}}$). The subgrid turbulent kinetic energy is defined as:

$$k_{LES} = f_d k_{RANS} \tag{2.9}$$

where the clipping function is defined as a function of the predicted turbulent length

4

scale and the local grid size:

$$f_d = \cfrac{1}{1 + \left(\frac{l_t}{2\Delta}\right)^{\frac{4}{3}}}$$
(2.10)

It should be noted that other implementations of this model (notably that in NXAIR) have the local grid spacing (Δ) rather than the local Nyquist wavelength (2Δ) in the denomenator of the above equation. This has the effect of increasing the effect of the LES component and decreasing the RANS component of the turbulent viscosity. The turbulent length scale used in this effort is defined by

$$l_t = \max\left(6\sqrt{\frac{\nu_{t_{RANS}}}{\omega}}, \frac{k_{RANS}^{\frac{3}{2}}}{\varepsilon_{RANS}}\right)$$
(2.11)

where ω is the local mean flow vorticity. This length scale is a mixture of the traditional turbulent scale definition for two-equation turbulence models ($k_{RANS}^{3/2}/\varepsilon_{RANS}$) and the definition usually associated with algebraic turbulence models ($\sqrt{\nu_t/\omega}$). The factor of six was chosen, such that the two components of the length scale were approximately equal in a simple test case. This turbulent length scale definition could be easily adapted to other types of turbulence models. The cut-over function (Λ) is defined as:

$$\Lambda = \frac{1}{2}\left(1 + \tanh\left(2\pi\left(f_d - \frac{1}{2}\right)\right)\right)$$
(2.12)

In practical terms, then, the approach that Nichols and Nelson have taken in developing the hybrid model for unsteady turbulent flows can be described as filtering the RANS turbulence models such that the eddy viscosity does not include the energy of grid-resolved turbulent scales. Therefore, the filtered RANS turbulence model may be thought of as a subgrid model for very large turbulent eddies. The objective in choosing this filter is that it should not degrade the performance of the turbulence model when the largest turbulent scales present are below the resolution of the grid, as is generally the case in current aircraft CFD applications–certainly the case near viscous walls and often so elsewhere. This approach should be viable for the current class of CFD flow solvers and would not require any more grid resolution than the time averaged CFD grids used currently except in areas where finer details of the instantaneous flow structures are desired.

As a final note on hybrid model theory, it should be pointed out that others take widely different views of hybrid models and the theory, if any, behind them. Durbin[12], for example, sees problems with the DES model (and others like it) because "there is an influence of the ensemble on the instantaneous, which could not really happen." At the same conference where Durbin's aforementioned ideas were presented, the DES model was described by Piomelli and Gatski (in the question-and-answer period following a presentation by Piomelli[13]) as being an LES model that has a simple wall model based on a RANS turbulence model. Thus, while there may be (and the current work has found) practical benefits to the hybrid approach, as of this writing there is no broad consensus as to its theoretical basis.

Chapter 3

Evaluation of Hybrid RANS/LES Turbulence Models Using an LES Code

3.1 Introduction

The numerical schemes commonly used in production flow solvers are relatively dissipative, and many such schemes have themselves been found to act much like a turbulence model (this observation being the basis of "monotone implicit LES"–aka "MILES"). This complicates the task of analyzing the effect of a given turbulence model since it is not always a straightforward process to determine how much of what is observed comes from the numerical scheme and how much comes from the turbulence model. The purpose of the work presented in this chapter is to investigate hybrid turbulence models, comparing them to both conventional RANS models and LES models in the context of a code designed for LES. The numerical scheme used in this code has comparatively little dissipation (relative to production RANS codes); therefore, the effects of the various turbulence models should be more clearly shown.

The immediate benefit to the Facility Unsteadiness Research project is a clearer understanding of the strength's and weaknesses of the various models when operating in LES mode. If this segment of the operating envelope is not well handled, the prospects for successful simulations of large scale facilities would be relatively dim. Fortunately, as will be shown, these models have been found to perform surprisingly well. Performance when the configuration is more in the RANS range will be discussed in a later chapter.

3.2 Description of the Turbulence Models

The two hybrid turbulence models discussed in the previous chapter have been investigated: a hybrid $k - \varepsilon$ model using the approach from Nichols and Nelson [14] and

Table 3.1: Flow Parameters for Spatial Mixing-Layer Case

T_0, K	P_{0_1}, kPa	M_1	M_2	M_c	U_1, m/s	$\frac{U_2}{U_1}$	$\frac{\rho_2}{\rho_1}$	δ_1, mm
291.0	314.0	1.80	0.51	0.52	479.5	0.355	0.638	8.0

the DES model of Spalart[5]. For comparison, results are presented using the RANS models upon which the two hybrid models are based: the Jones-Launder $k - \varepsilon$ model [10] (with compressibility correction [15]) and the Spalart-Allmaras model [4]. Finally, three LES models have been run: the Smagorinsky model (as implemented by Hixon[16]) and two versions of a k-equation model–one with constant coefficients and another, dynamic coefficient version[11]. An attempt was made to run without any explicit turbulence model (as in MILES), but the code was not stable under these conditions, and the attempt was unsuccessful. This is not surprising, since the scheme is not monotone and is therefore inappropriate for a MILES approach.

3.3 Description of the Test Case

The test case used to evaluate the models was based on the mixing-layer experiments of Samimy and Elliot[17]: a two-stream planar mixing layer, with one stream supersonic and the other subsonic. Experimental data were available at various locations between the trailing edge of the splitter plate and 210 mm downstream from there. The domain of the simulations included a short length of splitter plate and extended over 600 mm downstream. Only the middle 75 mm of the experimental rig (out of 150 mm) was simulated. Since the side walls were not being modeled, periodic boundary conditions were employed in the spanwise direction. This approach had two principal advantages. First, it removed any need for injecting artificial turbulence at these boundaries (when flow entered the domain through them). Second, it permitted the use of spanwise averaging to decrease the simulation time required to achieve statistical steady state (estimated at five to ten times faster than without averaging).

The flow parameters for this case are given in Table 3.1. In the table, the subscript numbers 1 and 2 refer to the high- and low-speed streams, respectively, and δ_1 refers to the boundary-layer thickness at the end of the splitter plate on the high-speed side. Results from three grid resolutions are presented here: $81 \times 61 \times 34$, $141 \times 91 \times 50$, and $181 \times 121 \times 66$. At the finest grid resolution, this provided about thirty points across the mixing layer at the 210 mm station. A pseudo-turbulent fluctuation field was added at the incoming boundaries to better match the experimental conditions.The solutions were run for 30,000 time steps to wash initial transients out of the region of interest. Then statistics were taken over 60,000 further steps. As mentioned above, since transverse boundary conditions were periodic (making this a homogeneous flow direction), spatial averaging was used to achieve statistically steady-state results relatively quickly. The time step for all cases was 5.0×10^{-8} seconds.

The code employed for this work uses an explicit MacCormack-type predictor-

Table 3.2: Mixing Layer Growth Rate Predicted by Various Turbulence Models

	$\left(\frac{db}{dx}\right)_i$	Exp.	Smag.	k-eqn.	Dyn. k	Hybrid	DES	$k-\varepsilon$	Spalart
db/dx	0.0742	0.0802	0.0547	0.0576	0.0578	0.0610	0.0585	0.0318	0.0476
$\frac{db/dx}{(db/dx)_i}$	1	1.080	0.737	0.776	0.779	0.822	0.788	0.429	0.642

corrector scheme that is fourth order in space (on Cartesian grids) and second order in time. Additional details on the geometry, statistical methods (including sampling procedures), and numerical methods may be found in Nelson[18]. Note, however, that the domain of the previous simulations did not extend as far either upstream or downstream as does this study. The extended computational domain was included because studies of the effect of boundary location (not presented here) for the current work indicated that it improved results somewhat. Also note that the current work uses the conventional Favre-averaged LES governing equations, while the previous work did not. In other respects, the techniques used are much the same.

3.4   Results

The results presented here are split into three categories. First, a general survey of the behavior of the various models is presented. Next, a study of the effects of grid resolution on the results from the hybrid models is presented (this doubles as a grid convergence study). Finally, the self-similarity predicted by the hybrid models is examined.

The variables shown in the plots are now defined. The non-dimensional streamwise velocity is defined as follows:

$$U^* = \frac{\overline{u} - U_2}{U_1 - U_2} \tag{3.1}$$

where $\overline{u}$ represents the time-averaged velocity in the streamwise direction and U_1 and U_2 are the freestream velocities of the incoming high- and low-speed streams, respectively. The shear layer thickness at a given streamwise station is then defined as the distance between the point where $U^* = 0.1$ and the point where it reaches 0.9. The normalized vertical coordinate variable used in the plots is computed using the location where $U^* = 0.5$ as the origin and the vorticity thickness as the normalizing factor:

$$\delta_\omega = \frac{U_1 - U_2}{\left(\frac{\partial \overline{u}}{\partial y}\right)_{max}} \tag{3.2}$$

The streamwise turbulent intensity is defined as:

$$\sigma_u = \sqrt{\overline{u'u'}} \tag{3.3}$$

and the lateral turbulent intensity is defined as:

$$\sigma_v = \sqrt{\overline{v'v'}} \tag{3.4}$$

The *uv* component of Reynolds stress is:

$$R_{uv} = \overline{uv} - \overline{u}\,\overline{v} \qquad (3.5)$$

The streamwise velocity skewness is computed as $\overline{u'^3}/\sigma_u^3$ and the flatness as $\overline{u'^4}/\sigma_u^4$.

3.4.1 Behavior of the Various Models

In this section, the predictions of the various turbulence models are compared with each other. The results presented here are taken from the fine grid simulations (with grid dimensions of $181 \times 121 \times 66$).

As shown in Fig. 3.1, all the models predict roughly the same initial growth of the mixing layer. As one reaches the first experimental data point (60 mm downstream of the trailing edge of the splitter plate), in some cases the differences between models approach 12 percent of the experimentally determined thickness. At the last experimental data point (210 mm downstream), the maximum difference between models is almost 22 percent of the experimental value. Given the lack of data available on the incoming streams, and the consequent assumptions made in the simulations, it is perhaps not surprising that the absolute values of shear layer thickness would differ from the experiment. In addition, the geometry has been somewhat simplified (and under-resolved as well) from the experimental rig. This simplification would also have an effect on the initial portions of the mixing layer.

Of more importance is the predicted shear layer growth rate, which should be more or less independent of the details of the incoming streams once the mixing layer has achieved self-similarity. In the experiment, the flow was found to be self-similar by the time it reached 150 mm downstream of the splitting plate. The shear layer growth rate has been computed using a least-squares curve fit of the data between the 150 and 300 mm stations. The results are shown in Table 3.2. The incompressible growth rate ($\left(\frac{db}{dx}\right)_i$) is computed using the form suggested by Papamoschou and Roshko[19]:

$$\left(\frac{db}{dx}\right)_i = C_0 \frac{(1 - r_U)(1 + \sqrt{s})}{1 + r_U \sqrt{s}} \qquad (3.6)$$

Where r_U is the velocity ratio (U_2/U_1), s is the density ratio (ρ_2/ρ_1), and the value for the coefficient (C_0) was 0.083, as suggested by Goebel and Dutton[20] for thickness measured as the distance between the two points where the normalized streamwise velocity is 0.1 and 0.9, respectively. Not surprisingly, the RANS models ($k - \varepsilon$ and Spalart) perform worst of all. The algebraic LES model (Smagorinsky) improves on their results somewhat. Providing even better results are the one-equation LES models (the k-equation and dynamic k-equation models) and the DES model, all of which predict roughly the same growth rate. Finally, the best prediction is obtained using the hybrid model. All of the simulated mixing layers had a significantly lower growth rate than the experiment. The experimental value was obtained from only three points, however, which might lead to some error. It should also be noted that there is a great deal of scatter in experimental measurements by different researchers. For convective Mach numbers ranging from 0.4 to 0.6, the results (from multiple sources) presented in Elliot[21] show experimentally measured growth rates (normalized) ranging from less

than 0.5 to more than 1.0. Thus, in addition to whatever numerical problems there may be with the simulations, one would expect a relatively large experimental uncertainty as well.

Normalized streamwise velocity profiles are shown in Fig. 3.2. These data, and all other transverse profiles (unless otherwise noted), are taken from a station 210 mm downstream of the splitter plate. All of the models do a good job of capturing the experimentally observed behavior. On the low-speed side of the layer, the DES and Smagorinsky models appear to deviate somewhat more than the other models (though the errors are in opposite directions). On the high-speed side, the RANS $k - \varepsilon$ model underpredicts the velocity slightly, relative to the other models.

The inability of the RANS turbulence models to properly capture the unsteady features of this mixing layer become obvious in Fig. 3.3, which shows the predicted streamwise turbulence intensity across the mixing layer. Neither of the RANS models captures the correct intensity levels, and a qualitative comparison shows that the shapes of the curves are distorted as well, particularly by the $k - \varepsilon$ model. In contrast, the other models capture the flow features quite well. Note that away from the core of the mixing layer, the grid resolution is insufficient to maintain the freestream turbulence levels, resulting in a drop-off in the profiles at the edge of the mixing layer, relative to the experimental results. Much the same behavior is observed in the Reynolds cross-stress term (R_{uv}), although the deviation from experiment is somewhat greater for all the models (Fig. 3.4). This is to be expected, even apart from any error in the simulations, since the experimental error for cross terms is higher than that for normal terms. This error becomes even greater as one moves to higher-order turbulence statistics[22].

The streamwise velocity fluctuation skewness and flatness are shown in Figs. 3.5 and 3.6. Again, the hybrid and LES models are much more accurate than the unmodified RANS models. For these higher moments of turbulence, however, the limitations of the grid resolution become more apparent. Beyond the core region of the mixing layer, the effects of the small-scale turbulent structures become more important, and the lack of adequate grid resolution for these small flow features results in exaggerated peaks (relative to the experimental data) and, in the case of the flatness, wild fluctuations. Within the mixing layer, however, the flow is sufficiently resolved that the experimentally observed features are well captured by the LES, DES, and hybrid models.

The above results show that, for this case, the DES and hybrid $k-\varepsilon$ models do as well or better than the pure LES models. Relative to the unmodified RANS models, the DES and hybrid models represent a clear improvement.

3.4.2   Grid Sensitivity

There are two parts to the issue of grid sensitivity. The first is whether the results computed on a grid are of sufficient resolution that the solution truly represents the capabilities of the turbulence models. The second is whether there are any significant differences between the responses of these models to changing grid resolution. To answer these questions, the results from the DES and hybrid models at three different grid resolutions are presented. One complicating factor to note is that, unlike a traditional RANS solution, an LES solution will never completely "converge" as one increases

grid resolution (until it becomes a DNS solution). This is because, as more resolution is added, smaller features are resolved, resulting in additional information entering the analysis. Thus, although mention is made here of "grid convergence," the meaning of such a thing is somewhat ambiguous. The working definition employed here is that a solution is considered "grid converged" if, in the core of the mixing layer, the differences between the fine and medium grid results are on the order of (or better than) the differences between experimental results at neighboring stations (when plotted using similarity variables). In addition, one expects that the differences between the fine and medium grids should, in general, be smaller than those between the medium and coarse grids.

In Fig. 3.7 one can see that grid convergence appears to have been achieved for the shear layer thickness on both the fine and medium resolution grids. The same appears to be true of the streamwise velocity profiles (Fig. 3.8). Even the coarsest grid appears to capture these basic features of the flow quite well.

The second-order turbulence moments show more variability with grid resolution (Figs. 3.9, 3.10, and 3.11). Even here, however, the coarsest grid does a reasonable job of capturing both the qualitative trends and even the fluctuation magnitudes. The effect of resolution is somewhat different for the different models in that the largest changes typically are at different places on the profile. The DES model is slightly less sensitive to grid resolution than the hybrid model (this is particularly obvious in Fig. 3.10). The hybrid model, however, appears to be slightly more accurate on the fine grid, especially at the edges of the mixing layer.

Much the same behavior is observed in the higher moments (Figs. 3.12 and 3.13), although there appears to be no clear grid convergence advantage for the DES model. The hybrid model still arguably maintains an edge in accuracy at the fringes of the mixing layer, particularly on the low-speed side.

It thus seems safe to say that the fine grid resolution is sufficient to provide meaningful results. It would also appear that, for the most part, the DES and hybrid models provide comparable capability at the various grid resolutions.

3.4.3   Predicted Self-Similarity

One of the most interesting features of mixing layers is their self-similar nature. The question arises, therefore, do the DES and hybrid models predict self-similar behavior? If so, does one do any better than the other? To examine this issue, the results from several downstream stations (where experimental data were available for comparison) are presented.

As seen in the experiments, the streamwise velocity achieves self-similarity very early in the flow (Fig. 3.14). Both the hybrid $k - \varepsilon$ model and the DES model capture this behavior well. Although it may require magnification to see it, the DES model appears to predict self-similarity much earlier in the flow than either the hybrid model or the experiment; even the data at the 60 mm station show this trait. The hybrid model does somewhat better, although the deviation from similarity at 60 mm is less than that observed in the wind tunnel. Of course, the closer one gets to the splitter plate, the more the solution depends on how the incoming boundary layers and freestream

turbulence are handled. Therefore, any conclusions drawn from these observations are tentative at best.

In the experiments, Elliott observed that, while streamwise velocity showed self-similarity by the 120 mm station, the self-similarity of higher moments of turbulence was delayed until the 150 mm station. Much the same behavior can be observed in the computational results, as shown in Fig. 3.15 for the streamwise turbulence intensity. Both turbulence models do show the 120 mm station as being much closer to the "final" self-similar profile than was observed in the experiment. In general, however, self-similarity is achieved that is comparable to the experiment not only in peak magnitude and in the shape of the curve, but also in the variations observed between stations.

Figures 3.16 and 3.17 show, respectively, the lateral turbulence intensity and the uv component of the Reynolds stress. For these and following plots, only data from the three stations furthest downstream have been plotted. As before, the models behave slightly differently, with DES doing better in some places and the hybrid model better in others.

Figures 3.18 and 3.19 show third and fourth moments of the streamwise velocity fluctuations. Both models to a good job of capturing the observed self-similar behavior within the core of the layer. At the edges of the layer, deviations from the experimental data become significant, although the curve shapes remain consistent (except on the high-speed side of the flatness).

The above results show that both the DES and hybrid $k - \varepsilon$ models capture the important self-similarity features of the flow. Neither one, however, shows any clear advantage over the other.

3.5   Conclusions

In conclusion, it has been shown that both the DES and hybrid $k - \varepsilon$ models provide, for unsteady "LES-like" flows, a radical improvement over the conventional RANS models from which they are derived. Results using these models compare favorably with those obtained using conventional LES models. Beyond that, it is extremely difficult to draw any conclusions. Testing has shown that the results may be sensitive to a wide variety of factors, including boundary condition treatment at the inflow and outflow boundaries, treatment of incoming freestream turbulence, and grid resolution, as well as statistical sampling time and methodology. Each of these factors has been investigated, and an attempt has been made to reduce their effect, but the uncertainties they introduce are on the order of the observed differences between the DES and hybrid $k - \varepsilon$ models. In addition, while the numerical scheme used is much less dissipative than that typically used in production RANS solvers, it is not without its limitations. Finally, some experimental error exists as well. Therefore, given the relative equivalence of the results and the uncertainties involved, it is not clear how much of the deviation from experimental results observed in the simulations is due to turbulence model limitations and how much is due to errors unrelated to the turbulence models (not to mention experimental uncertainty). These questions are addressed in the following chapter.
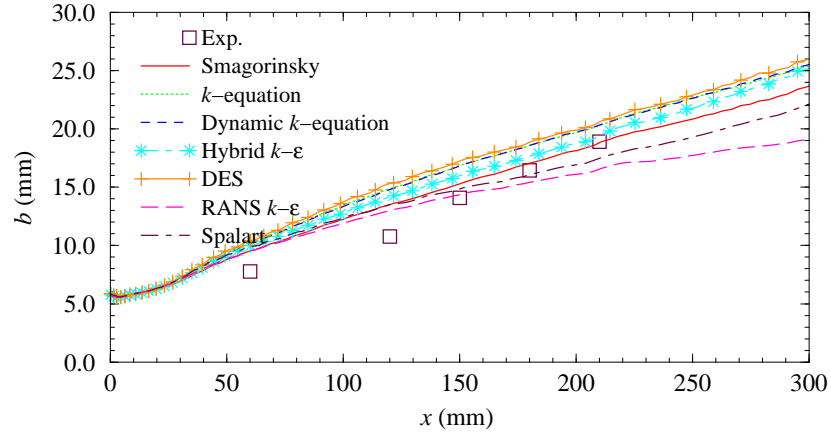
Figure 3.1: Mixing layer thickness
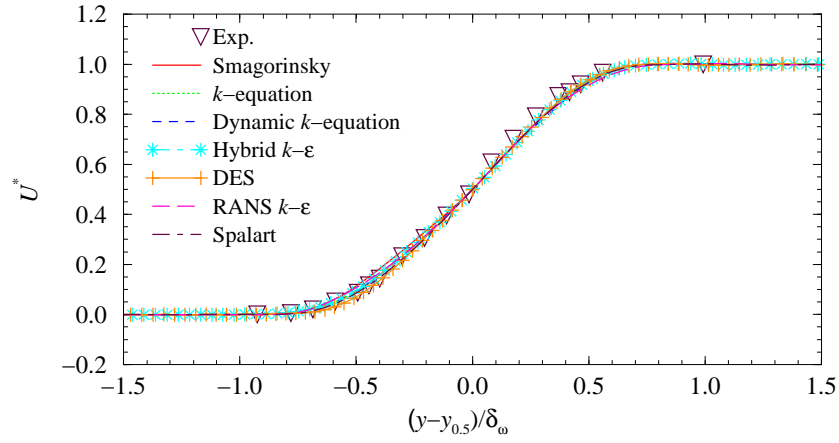
Figure 3.2: Non-dimensional streamwise velocity
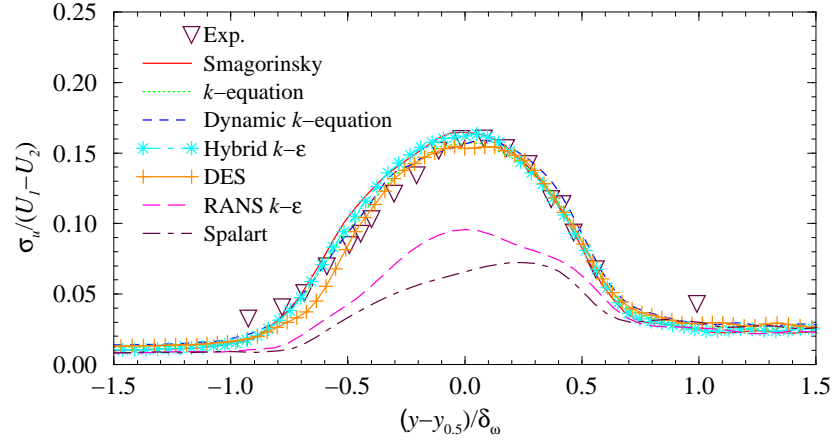
Figure 3.3: Streamwise turbulence intensity
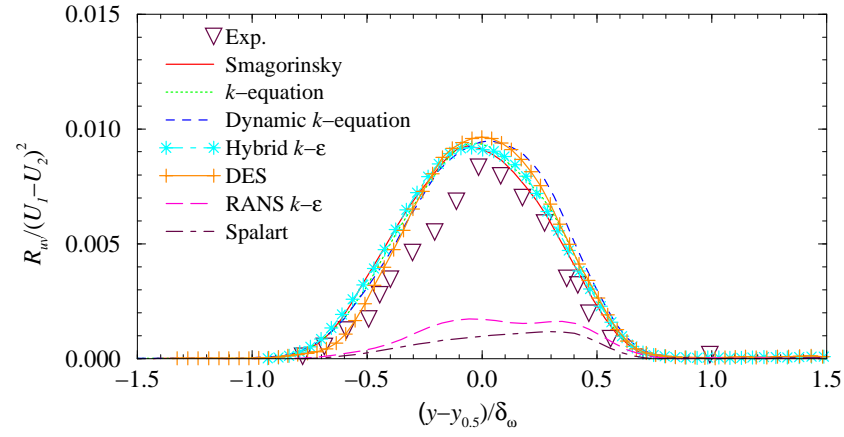
Figure 3.4: Reynolds stress profiles
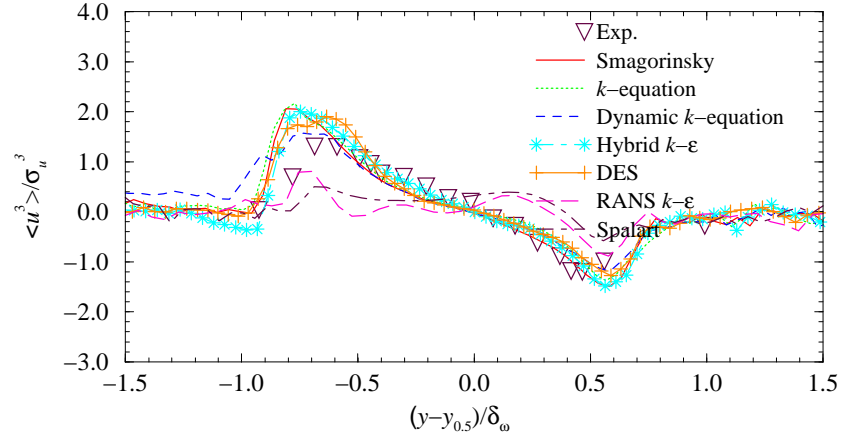
Figure 3.5: Streamwise velocity fluctuation skewness
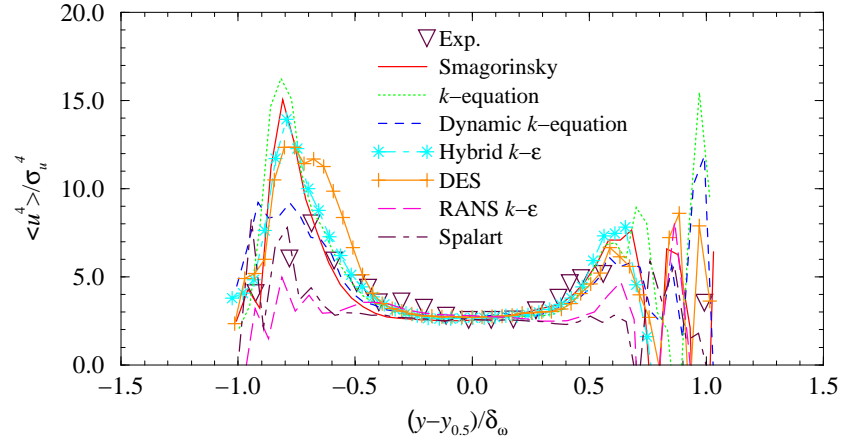
Figure 3.6: Streamwise velocity fluctuation flatness
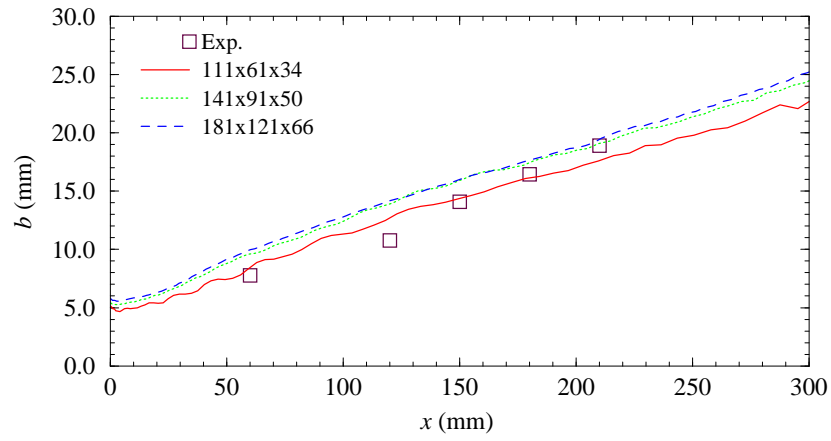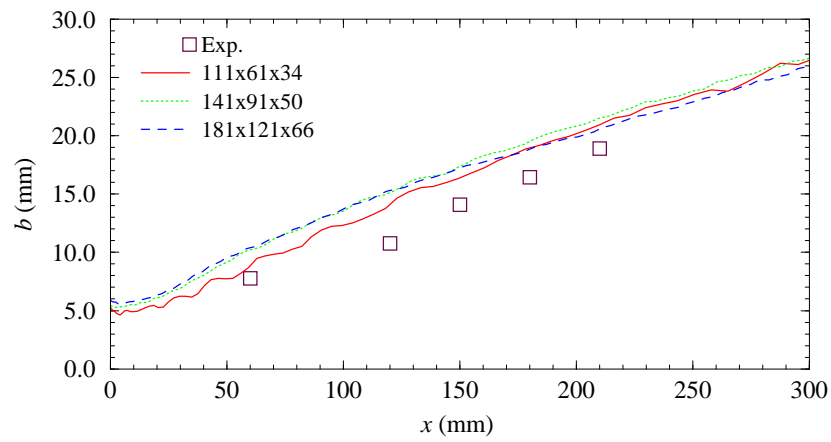
(a) Hybrid $k - \varepsilon$ model

(b) DES model

Figure 3.7: Effect of grid resolution on mixing layer thickness results
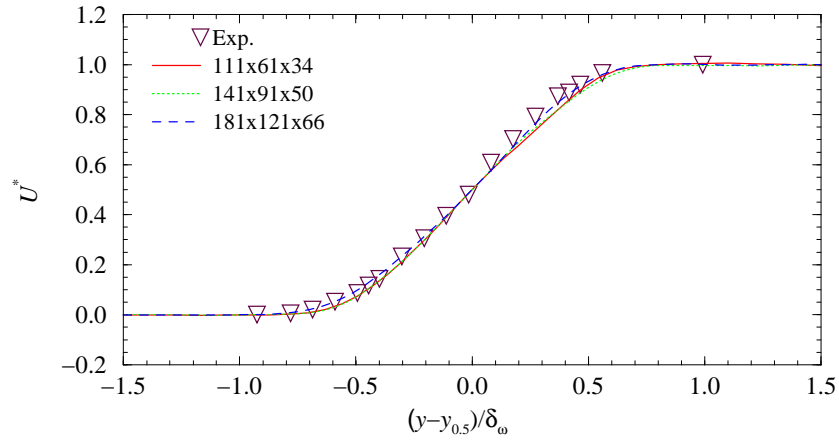
(a) Hybrid $k - \varepsilon$ model
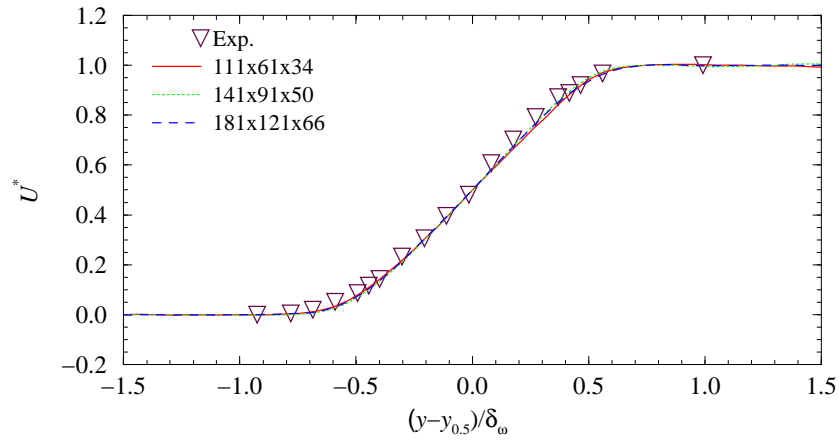
(b) DES model

Figure 3.8: Effect of grid resolution on non-dimensional streamwise velocity
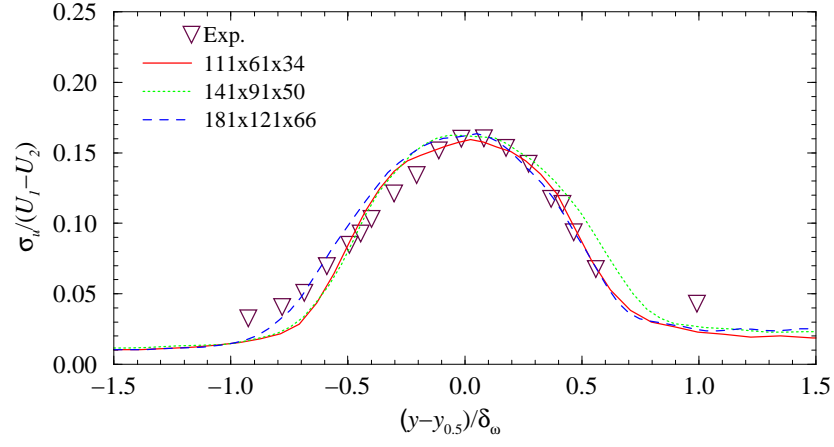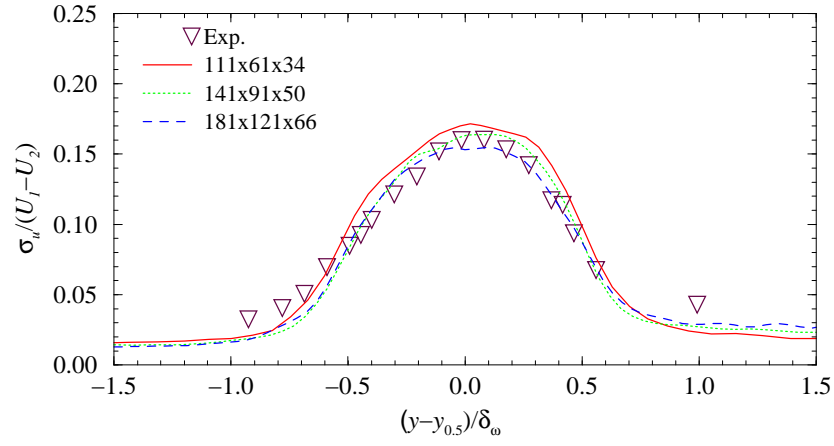
(a) Hybrid $k - \varepsilon$ model

(b) DES model

Figure 3.9: Effect of grid resolution on streamwise turbulence intensity
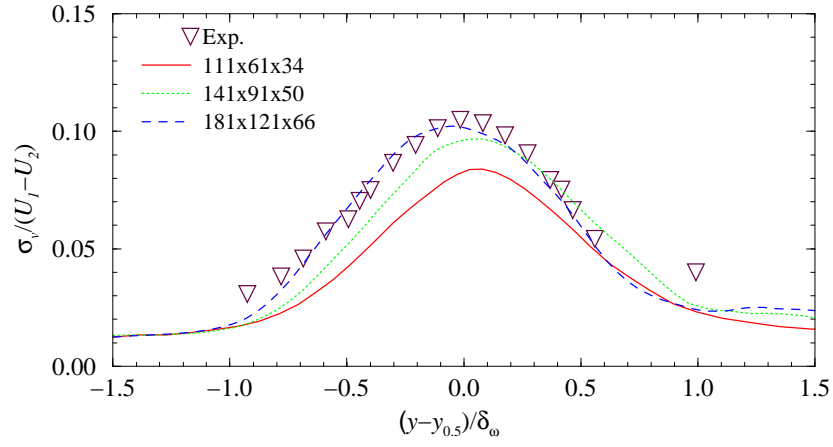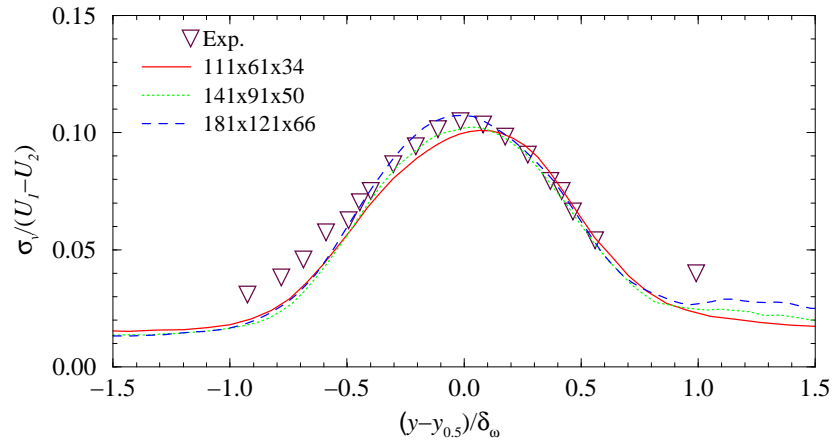
(a) Hybrid $k - \varepsilon$ model

(b) DES model

Figure 3.10: Effect of grid resolution on lateral turbulence intensity profiles
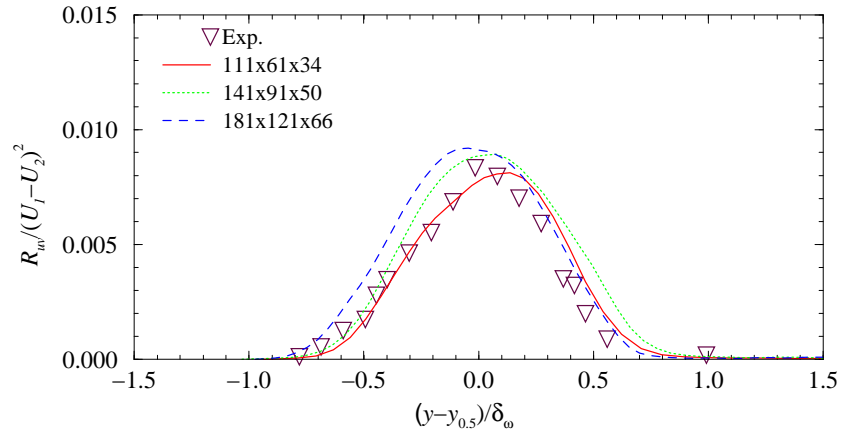
(a) Hybrid $k - \varepsilon$ model
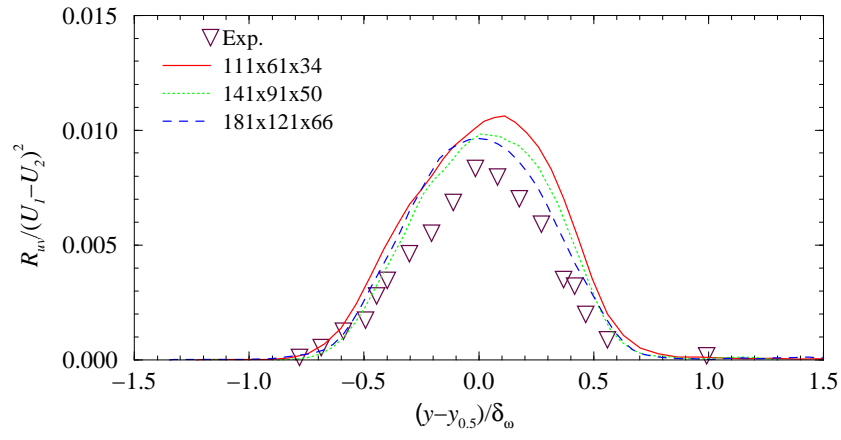
(b) DES model

Figure 3.11: Effect of grid resolution on resolved Reynolds stress
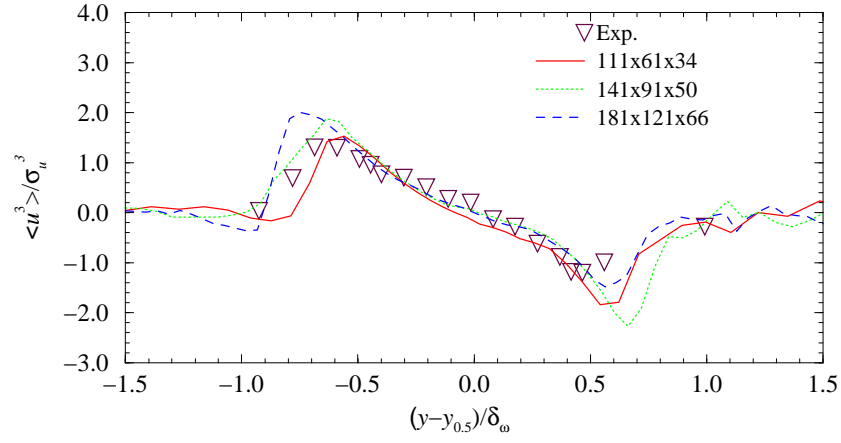
(a) Hybrid $k - \varepsilon$ model
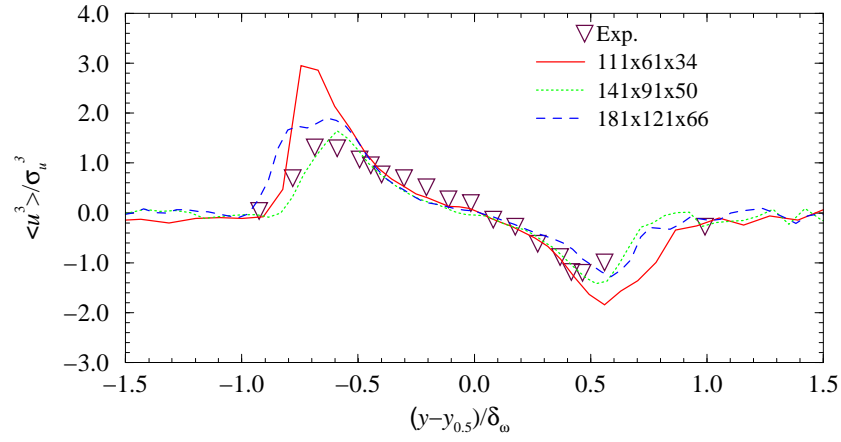
(b) DES model

Figure 3.12: Effect of grid resolution on streamwise turbulence fluctuation skewness
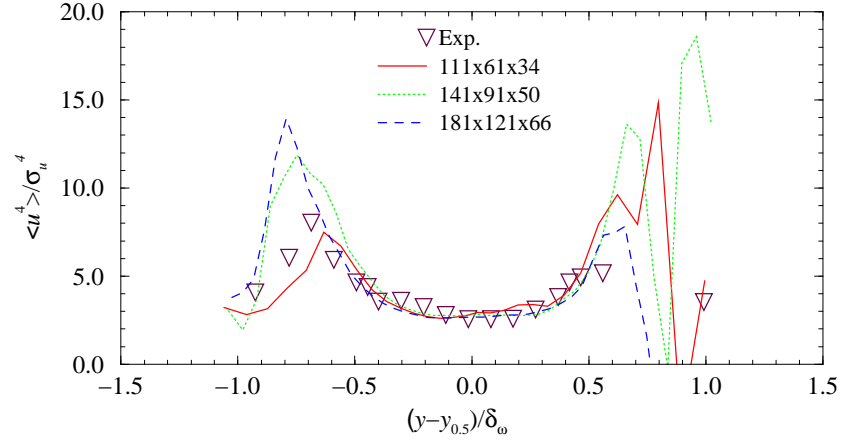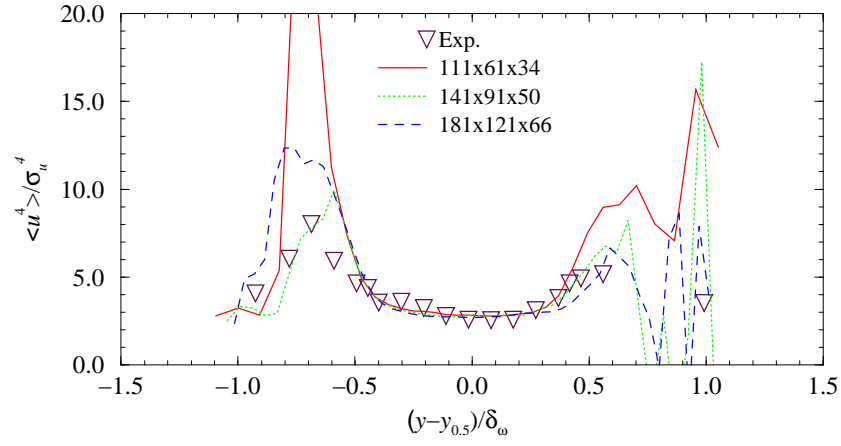
(a) Hybrid $k - \varepsilon$ model

(b) DES mode

Figure 3.13: Effect of grid resolution on streamwise turbulence fluctuation flatness
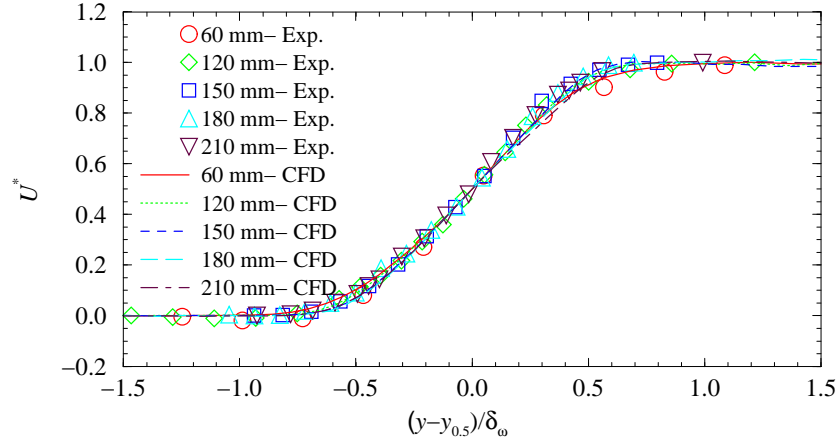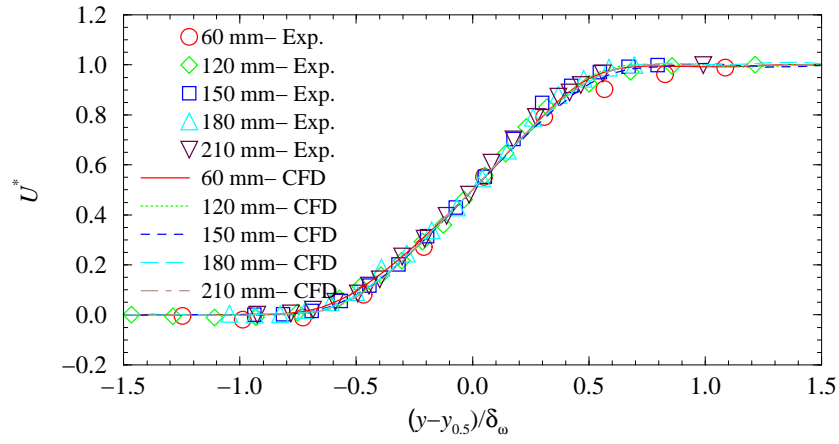
(a) Hybrid $k - \varepsilon$ model

(b) DES model

Figure 3.14: Self-similarity of streamwise velocity
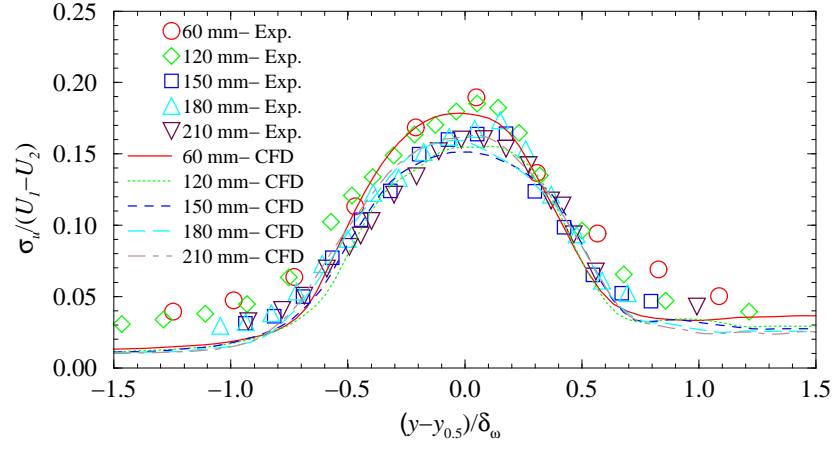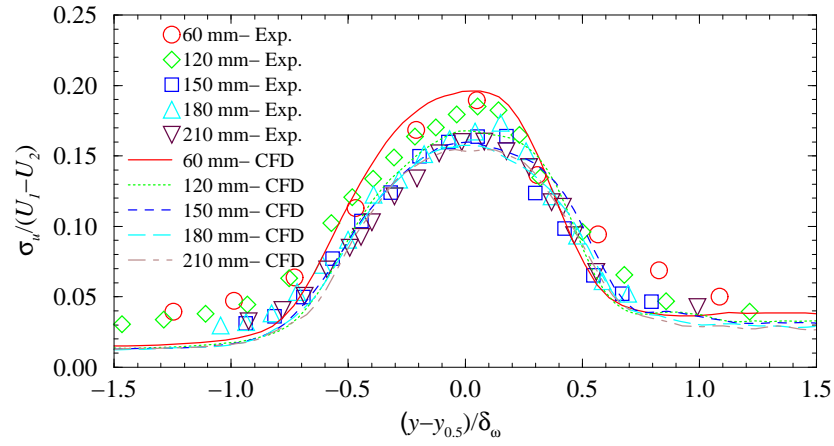
(a) Hybrid $k - \varepsilon$ model

(b) DES model

Figure 3.15: Self-similarity of streamwise turbulence intensity
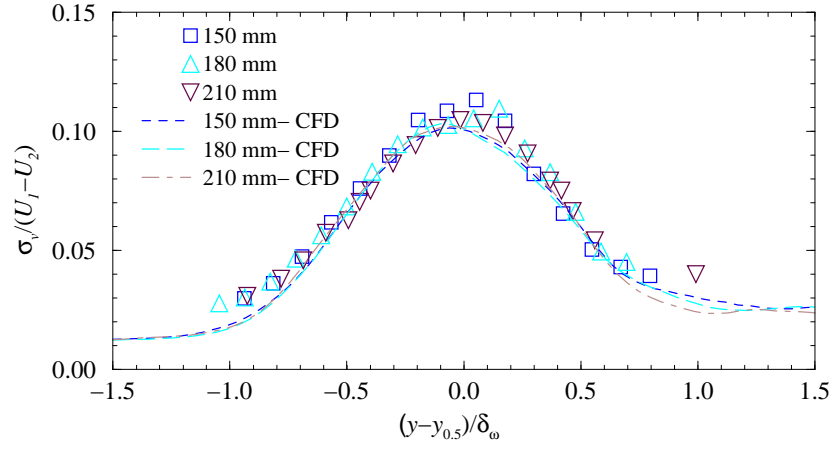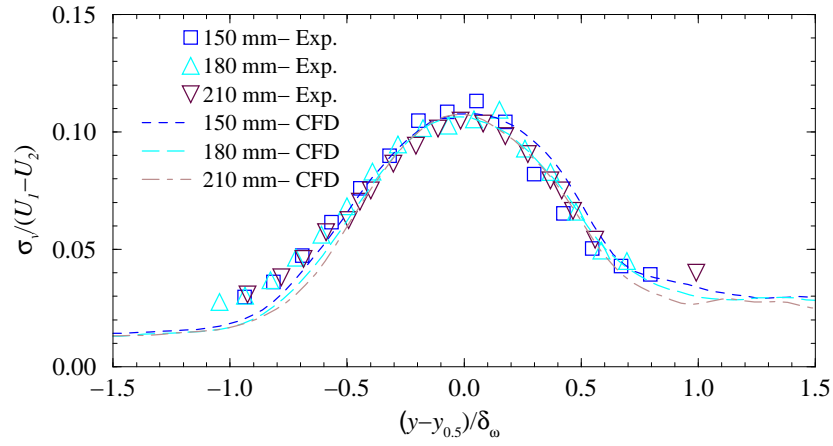
(a) Hybrid $k - \varepsilon$ model

(b) DES model

Figure 3.16: Self-similarity of lateral turbulence intensity
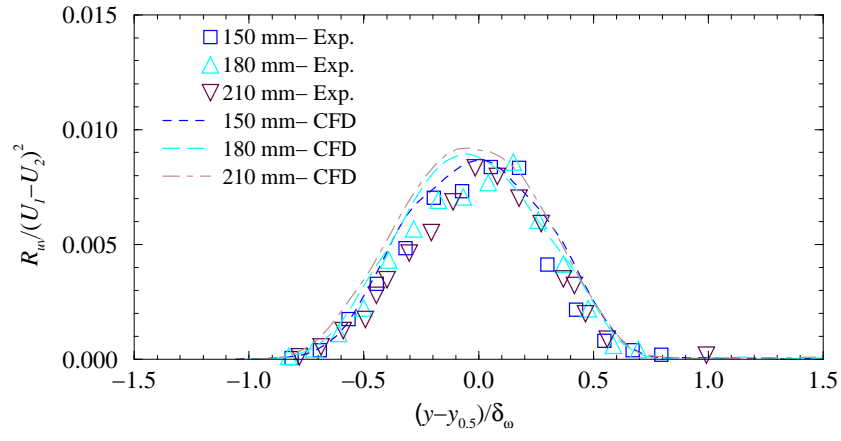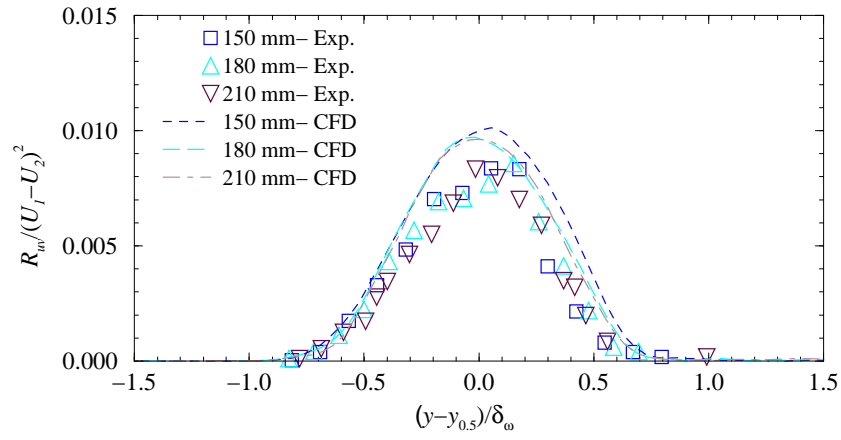
(a) Hybrid $k - \varepsilon$ model

(b) DES model

Figure 3.17: Self-similarity of Reynolds stress

26
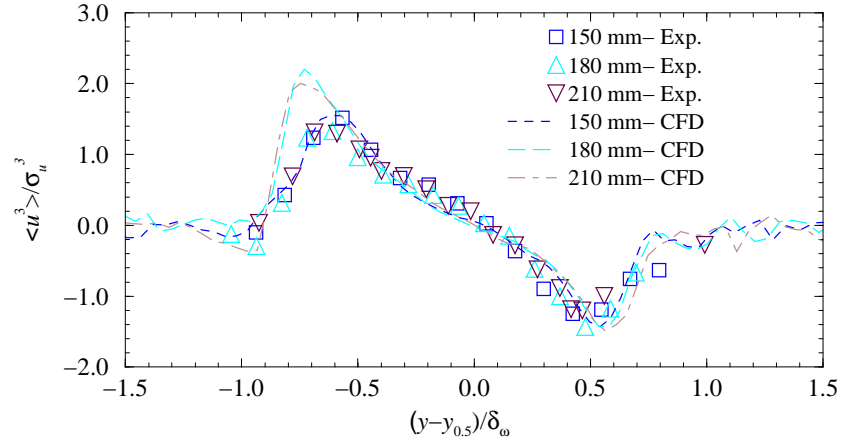
(a) Hybrid $k - \varepsilon$ model

(b) DES model

Figure 3.18: Self-similarity of streamwise velocity fluctuation skewness
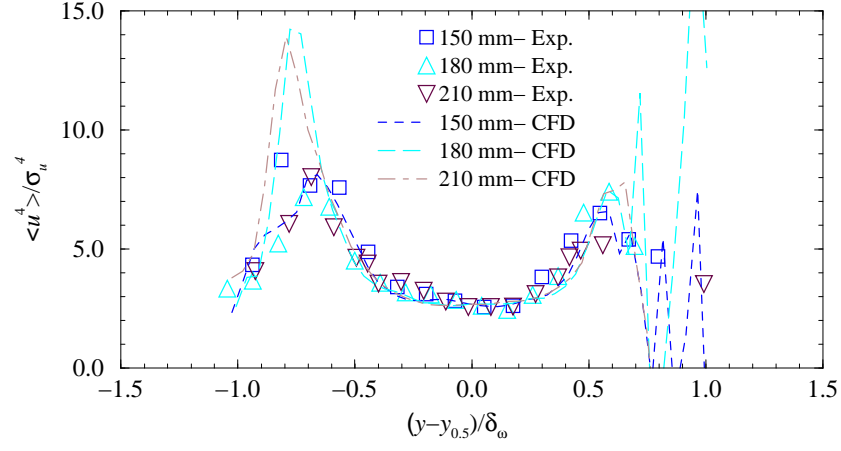
(a) Hybrid $k - \varepsilon$ model
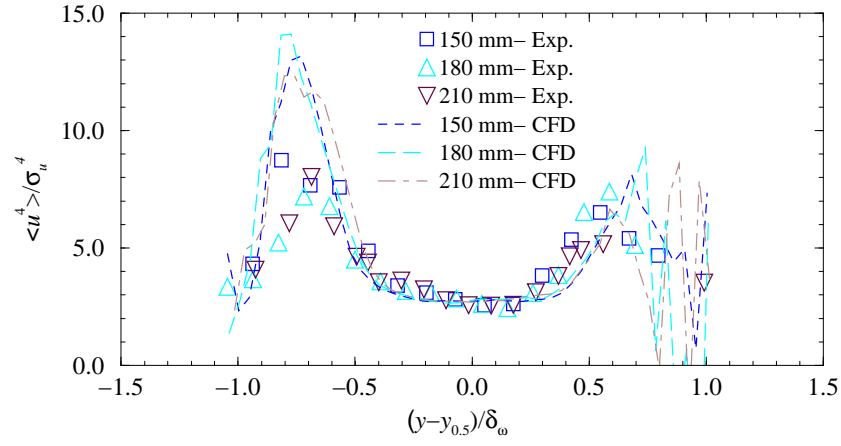
(b) DES model

Figure 3.19: Self-similarity of streamwise velocity fluctuation flatness

Chapter 4

Investigation into the Precision of Unsteady Simulations

4.1 Introduction

As the data presented in the previous chapter make manifestly clear (see also Nelson and Nichols[23]), simulations using the DES model often yield results which are very similar to those obtained using the Nichols and Nelson hybrid approach. Since other sources of error are known to exist in these simulations, the question arises as to whether or not the observed differences due to model choice are actually significant relative to the other error sources. If not, then it becomes vital that work on unsteady flow simulations (of this nature) focus more on the dominant error sources and less on turbulence model issues.

To answer this question, a series of simulations was performed, using the same LES code employed for the previous chapter's work, which examined a variety of issues to determine their relative effect on the results. The test case was again the planar mixing layer (convective Mach number of 0.51) studied experimentally by Samimy and Elliott[17, 24, 25].

The potential sources of error in a CFD simulation of any type are nearly limitless. Therefore, of necessity, the following analysis only examines a subset of issues that could be influencing the results. The areas investigated can be broken into two broad themes: boundary condition issues and statistical issues.

Since any solution to the Navier-Stokes equations is determined by the boundary conditions imposed in space and time (in conjunction with the physical geometry of the case), the treatment of boundaries is an obvious area to investigate for impact on the overall solution. This is particularly true for unsteady cases, where the reflection of transient waves from boundaries can be a serious problem. Thus, the placement of both the inflow and outflow boundaries was varied in an attempt to determine the extent to which this influences the solution. Also, the original inflow boundary condition employed for these simulations was based on an inviscid (characteristic) analysis. To help assess the effect of such an assumption, the boundary condition was modified so

as to add the viscous stresses as well.

Another possible source of error for unsteady simulations is the procedure by which the unsteady solution is processed to obtain time-averaged results. If the period over which the solution is averaged is not sufficient, then the results will not be accurate, particularly for the higher statistical moments. Furthermore, if the solution has not been given sufficient time to wash out the effects of the initial conditions, then these residual effects can also contaminate the solution. The current analysis attempts to address both of these issues.

Among the issues not addressed in this work were the effects of the simplified geometry used for these simulations and the specifics of the incoming pseudo-turbulence (spectrum, amplitude, etc.). While these issues might be important at times, these areas were ignored in order to focus on the aforementioned areas. This was partly due to the project's limited resources, but also because of the lack of experimental data with which to compare the simulated inflows, especially on the low speed side.

4.2   Test Case Description

The effect of grid resolution on the issues under consideration was tested by running the tests using three different base grids. The resolutions for these base grids were $91 \times 61 \times 34$, $121 \times 91 \times 50$, and $161 \times 121 \times 66$. By default, the same boundary conditions were used and the same statistical data collection procedure was followed (run for 30,000 steps and then collect data for a further 60,000). Except where noted, a variation of the Nichols and Nelson hybrid model was used for all tests.

The boundary location tests varied the above grids as follows (see Table 4.1). The first modification was to extend the inflow by ten uniform points in the upstream direction. Second, for the extended outflow case, a region of ten highly stretched points was added to the outflow boundary. Then a third grid was constructed with both of the aforementioned extensions.

A fourth grid was constructed similar to the extended inflow case, but with a further twenty points added to the inflow, for a total of thirty more streamwise points than the base grid. The fifth grid was similar to the extended outflow grid, but with an additional ten highly stretched points at the outflow. The sixth and final geometric variation had both the additional inflow and outflow points. The effects of adding viscous terms to the inflow boundary were then tested using the "Ext. in/out–2" grid.

To test the precision of the statistical data collection procedure, three additional cases were run (again using the "Ext. in/out–2" grid). Two of these cases extended the length of time over which data was collected. The first of these took data for 90,000 iterations, rather than the base 60,000; the second case doubled the base period for collecting data to 120,000 time steps. The final variation delayed taking statistical data until the solution had run for 90,000 steps; at that point data was collected for the standard 60,000 steps.

Table 4.1: Unsteady Simulation Precision Test Cases

Label	Description
Base	$91 \times 61 \times 34$, $141 \times 91 \times 50$, or $161 \times 121 \times 66$.
Extend in	10 uniform points added upstream
Extend out	10 stretched points added downstream
Extend in/out	Extend both inflow and outflow 10 points
Ext. in–2	30 uniform points added upstream
Ext. out–2	20 stretched points added downstream
Ext. in/out–2	Add 30 pts upstream and 20 pts downstream
Visc. inflow	Add viscous stresses at inflow
Ext. stats	Extend time averaging by 50%
Ext. stats–2	Take data for twice as long as base
Ext. init.	Delay start of averaging

4.3 Results

As was seen before[23], the non-dimensional streamwise velocity profile was completely insensitive to all variations. An example of this is plotted in Figure 4.1, which shows the profile at the 210mm station at the coarsest grid resolution (base grid $91 \times 61 \times 34$). In addition to the aforementioned test cases, the previously presented results from the DES model are plotted for comparison. In this work, the choice of model is considered to be "significant" only if the DES model results lie outside the scatter from the other cases. In this case, obviously, the results are insensitive to the choice of model.

A more interesting behavior is found in the streamwise turbulent intensity. As shown in Figure 4.2, the relative importance of the turbulence model varies with grid resolution. At the coarsest resolution, the DES model prediction is noticeably different on the high speed side of the mixing layer. At the medium resolution, however, this difference is reduced to the point of insignificance. For the fine grid cases, the DES model again appears to result in significant (albeit small) differences. It is encouraging that, for all three baseline grid resolutions, the boundary location does not dramatically change the character of the results. Therefore, while it may be difficult to determine which of the hybrid approaches is best, the dramatic improvement observed relative to the base RANS models (see Figure 3.3) appears to be real.

A stronger dependence on boundary location is shown by the higher moments of turbulence. This is illustrated in Figure 4.3 using the streamwise velocity skewness. In this case, choice of hybrid model seems to be less important, with the scatter from the boundary location variations bracketing the DES curves virtually everywhere. As expected, the largest deviations occur at the edges of the mixing layer, while the core shows good agreement (improving with resolution) for all grids. Of course, given the limited grid resolution beyond the core of the mixing layer, it is doubtful that any strong conclusions can be formed based on that deviation. Again, the differences observed are

not such that the overall benefit of hybrid models relative to the baseline RANS models would be called into question.

The effects of the variation of the statistical sampling procedure or inclusion of viscous terms at the inflow boundary are shown in Figure 4.4 for the streamwise turbulent intensity. Within the core of the mixing layer, only delaying the initiation of data collection has an appreciable effect (with a reduction in peak intensity at the medium resolution). This result was unexpected, especially since extending the statistical gathering period (so that the two runs were of the same length) had no such effect. Neither the fine grid nor the coarse grid showed the same behavior. A similar situation was observed in the *uv* component of Reynolds stress (Figure 4.5). In general, extending the period before gathering statistics had a larger than expected effect on the low speed side of the mixing layer, while the core and high speed sides were relatively unaffected. This is well illustrated by the streamwise velocity skewness, as shown in Figure 4.6.

In the above plots, the addition of viscous terms at the inflow was observed to have little effect. When changes were observed, they were confined, for the most part, to the edges of the mixing layer. In this region, the other uncertainties in the simulation make it difficult to draw any definite conclusions as to advantages or disadvantages of this strategy.

4.4   Conclusions

Based on the above analysis, it appears that the question of whether or not the choice of hybrid model technique is significant depends to some degree on what data is sought and the relative resolution of the grid. While the precision of these simulations is clearly sufficient to demonstrate the general superiority of the hybrid technique over a standard RANS model for this class of problem (as in Nelson and Nichols[23]), the uncertainties in these results would appear to call into question most conclusions regarding the relative merit of the different hybrid techniques. For most quantities, the differences are either not significant at all, or if they are, it is not yet clear which is the better model.

Furthermore, while a mixing layer is expected to behave in relatively "universal" fashion once self-similarity is achieved (and the data is plotted using the appropriate similarity variables), the initial development is heavily influenced by the inflow conditions (e.g. boundary layer thickness, inflow turbulence intensity, turbulence spectrum, etc.). It is, therefore, entirely possible (even probable), that even if all of the other issues raised here were dealt with, the inflow conditions could be tweaked to give an advantage to either of the hybrid models. In the absence of more complete experimental data about the inflow conditions, however, such an exercise would prove nothing.

As with boundary location, this investigation found that the original statistical data collection methodology was adequate to clearly show the advantages of the hybrid models to predict the core of the mixing layer relative to the RANS models upon which they are based. Extending the sampling time or delaying the initiation of data sampling was, however, seen to have an unexpectedly large effect. Given that the preponderance of changes were seen on the low-speed side of the mixing layer, it would appear that the original sampling technique did not allow for the core flow on that side to develop
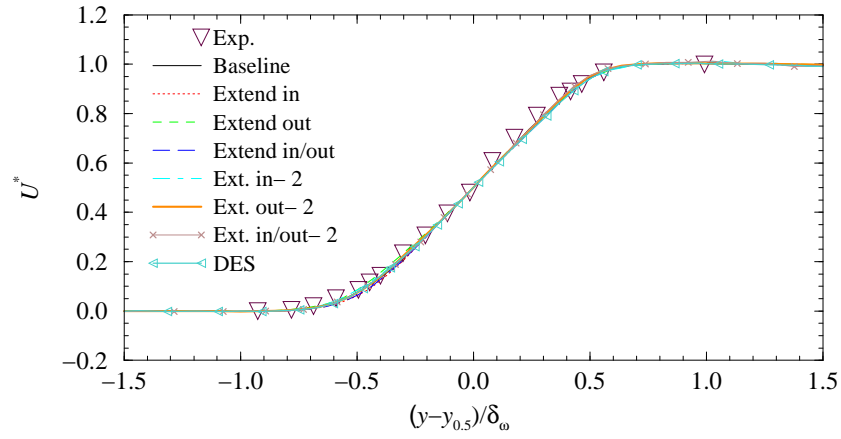
Figure 4.1: Variation of non-dimensional streamwise velocity with boundary location (coarse grid)

sufficiently to ensure a statistically stationary solution everywhere in the flowfield.

Adding in viscous terms at the inflow boundary was seen to have only a minor effect in most areas of the flow. When differences were observed, it was not readily apparent that the results were thereby improved. It is expected that such a question can only be resolved using simpler test cases which have a more precisely known solution.
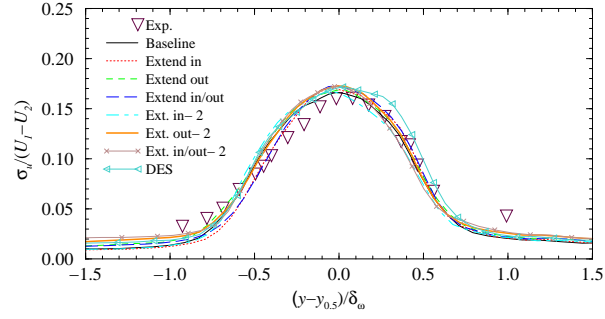
(a) Coarse base grid
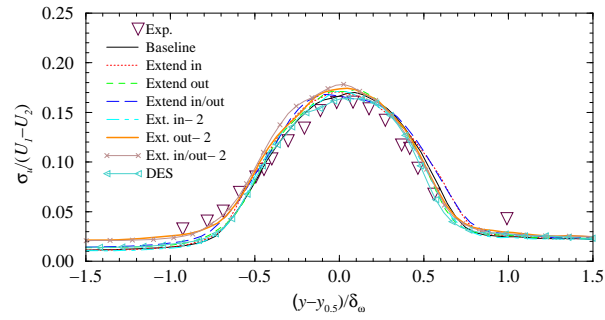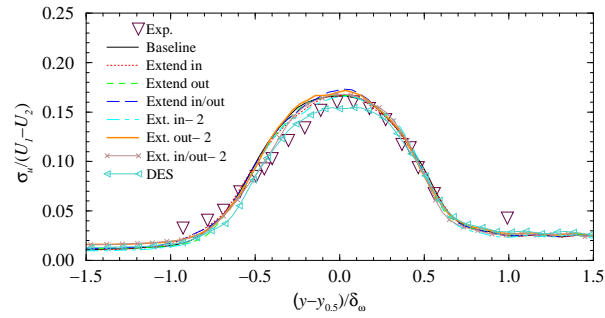
(b) Medium base grid

(c) Fine base grid

Figure 4.2: Effect of boundary location on non-dimensional streamwise turbulent intensity
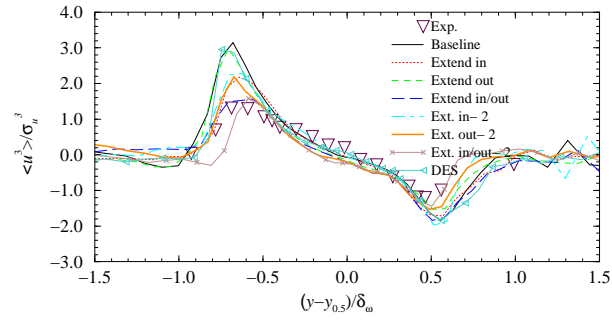
(a) Coarse base grid
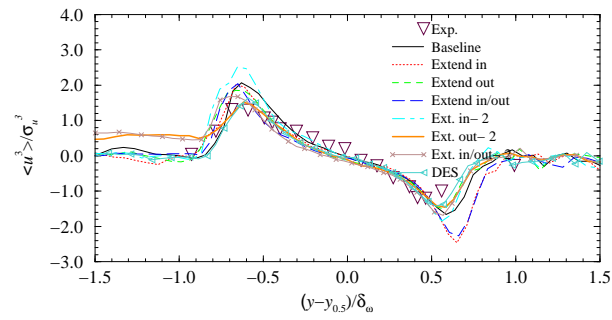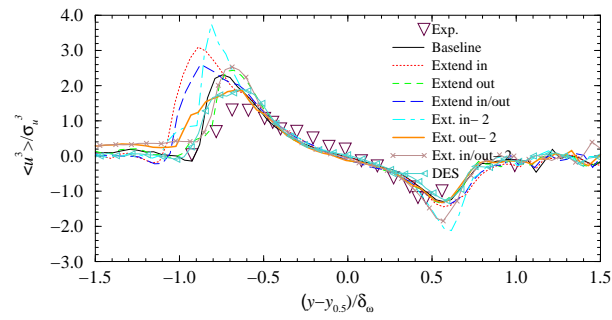
(b) Medium base grid

(c) Fine base grid

Figure 4.3: Effect of boundary location on non-dimensional streamwise velocity skewness
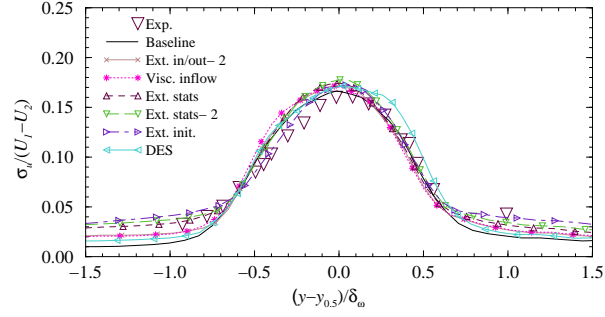
(a) Coarse base grid
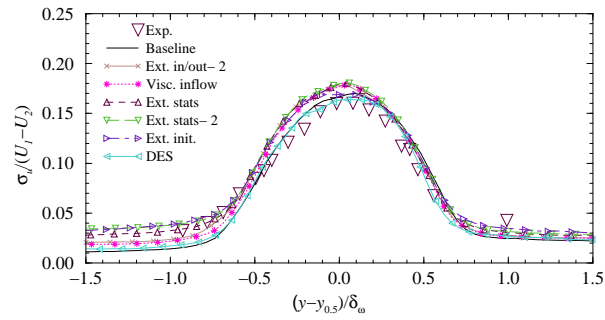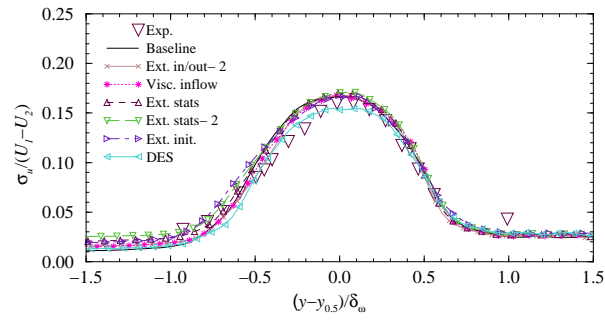
(b) Medium base grid

(c) Fine base grid

Figure 4.4: Variation of streamwise turbulent intensity with data collection method
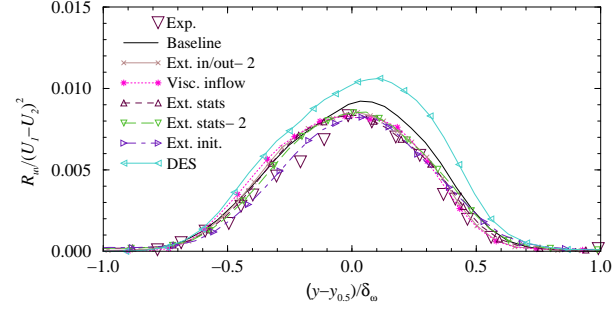
(a) Coarse base grid
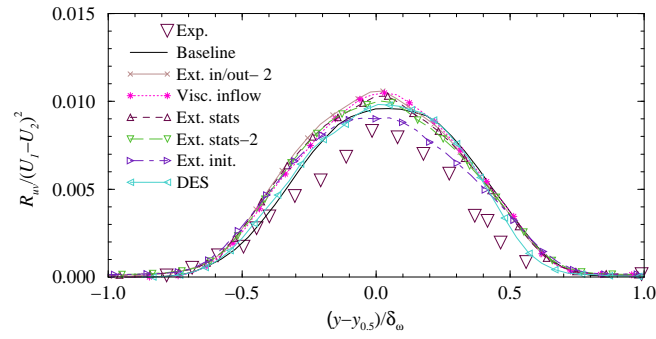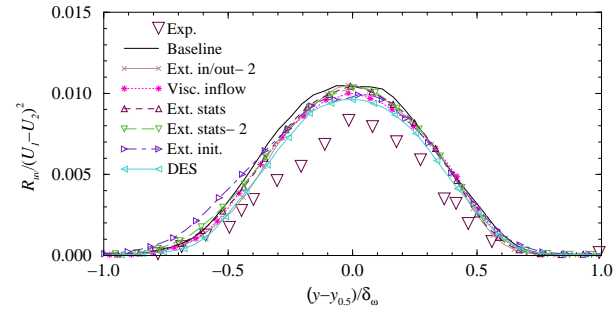
(b) Medium base grid

(c) Fine base grid

Figure 4.5: Variation of *uv* component of Reynolds stress with data collection method

37
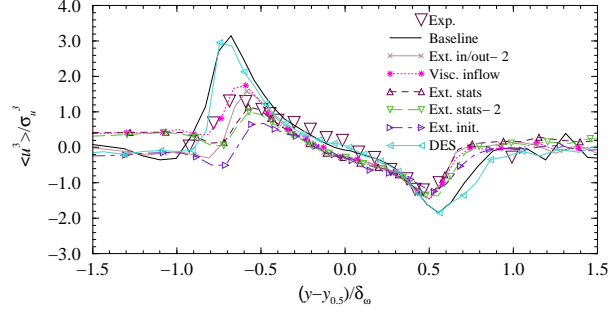
(a) Coarse base grid
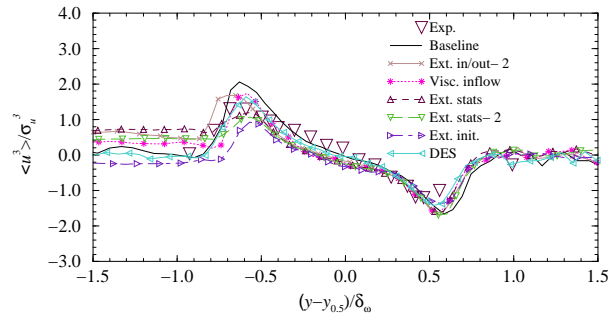
(b) Medium base grid
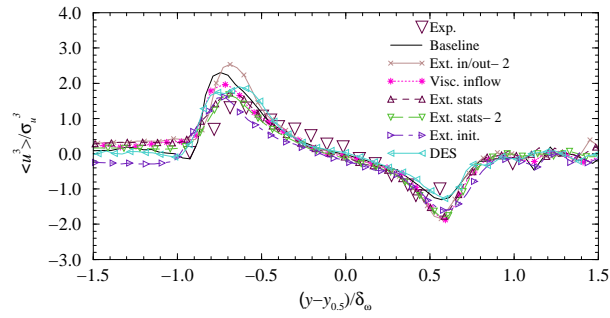
(c) Fine base grid

Figure 4.6: Variation of streamwise velocity skewness with data collection method

Chapter 5

Applications of Hybrid RANS/LES Turbulence Models

The standard Spalart-Allmaras one-equation turbulence model and Menter's SST two-equation turbulence model along with the Detached Eddy Simulation (DES) version of the Spalart-Allmaras model and the hybrid version of the SST model were applied to Several test cases. The first two cases are two-dimensional flows. In reality there are no truly two-dimensional unsteady turbulent flows, but these two-dimensional cases allow the turbulence models to be investigated quickly and allow some means of characterizing their performance. Three-dimensional effects would tend to reduce the magnitude of the unsteady forces and delay the onset of the unsteadiness in these cases since the third dimension would provide an avenue to relieve the maximum and minimum pressure peaks. The remaining test cases were true three-dimensional applications. All these test cases were run using the NXAIR Navier-Stokes code[26]. Wall function boundary conditions were used for these applications since they have been shown to provide reasonable results for similar unsteady applications[26].

5.1   Two-Dimensional Cylinder

Unsteady two-dimensional calculations were performed for the vortex shedding from a circular cylinder for $M = 0.2$ and $Re_d = 8 \times 10^6$. The computational grid was 201×201 with an initial wall spacing of 2×10^{-4} diameters, which corresponds to a $y+$ of about 20. The time step used in the calculations was a constant 9.1×10^{-5} sec., which corresponds to about 150 steps per cycle of the shedding frequency.

   The instantaneous pressure contours for the four turbulence models are shown in Fig. 5.1. The vortex shedding is clearly evident behind the cylinder. The hybrid RANS/LES models produce a much lower pressure in the core of the shed vortices than do the standard models. The pressure distribution across the nearest shed vortex for each turbulence model is shown in Fig. 5.2 (note that the vortex location is not exactly the same for each of the models at this observation time). The legend notation is as follows: "SST" refers to the standard Menter SST model, "SST MS" refers to the

hybrid SST model, "SA" refers to the Spalart-Allmaras model, and "SA DES" refers to the DES version of the Spalart-Allmaras model. The hybrid RANS/LES models are seen to predict about the same minimum pressure in the vortex. This would indicate an improvement in the results with the hybrid RANS/LES models since the standard RANS models are known to over-predict the minimum pressure in a vortex[8]. The instantaneous eddy viscosity contours are shown in Fig. 5.3. The eddy viscosity distributions differ radically for each turbulence model. The SST model predicts the highest eddy viscosity and also has the highest pressure in the vortex core. The Spalart model has high eddy viscosity near the cylinder and rapidly decreases away from the body. The hybrid SST model has low eddy viscosity near the cylinder, but the eddy viscosity rapidly increases away from the cylinder as the computational grid becomes coarser. The DES model has relatively low eddy viscosity everywhere in the field. The differences in the DES model and the hybrid SST model may be due to the fact that the latter examines locally predicted turbulent length scales when determining whether to operate in RANS or LES mode, while the former switches based purely on distance from the nearest wall and the local grid scale.

The spectral results for axial and normal force are shown in Fig. 5.4 and Fig. 5.5 respectively. These results were taken from the last 4096 time steps of the solution. While the energy in the primary peak is similar for all the models, the hybrid RANS/LES models are seen to produce much more energy in the secondary peaks and the overall background. The non-harmonic higher energy peaks at the higher frequencies predicted by the hybrid RANS/LES models indicate the presence of small-scale structures in the flow field. These structures can clearly be seen in Fig. 5.1. The average cylinder drag and the Strouhal number of the primary peak in the normal force spectrum for both the CFD and experimental data[27, 28, 29] are shown in Table 5.1. The predicted Strouhal number is seen to be in good agreement with the experimental data for all the turbulence models. The hybrid RANS/LES models predict a higher drag coefficient than do the standard turbulence models, but all the models produce a reasonable result compared to the scatter in the experimental values.

The data from Jones [27] was taken in a 16 foot tunnel with a 3 foot cylinder. This represents a tunnel blockage of nearly 20 percent. Therefore, the effect of the walls is potentially quite large. To test this, the case was re-run with walls present using the standard SST model. With the walls in place the results from this run indicate a significant effect on the predicted drag. Indeed, the drag now matches the experimental data ($c_d = 0.53$).

5.2   Two-dimensional Oscillating NACA 0015 Airfoil

The second test case was an oscillating two-dimensional NACA 0015 airfoil. The experimental configuration [30] included a wing section that spanned the wind tunnel wall and an end plate. Pressure data was taken at four spanwise locations and did indicate that three-dimensional effects were not insignificant at the post-stall angles-of-attack. This could also be seen in tuft photographs. Sectional coefficients were taken by integrating the pressure measurements. The comparisons here are with the mid-span location that had twenty pressure ports. The pressure transducer output was low-pass

Table 5.1: Comparison of CFD and Data for the Unsteady Flow from a Circular Cylinder for $M = 0.2$ and $Re_d = 8.0 \times 10^6$

Data Source	c_d	St
CFD–SST Model	0.62	0.29
CFD–Hybrid SST Model	0.85	0.30
CFD–Spalart-Allmaras Model	0.68	0.29
CFD–DES Model	0.83	0.30
Data–Jones et. al [27]	0.53	0.30
Data–Roshko [28]	0.79	0.27
Data–Schlichting [29]	-	0.29

filtered at 500 Hz. The net effect of the experimental setup was that the unsteady data is highly filtered.

The flow conditions for the experiment was $M = 0.29$ and $Re_c = 1.95 \times 10^6$, where c is the airfoil chord. The airfoil was oscillated about the quarter chord location at three mean angles-of-attack, 4°, 11°, and 15°. The amplitude of the oscillation was $\pm 4.2°$ for all cases. The instantaneous angle-of-attack was given by

$$\alpha(t) = \alpha_0 + \alpha_1 \sin(Kt) \tag{5.1}$$

where K is the reduced frequency given by

$$K = \frac{\overline{\omega} c}{2 U_\infty} = 2St \tag{5.2}$$

Here ω was the frequency of oscillation (10.1 Hz) which yields $K = 0.1$.

The calculations were performed on a 341×51 "C" mesh with 241 points around the airfoil. The initial wall spacing was 0.00025 chords that corresponds to a $y+$ of about 30. Wall function boundary conditions were used in these calculations. The time step for the calculation was 2.2×10^{-5} seconds which corresponds to about 3200 time steps per wing oscillation cycle. The pressures around the wing were integrated at each time step for comparison with the experimental data.

Figure 5.6 shows the pressure contours for the airfoil oscillating about the 4° mean angle-of-attack. The airfoil is at $\alpha = 7.92°$ on the down stroke. There appears to be very little difference between the models for this attached flow case. Comparisons of the predicted and experimental forces and moment are shown in Fig. 5.7. The standard Spalart-Allmaras model seems to give the best agreement with the experimental data, but all the models yield reasonable results as well.

The pressure contours for the airfoil oscillating about the 11° mean angle-of-attack is shown in Fig. 5.8. The airfoil is at $\alpha = 14.93°$ on the up stroke. The presence of small-scale structure in the near wake of the airfoil can be seen in the hybrid RANS/LES results. Eddy viscosity contours for the four turbulence models are shown in Fig. 5.9. The two RANS models predict similar distributions on the airfoil, but the

41

SST model predicts higher levels of eddy viscosity in the wake than does the Spalart-Allmaras model. Both of the hybrid RANS/LES models are seen to reduce the eddy viscosity in the aft region of the airfoil and in the near wake. The hybrid SST model recovers a higher level of eddy viscosity in the wake than does the DES model. Comparisons of the predicted and experimental forces and moment are shown in Fig. 5.10. The hybrid RANS/LES models and the SST model show distinct oscillations on the down stroke at the high angles-of-attack. The Spalart-Allmaras model does not predict this effect. The data show some small oscillations in this angle-of-attack range. It is suspected that with the limited number of pressure ports, the low frequency filtering, and the three-dimensional effects the experimental results have filtered and damped out most of the oscillations. The spectral result for the normal force is shown in Fig. 5.11. These results were taken from the last 4096 time steps of the solutions. The hybrid RANS/LES models and the SST model all show significant energy above 500 Hz, which would not be seen in the experimental results because of the filters employed in the data reduction.

The pressure contours for the airfoil oscillating about the 15° mean angle-of-attack is shown in Fig. 5.12. The airfoil is at $\alpha = 18.92°$ on the down stroke. The hybrid RANS/LES models and the SST model all show a large vortical structure above the airfoil with smaller structures coming off the airfoil leading and trailing edges. The minimum pressure for the large vortex is lower for the hybrid RANS/LES models than in the SST model. The Spalart-Allmaras model does not show any structure above the airfoil. Eddy viscosity contours for the four models are shown in Fig. 5.13. Again there is considerable difference in the results. The SST model has high values of eddy viscosity in the region above the upper surface of the airfoil. The hybrid SST model has much lower values near the airfoil surface, but approximates the SST model in the region away from the airfoil. The DES model has low eddy viscosity values everywhere, which again may be due to the strategy used to switch between RANS and LES modes. The Spalart-Allmaras model has high eddy viscosity values near the airfoil surface. Comparisons of the predicted and experimental forces and moment are shown in Fig. 5.14. All of the models show oscillations on the down stroke and on the end of the upstroke. The data does not show this effect. Again, it is suspected that the experimental results have filtered out most of the oscillations in the data reduction process. The spectral result for the normal force is shown in Fig. 5.15. These results were taken from the last 4096 time steps of the solutions. The hybrid RANS/LES models show significant energy above 200 Hz, which would not be seen in the experimental results because of the data reduction procedure. The RANS models both have a spectral peak at about 200 Hz.

5.3 WICS Bay

Unsteady Navier-Stokes calculations were also performed for the WICS (Weapons Internal Carriage and Separation) $L/D = 4.5$ weapons bay [31] for $M = 0.95$ and $Re = 2.5 \times 10^6/ft$. The wind tunnel data were obtained in the AEDC four-foot transonic wind tunnel. The weapons bay was 18 in. long, 4 in. wide, and 4 in. deep. The computational geometry was a flat plate that extended 15 in. upstream of the bay to

match the experiment and 25 in. downstream of the bay. The sides of the computational grid extended 50 in. on either side of the bay centerline. As in the previous simulations, wall functions for all viscous walls. The wall spacing was chosen as 0.0075 in., which corresponds to a $y+$ of 50 on the upstream plate. The grid system had 1,132,860 points broken into eight grids. A constant time step of 7.88×10^{-6} seconds was used in the calculation. The calculation was run 2000 steps to remove the initial transients and all unsteady results were processed over the last 8192 time steps.

Mach number contours on the WICS bay centerline are shown in Fig. 5.16 for all the turbulence models. All of the models except the DES models produce qualitatively similar results. The DES model seems to be much more dynamic at this moment of observation. The eddy viscosity contours are shown in Fig. 5.17. The Spalart-Allmaras model predicts high values of eddy viscosity in side the bay. The SST model has regions of high eddy viscosity within the bay, but has less eddy viscosity overall than does the Spalart-Allmaras model. The hybrid SST model has much lower values of eddy viscosity in the bay than do the RANS models, and the DES model seems to have almost no eddy viscosity in the bay, indicating that the simulation is virtually a MILES approach in this region. Mach number contours at $X/L = 0.61$ are shown in Fig. 5.18. These contours indicate the three-dimensionality of the flow. The DES model seems to demonstrate the largest three-dimensional effects.

The time-averaged pressure coefficient and the sound pressure level along the bay centerline are shown in Fig. 5.19. All four of the models are in reasonable agreement with data. The three outlying sound pressure level data points are suspected to be bad data, but are included here for completeness. Spectral results for two locations in the bay are shown in Fig. 5.20. All of the models predict the largest spectral peak at about 480 Hz. The RANS models predict the first three peaks, while the hybrid RANS/LES models predict the first four peaks. The DES model does seem to produce some spurious peaks not seen in the data or in any of the other models. The hybrid RANS/LES models are in much better agreement with the data at the higher frequencies than are the RANS models.

5.4   Planar Shear Layer

One area of great importance for practical application of hybrid RANS/LES models in a production environment is the examination of their failure modes. When, for whatever reason, one has a fine grid but little or no unsteadiness is reaching that part of the domain, it is important that the turbulence model "fail" in a benign way. In the current work, it has been observed that the DES model tends to revert to a laminar solution (away from walls), while the hybrid model falls back to something closer to a standard RANS solution. Illustrative of this are the results of 3-D simulations using the NXAIR RANS flow solver of the same mixing layer case discussed in Chapter 3. Plots of mixing layer thickness are shown in Fig. 5.21. The coarse grid dimensions in this case were $188 \times 106 \times 61$ and for the fine grid the dimensions were $188 \times 106 \times 141$. The fine grid spanwise spacing is half that of the coarse grid at the center of the duct. Both cases were run without any sort of forcing or pseudo-turbulence at the inflow that would trigger chaotic 3-D behavior. For the coarse grid, all but the DES model are predicting

a reasonable RANS mixing layer solution. The DES model is underpredicting the growth somewhat. The situation is even more striking for the fine grid, however, where the DES model is clearly predicting a laminar solution. In contrast, the hybrid SST model, although it does show some deviation from the RANS models, is still predicting mixing layer growth along the lines of a turbulent RANS simulation.

If this trend holds up in further testing, then it would represent a clear advantage for the hybrid model over the DES model. This is especially true since, for complex production applications, grid quality is often impossible to maintain over the entire domain. As long as sufficient resolution is present to capture the unsteady features of interest in the region of interest, it is often acceptable for the rest of the domain to revert to, in effect, a turbulent RANS solution. A reversion to laminar flow, however, would not be acceptable for many applications.

5.5   Conclusions

The hybrid RANS/LES models provided reasonable agreement with the data in all cases, and consistently predicted higher unsteady energy levels than did the traditional RANS models. The hybrid models also predicted lower minimum pressures in vortex cores than did the RANS models, which indicates that they can be used to remove a known restriction of RANS type models.

(a) SST Model

(b) Hybrid SST Model

(c) Spalart-Allmaras Model

(d) DES Model
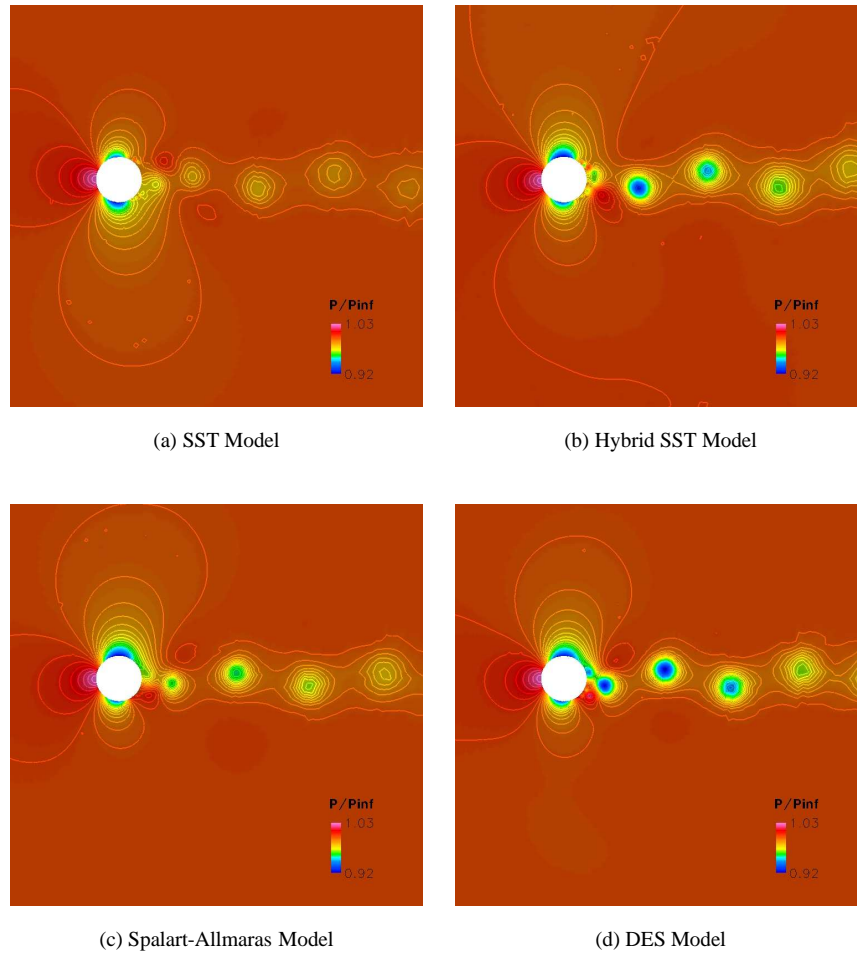
Figure 5.1: Instantaneous Pressure Contours for a Circular Cylinder for $M = 0.2$ and $Re_d = 8.0 \times 10^6$
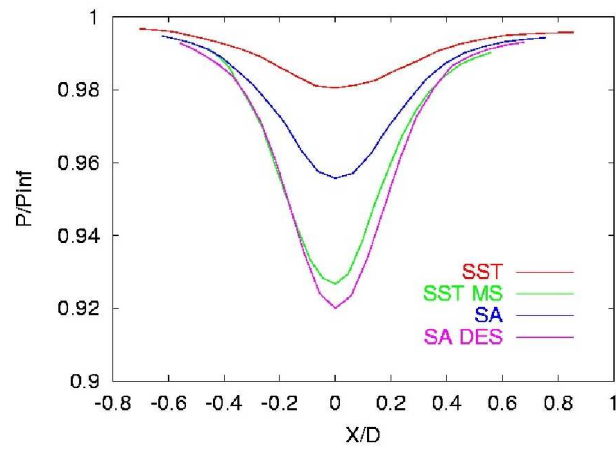
Figure 5.2: Pressure Distribution Across the Nearest Shed Vortex of a Circular Cylinder at $M = 0.2$ and $Re_d = 8.0 \times 10^6$

(a) SST Model

(b) Hybrid SST Model

(c) Spalart-Allmaras Model

(d) DES Model
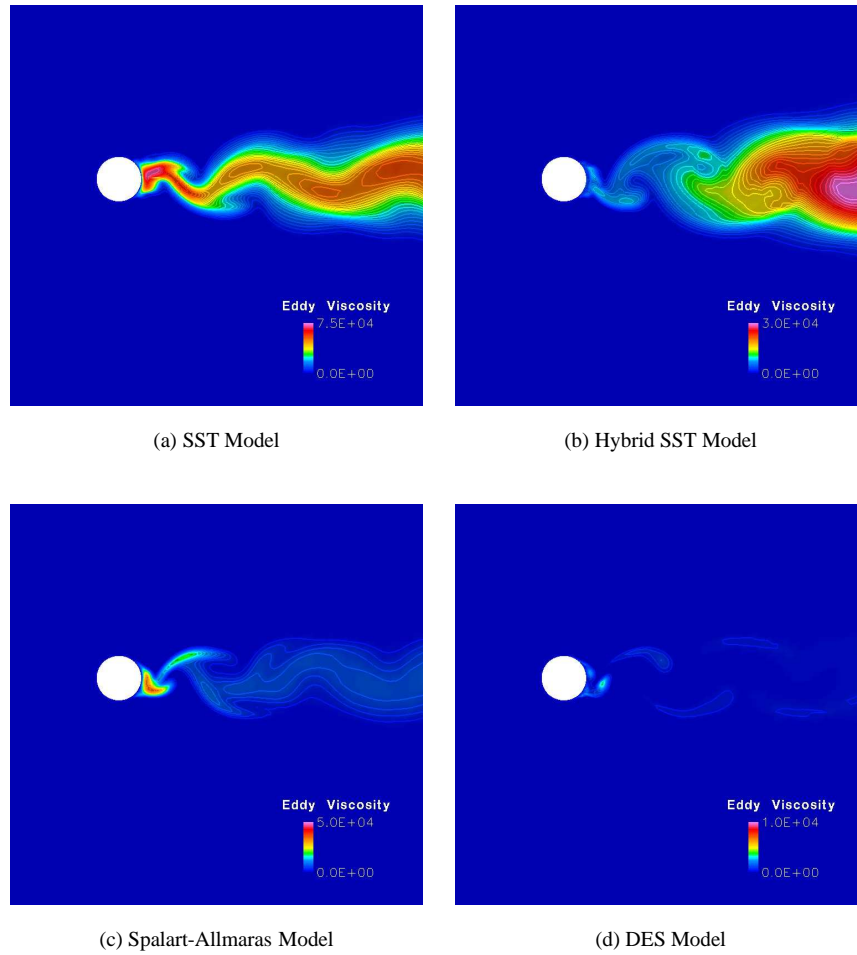
Figure 5.3: Instantaneous Eddy Viscosity Contours (Nondimensionalized by Free Stream Molecular Viscosity) for a Circular Cylinder at $M = 0.2$ and $Re_d = 8.0 \times 10^6$
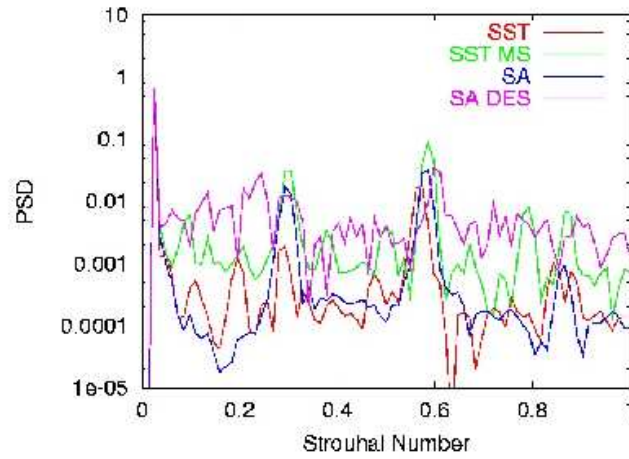
Figure 5.4: PSD for the Circular Cylinder Axial Force at $M = 0.2$ and $Re_d = 8.0 \times 10^6$
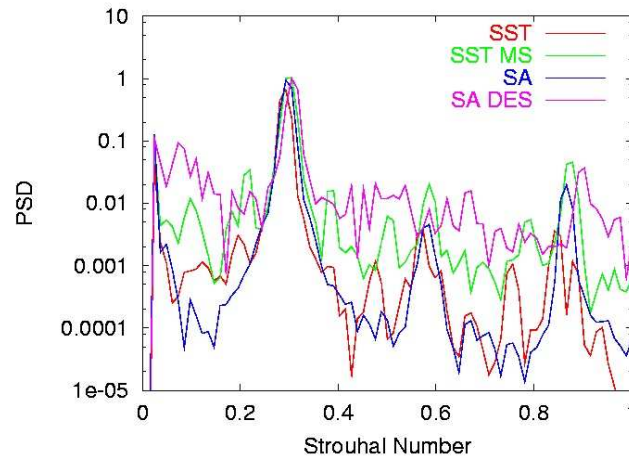
Figure 5.5: PSD for the Circular Cylinder Normal Force at $M = 0.2$ and $Re_d = 8.0 \times 10^6$

(a) SST Model

(b) Hybrid SST Model

(c) Spalart-Allmaras Model

(d) DES Model
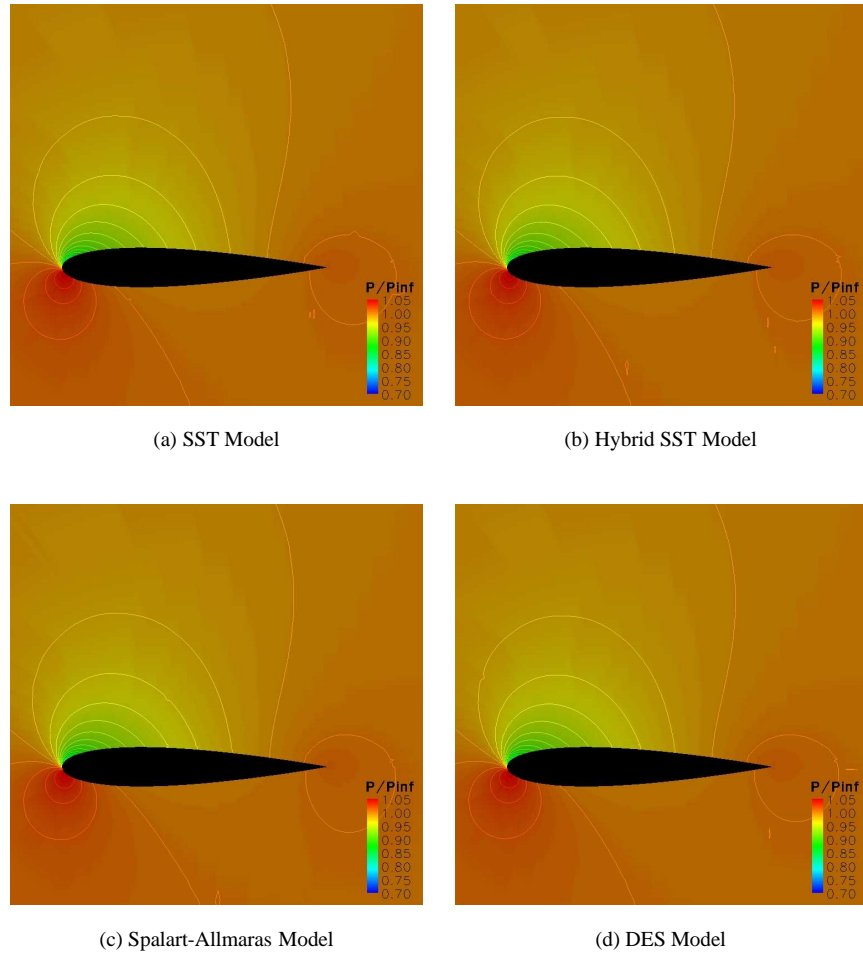
Figure 5.6: Pressure Contours on a NACA 0015 airfoil at $\alpha = 7.92°$ on the Down Stroke Oscillating About $\alpha_0 = 4°$ with $K = 0.1$

49
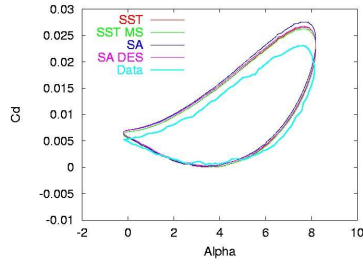
(a) Drag Coefficient

(b) Lift Coefficient

(c) Moment Coefficient

Figure 5.7: Forces and Moments on a NACA 0015 Airfoil Oscillating About $\alpha_0 = 4°$ With a Reduced Frequency of $K = 0.1$

(a) SST Model

(b) Hybrid SST Model

(c) Spalart-Allmaras Model

(d) DES Model
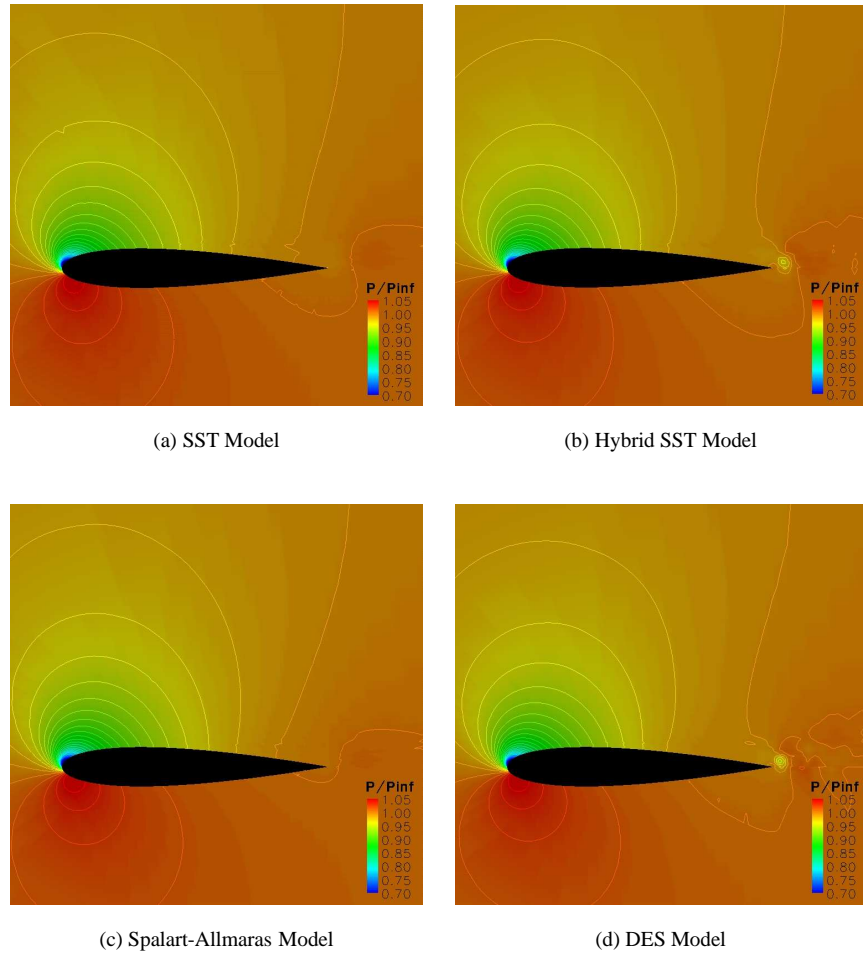
Figure 5.8: Pressure Contours on a NACA 0015 airfoil at $\alpha = 14.93°$ on the Up Stroke Oscillating About $\alpha_0 = 11°$ with $K = 0.1$

51

(a) SST Model

(b) Hybrid SST Model

(c) Spalart-Allmaras Model

(d) DES Model
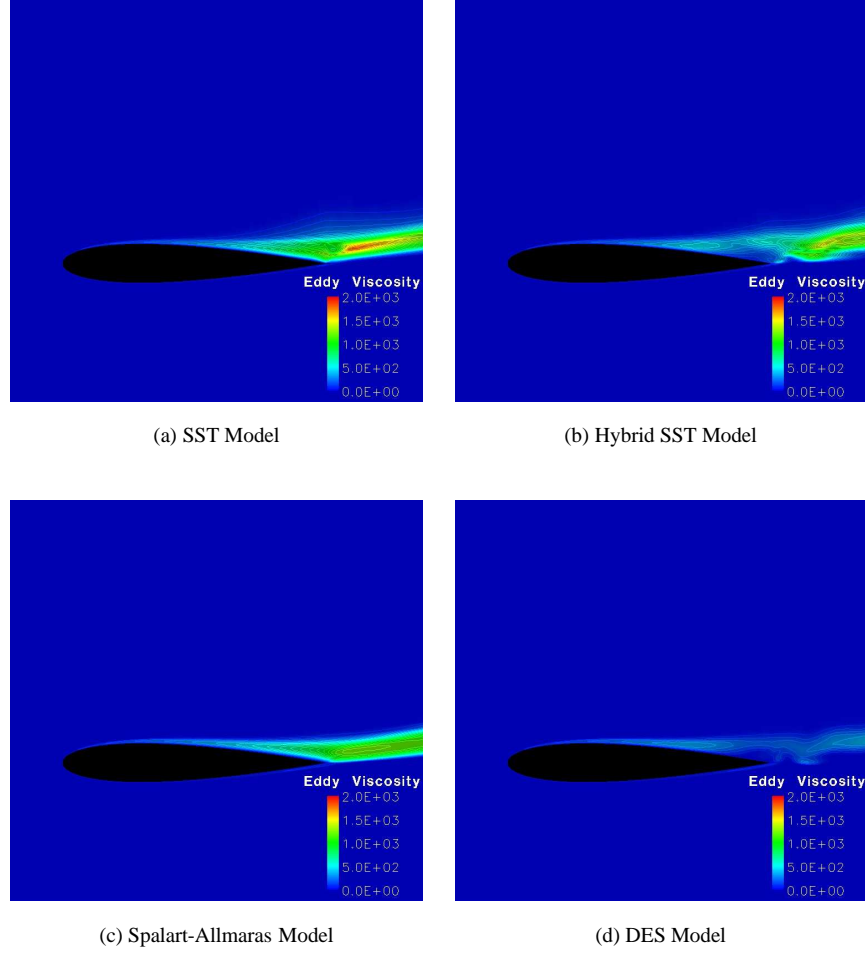
Figure 5.9: Eddy Viscosity Contours on a NACA0015 airfoil at $\alpha = 14.93°$ on the Up Stroke Oscillating About $\alpha_0 = 11°$ with $K = 0.1$
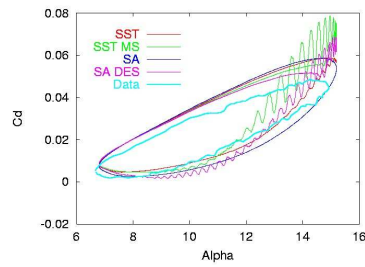
(a) Drag Coefficient
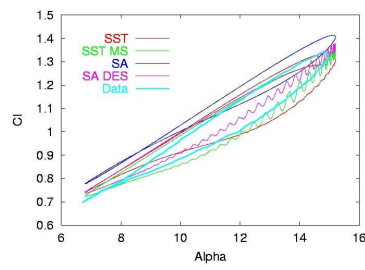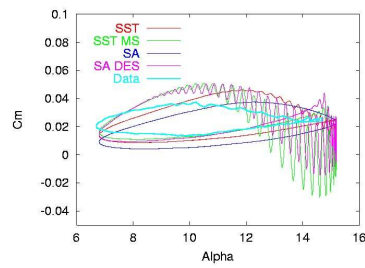
(b) Lift Coefficient

(c) Moment Coefficient

Figure 5.10: Forces and Moments on a NACA 0015 Airfoil Oscillating About $\alpha_0 = 11°$ With a Reduced Frequency of $K = 0.1$

53
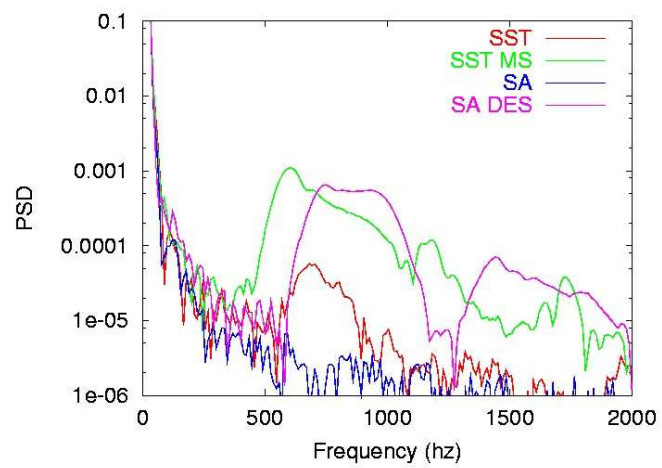
Figure 5.11: Predicted PSD for the Normal Force on a NACA 0015 Airfoil Oscillating About $\alpha_0 = 11°$ With a Reduced Frequency of $K = 0.1$

(a) SST Model

(b) Hybrid SST Model

(c) Spalart-Allmaras Model

(d) DES Model
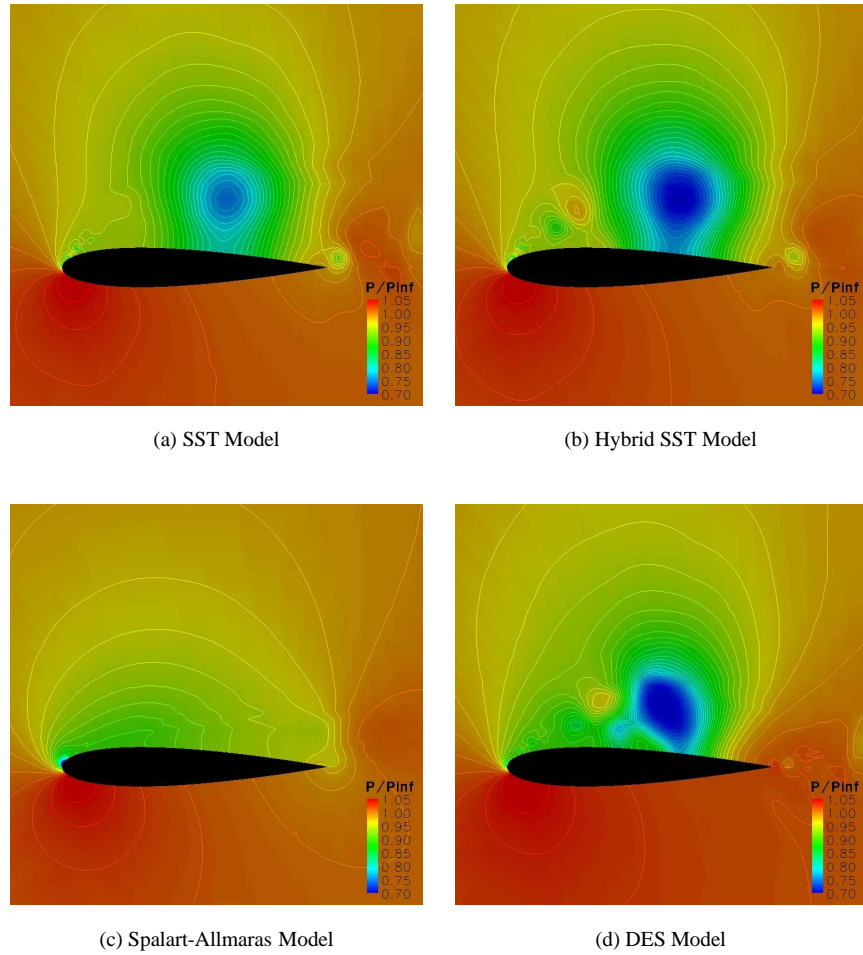
Figure 5.12: Pressure Contours on a NACA 0015 airfoil at $\alpha = 18.92°$ on the Down Stroke Oscillating About $\alpha_0 = 15°$ with $K = 0.1$

(a) SST Model

(b) Hybrid SST Model

(c) Spalart-Allmaras Model

(d) DES Model
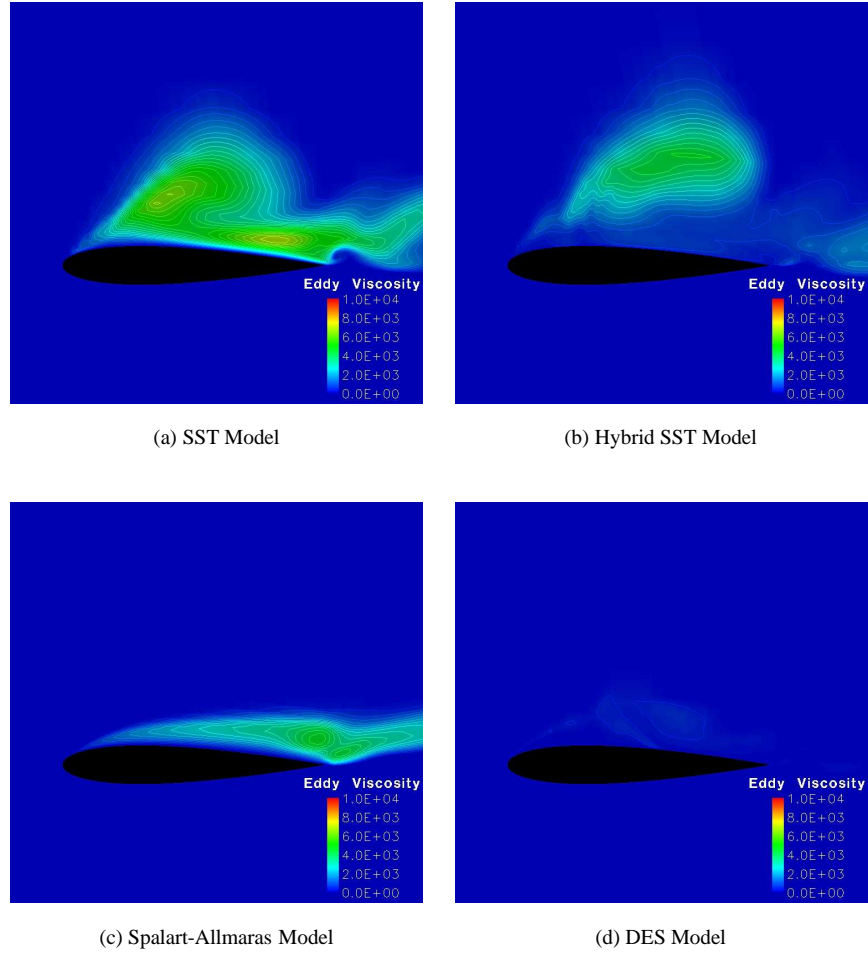
Figure 5.13: Eddy Viscosity Contours on a NACA 0015 airfoil at $\alpha = 18.92°$ on the Down Stroke Oscillating About $\alpha_0 = 15°$ with $K = 0.1$
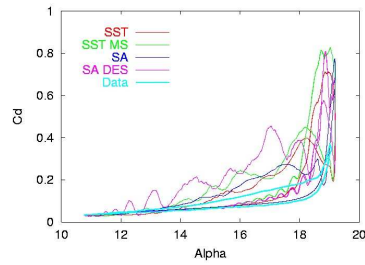
(a) Drag Coffi cient

(b) Lift Coeffi cient

(c) Moment Coeffi cient

Figure 5.14: Forces and Moments on a NACA 0015 Airfoil Oscillating About $\alpha_0 = 15°$ With a Reduced Frequency of $K = 0.1$
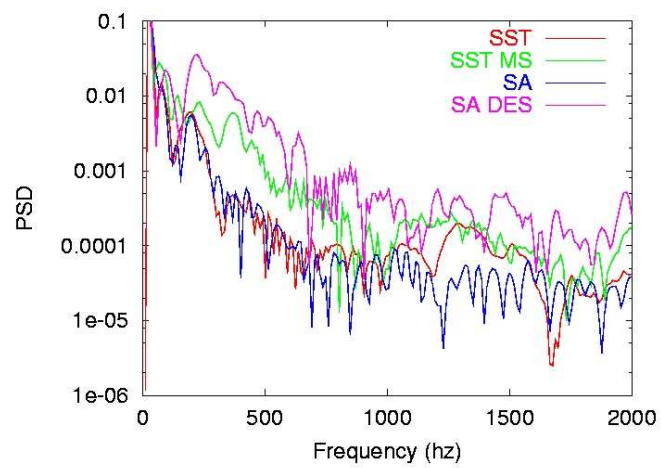
Figure 5.15: Predicted PSD for the Normal Force on a NACA 0015 Airfoil Oscillating About $\alpha_0 = 15°$ With a Reduced Frequency of $K = 0.1$

(a) SST Model

(b) Hybrid SST Model

(c) Spalart-Allmaras Model

(d) DES Model
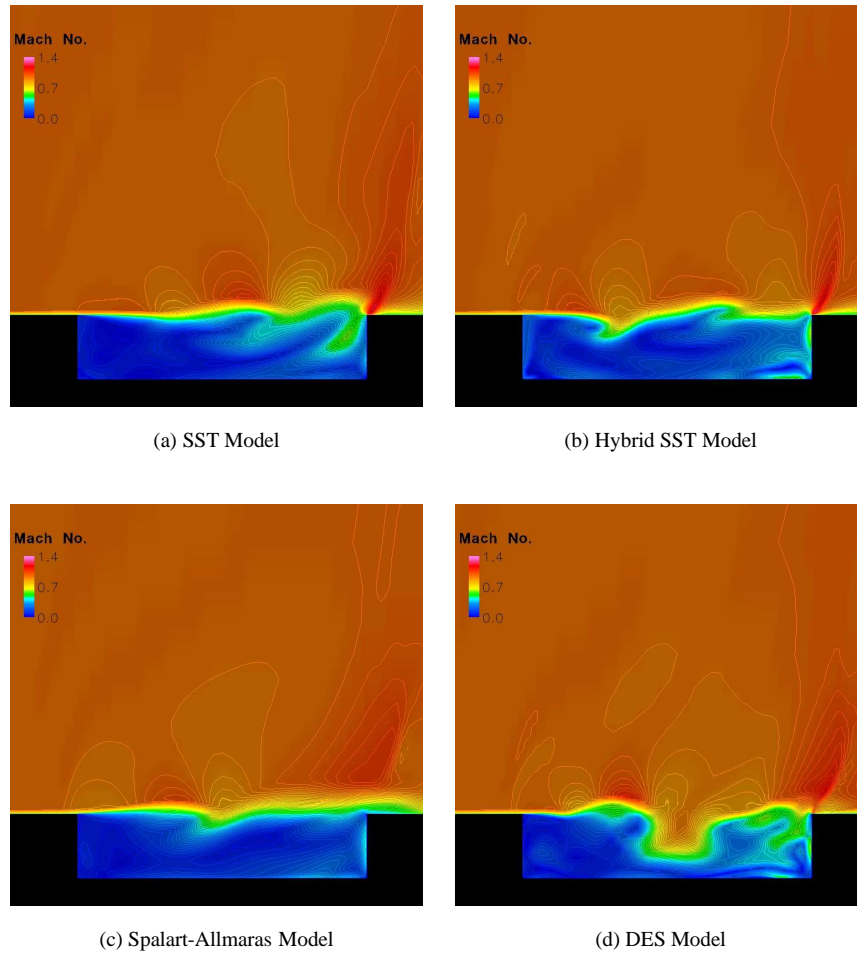
Figure 5.16: Instantaneous Mach Number Contours on the WICS Bay Centerline for $M = 0.95$

(a) SST Model

(b) Hybrid SST Model

(c) Spalart-Allmaras Model

(d) DES Model
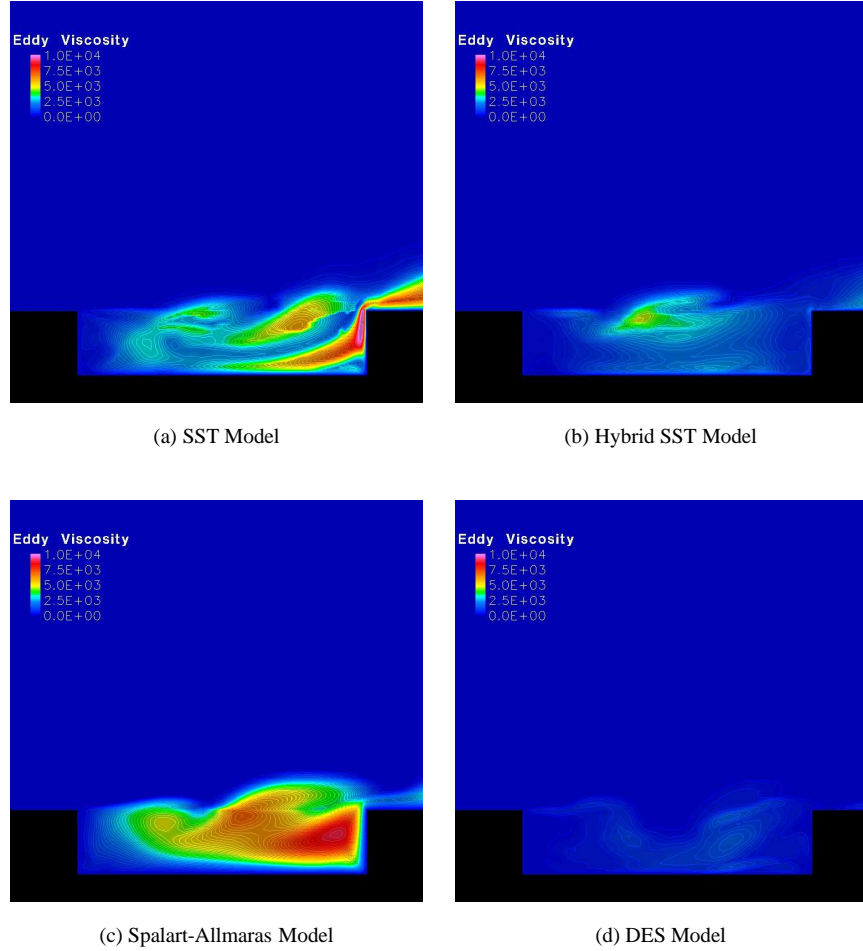
Figure 5.17: Instantaneous Eddy Viscosity Contours on the WICS Bay Centerline for $M = 0.95$

(a) SST Model

(b) Hybrid SST Model

(c) Spalart-Allmaras Model

(d) DES Model
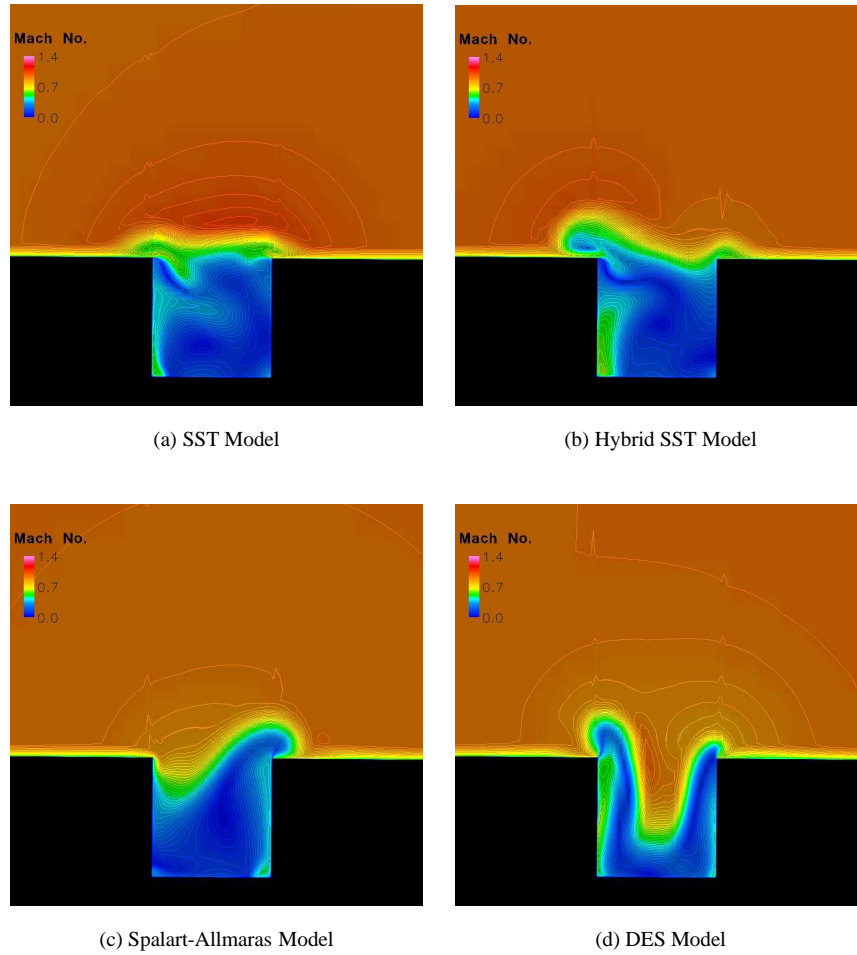
Figure 5.18: Instantaneous Mach Number Contours at $x/D = 0.6$ for the WICS Bay at $M = 0.95$

a) Front Wall
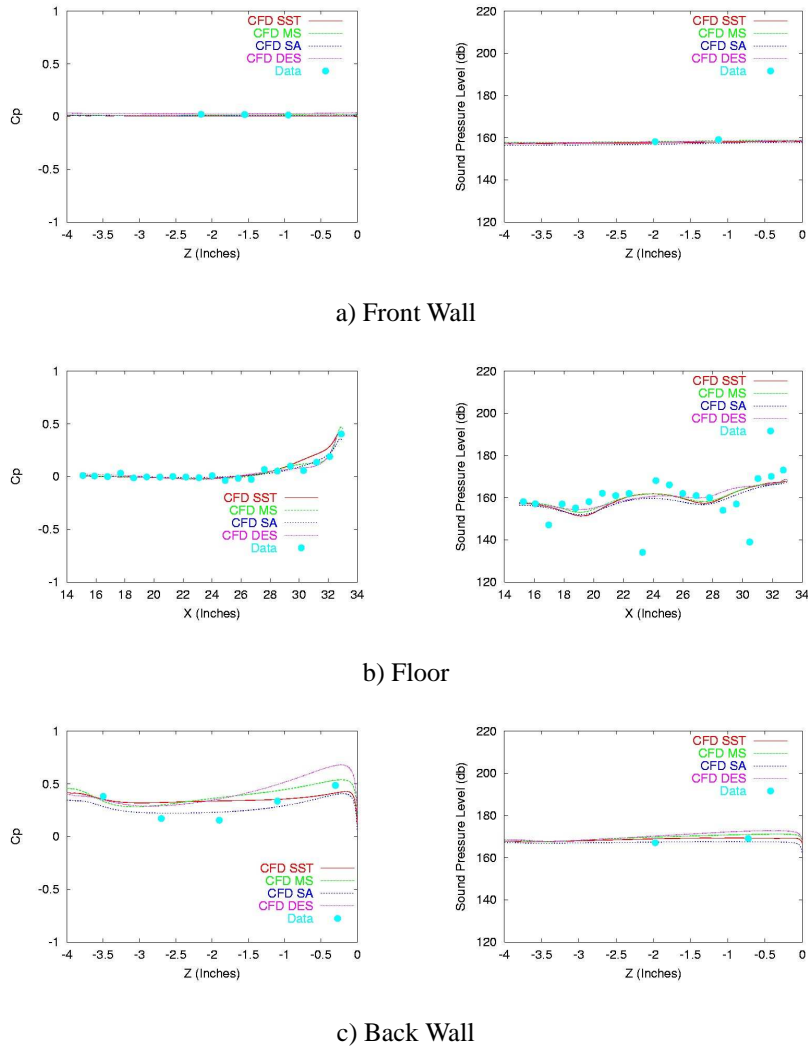
b) Floor

c) Back Wall

Figure 5.19: Time Averaged Pressure Coefficient and Sound Pressure Level on the WICS Bay Centerline
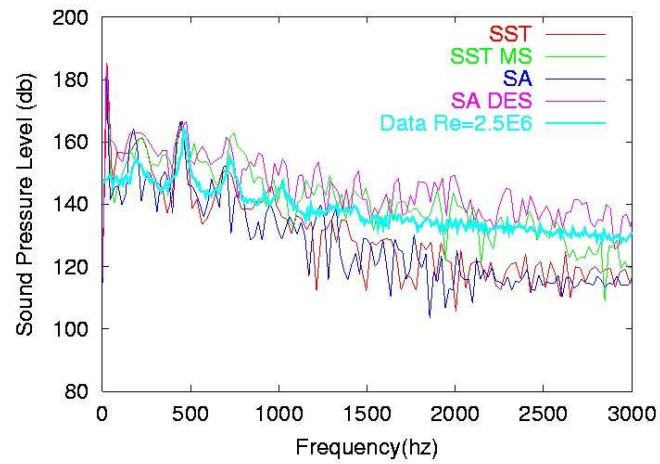
(a) WICS bay floor centerline $X/L = 0.985$
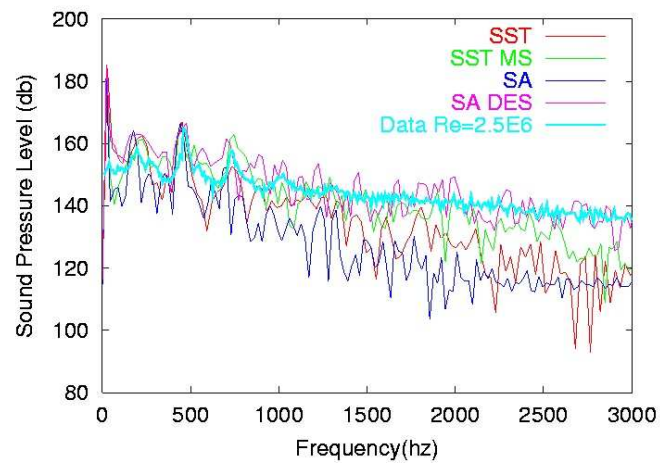
(b) WICS bay back wall centerline at $Z/H = 0.82$

Figure 5.20: FFT for two locations in the WICS bay at $M = 0.95$
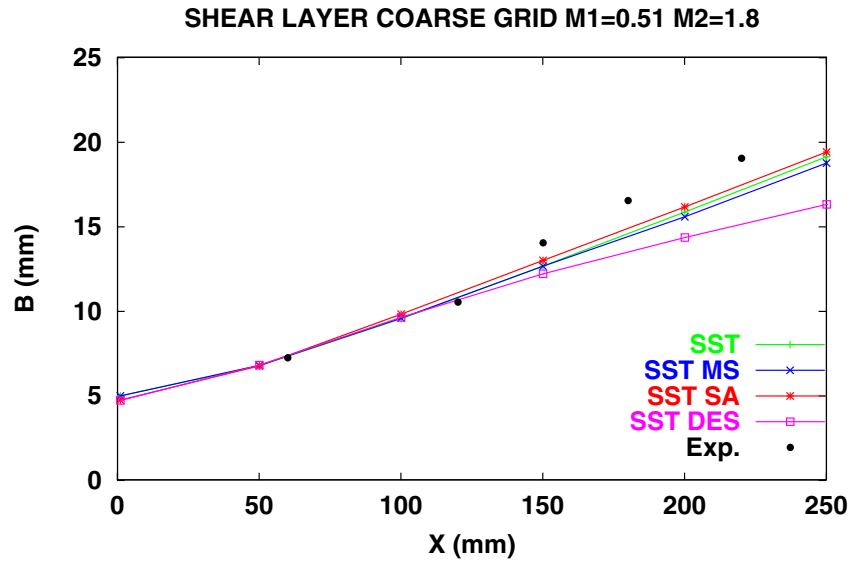
(a) Coarse Grid
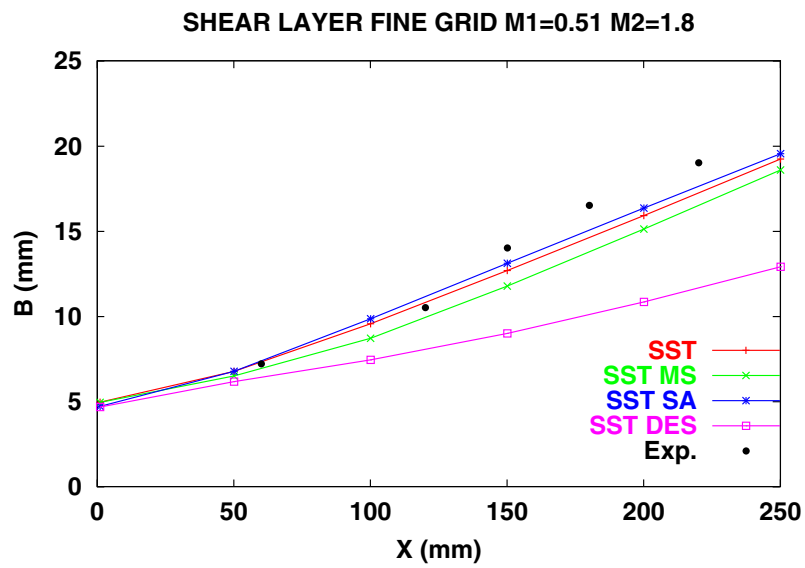
(b) Fine Grid

Figure 5.21: Mixing Layer Growth Rate Predicted Using a RANS Flow Solver With No Inflow Perturbations

Chapter 6

Code Verification Using the Method of Manufactured Solutions

6.1   Introduction

As mentioned earlier, technology transition has been a major component of this project from the beginning. It is not sufficient to merely run simplified cases using a research code; The resulting technology must be transitioned to a production flow solver if at all possible. As discussed above, the flow solver chosen for this effort was the Wind-US code. Wind-US is a relatively large and complex code with numerous options for almost every aspect of a CFD simulation. As is characteristic of complex systems, it has in the past been found that updates to fix one problem often cause other problems. It therefore becomes very important to verify that the algorithms required to perform the Facility Unsteadiness Research project remain functional through all the code modifications. Indeed, much time was spent in FY2004 tracking down a problem which resulted in Newton iterations not working properly in combination with the second order implicit time marching scheme. The Method of Manufactured Solutions has been found to be extremely useful in this regard, and therefore this section covering it is included in this final report.

6.2   Overview of the Method of Manufactured Solutions

The analysis of error in computational fluid dynamics (CFD) codes can be divided into two general categories: verification and validation. Validation refers to whether the correct equations are solved for the problem at hand. For example, a linear Euler solver will not be able to accurately resolve strong shocks, no matter how well implemented. Verification addresses the issue of whether or not the chosen governing equations are solved correctly. In verifying CFD results, one must address such things

as the sufficiency of grid resolution, completeness of convergence (or accuracy of time marching), and the presence (or not) of coding errors.

One tool for code verification which has only recently begun to be applied to large, general-purpose flow solvers is the method of manufactured solutions (MMS). This technique is a rigorous method for finding and eliminating coding mistakes. While any given series of MMS runs can only examine a subset of the available options in a modern production flow solver, within that subset, the results that it yields are fairly conclusive. MMS was originally developed by Roache and Steinburg[32] and extended by Roache et al.[33]. The term "manufactured" solutions was coined by Oberkampf and Blottner[34] and refers to the fact that the solutions are arbitrarily chosen (or manufactured). The governing equations are then modified by the addition of source terms such that the manufactured solution satisfies the governing equations. The work of Salari and Knupp[35] contains a detailed discussion of MMS as applied to a variety of partial differential equations.

The actual application of the method of manufactured solutions is now discussed in somewhat more detail. The overall procedure is as follows:

- Choose the form of the governing equations

- Chose the form of the manufactured solution

- Apply the governing equations to the manufactured solution to generate analytical source terms

- Solve the equations on multiple mesh levels using the source terms

- Evaluate the global discretization error in the numerical solutions

- Determine the order of accuracy

The analytical solutions can be almost anything, but to be useful, they must at least satisfy the following conditions:

- They must be continuous. Current numerical schemes all reduce to first order at discontinuities–if they can handle them at all.

- Each variable in the solution must be continuously differentiable up to the order of the corresponding terms in the governing equations. One can only test the terms of the governing equations for which the solutions give non-zero contributions

- The Taylor series expansion of the solutions must include non-zero terms at least up to the purported order of the numerical scheme to be tested. As above, only non-zero contributions from the manufactured solutions can be tested.

- In addition, for best effect, the contribution from each term in the governing equations should be of the same order of magnitude. This prevents the larger terms from masking errors in other terms of smaller magnitude. For example, in the current work, when the Navier-Stokes equations are solved, the viscosity is fixed at a value of $10 \, N \cdot s/m^2$ in order to bring the contribution of the viscous terms up to the level of the inviscid terms.

- In order to avoid numerical problems, the solutions should avoid negative values of quantities which should physically only be positive (e.g. pressure, density, and temperature).

For the cases discussed here, the analytical solutions were chosen to be functions of sines and cosines designed such that each term in the governing equations to be examined (either the Euler equations or the laminar Navier-Stokes equations) would produce a non-zero value. For the Euler equations, the manufactured solution for each specified variable was of the form:

$$\phi_{Euler}(x,y,z) = \phi_0 + \phi_x f_{\phi_x}\left(\frac{(a_{\phi_x}x+c_x)\pi}{L}\right) + \phi_y f_{\phi_y}\left(\frac{(a_{\phi_y}y+c_y)\pi}{L}\right)$$
$$+ \phi_z f_{\phi_z}\left(\frac{(a_{\phi_z}z+c_z)\pi}{L}\right) \tag{6.1}$$

where $\phi = \rho$, u, v, w, or p and the f functions denote either the sine or cosine function. L is a reference length (taken as 1 m here). The various ϕ's, a's, and c's that appear on the right hand side are constant coefficients. Note that subscripts do not denote differentiation in this case. The constants used in the various tests of the Euler equations solver are contained in Tables 6.1, 6.2, 6.3, and 6.4.

For the Navier-Stokes solutions, the solutions take the form of the Euler equations solutions with additional cross terms added to ensure that the viscous terms are fully exercised:

$$\phi_{NS}(x,y,z) = \phi_{Euler}(x,y,z) + \phi_{xy}f_{\phi_{xy}}\left(\frac{a_{\phi_{xy}}\pi xy}{L^2}\right) + \phi_{xz}f_{\phi_{xz}}\left(\frac{a_{\phi_{xz}}\pi xz}{L^2}\right)$$
$$+ \phi_{yz}f_{\phi_{yz}}\left(\frac{a_{\phi_{yz}}\pi yz}{L^2}\right) \tag{6.2}$$

The constants used for the Navier-Stokes equations tests are shown in Tables 6.5, 6.6, 6.7, and 6.8.

A symbolic manipulation software package was used to analytically differentiate the general manufactured solution (either equation 6.1 or 6.2) according to the governing equations. Since the manufactured solutions do not actually solve the governing equations, this will result in extra terms which are then added as source terms to drive the solution toward the specified manufactured solution. As the source terms are quite complex, space considerations prevent them being included in this report.

6.3 Numerical Scheme

Wind-US contains, among other things, a structured compressible Navier-Stokes solver. It uses a finite volume discretization in the solution of the governing equations. Interior mesh points are treated as cell centers and the corners that define a given control volume around them are computed by averaging the coordinates of neighboring cell centers. With this information, cell volumes and face areas can be readily computed.

On the boundaries, however, Wind-US uses a technique that was inherited from the NASTD code. Rather than solving half cells at boundaries, the nearest interior cell is enlarged to reach all the way to the boundary. Therefore, if a uniform grid is input, this results in so-called "fat" cells at boundaries, as illustrated in Fig 6.1. These fat cells have two main drawbacks: first, they introduce a discontinuity in in the grid spacing at the boundaries, and second, the nominal "center" of a fat cell is not actually at the center of mass of the volume (even on a uniform grid). Both of these issues are potential sources of error. In order to avoid these problems in the current work, a preprocessor has been employed which reads in a smooth well-defined nodal grid, computes cell centers, and then adds a fringe of boundary points around the edges. When such a grid is loaded into Wind-US, its internal scheme will create a more uniform set of finite volumes (see Fig. 6.2). For a truly uniform Cartesian nodal grid, the resulting "cell-centered" grid has uniform volume and the cell centers are exactly in the center of mass. Thus, Wind-US behaves much like a cell-centered finite-volume code although the internal algorithm remains node-centered.

By default Wind-US uses a Roe scheme on the right hand side with a flux extrapolation algorithm that attempts to account for grid stretching to maintain its order on non-uniform meshes. For the Navier-Stokes results, the viscous fluxes are evaluated at cell faces using a central-difference scheme. This results in an overall scheme which, on uniform meshes is formally second order accurate in space. While it can be run explicitly, Wind-US is by default an implicit code, and the standard inversion method is an approximate factorization scheme. Although there are numerous alternatives for both the right and left hand side, the discussion here will attempt to focus on the code options of interest when running large scale unsteady simulations. Additional information about the numerics of the structured portion of the Wind-US code may be found in the work of Bush[36], Bush et al.[37], and Power and Underwood[38].

6.4 Test Cases

MMS has been used to test the Wind-US flow solver in several configurations. The first set of cases were run on a two-dimensional uniform Cartesian mesh using the default numerical scheme. For the two-dimensional cases, results were obtained (or attempted) for seven resolutions ranging from 8×8 to 128×128. The domain for all these cases was a one meter square. Previous applications of MMS to the Wind solver for 2-D supersonic Euler and subsonic Navier-Stokes flows have been performed by the Roy et al.[39]. For the current work, multi-block versions of the same cases were run to assess the effect of block-to-block coupling on the scheme's overall order of accuracy. Also, for this work, subsonic Euler and supersonic Navier-Stokes cases are investigated. Similar runs are also performed on 3-D versions of the above cases. For the 3-D runs, however, machine limitations prevented the running of $96 \times 96 \times 96$ and $128 \times 128 \times 128$ single block grids. A multi-block version of the $96 \times 96 \times 96$ case was generated using eight $48 \times 48 \times 48$ grids.

Of particular interest for this project are the higher order algorithms available in the code. Thus, the third, fourth, and fifth order schemes for computing inviscid fluxes have been tested.

Finally, the order of accuracy of the Wind-US code on curvilinear grids is investigated. The grid used for the curvilinear test case was originally designed for an internal duct flow. It features clustering and curvature to some degree in all three coordinate directions.

For all of the subsonic cases, outer boundaries were specified to match the prescribed manufactured solutions. For the supersonic cases, however, outflow boundaries were solved using the code's normal supersonic outflow boundary condition (which simply extrapolates variables from the interior) unless otherwise noted.

6.5 Results

Results for the 2-D supersonic Euler case using the default numerical scheme of Wind-US are shown in Fig. 6.3. The L_2 norm of the error at convergence is plotted for the conserved variables at various grid resolutions. The results for single block grids are shown with open symbols, while the filled symbols represent a multi-block run (the 96×96 grid was split into four equal parts). At the higher resolutions (48×48 and above), the code is clearly showing second order convergence. The "bulge" in the curve for the 32×32 grid is caused by the flux limiter activating at this level, which reduces the scheme to first order. The proof of this is found in Fig. 6.4, which has results from the same case, but this time the flux limiter was deactivated. For this case, the code shows second order convergence throughout the range of grids, although for the coarsest grid (with 8×8 resolution) the convergence seems to be dropping off somewhat. Notable on both of these figures, the converged error of the multi-block case is almost identical to the corresponding single block case. The differences that exist are due to the implicit scheme not having information available from the entire domain when it solves each block in the multi-block case. The equivalent three-dimensional case produced, as expected, much the same behavior as the two-dimensional results (see Fig. 6.5).

Results from the subsonic Euler case are shown in Fig. 6.6 for two dimensions and Fig. 6.7 for three. For both these cases, the code clearly demonstrates second order convergence. Again, the equivalent multi-block solutions also appear to be behaving much like their single-block counterparts.

The first Navier-Stokes case to be examined is the subsonic case. Figure 6.8 shows the results from the 2-D case. The convergence rate at the coarser resolutions appears to be somewhat less than second order (but better than first order). At higher resolutions, however, the curve approaches a second order slope, indicating that with sufficient resolution, the theoretical order can be achieved. The results from the equivalent 3-D case are shown in Fig. 6.9. As with the 2-D case, the code shows clear second order behavior. For both of these cases, the multi-block runs failed to complete. This is because the algorithm that Wind-US uses to communicate between abutting boundaries currently only passes the inviscid fluxes. When the viscous fluxes are of the same magnitude as the inviscid fluxes (as in this case), the coupling mechanism breaks down. It should be noted that, in theory, the overlapped coupling in Wind-US has no such limitations, but this has yet to be tested using MMS.

The power of MMS as a verification tool was highlighted by the results from the

69

2-D supersonic Navier-Stokes test case. Figure 6.10 the convergence of the original, default scheme with first order extrapolation at outflow boundaries. As the figure makes painfully clear, Wind-US was not behaving as a second order code at all. Since the Euler cases already verified the inviscid fluxes as being correct, and the subsonic Navier-Stokes case seemed to indicate that the viscous terms were also correct, suspicion quickly focused on the outflow boundary condition (recall that the subsonic case specified the exact solution on outflow boundaries where the supersonic case uses Wind-US's normal outflow boundary condition). To test this, the case was re-run using zeroth order extrapolation on the outflow.

As seen on Fig. 6.11, these results are markedly different than the previous, and indeed show something of a zeroth order rate of convergence at the higher resolutions. This indicates that not only was the outflow boundary affecting the solution (via the viscous terms), but that at higher resolutions it was the dominant factor. Upon examination, the extrapolation algorithm was found to have two significant bugs. First of all, the basic algorithm was inappropriate for the pseudo-cell-centered grid which was being employed. Second, an attempt was being made to apply a flux limiter to the extrapolation, and this algorithm was completely unsuitable for the task. Having fixed these two problems, the case was re-run with first order extrapolation on the boundaries. Figure 6.12 shows that these changes resulted in a dramatic improvement in the error. The code now clearly shows roughly second order convergence on the coarse grids, while the fine grids have a first order convergence rate.

Seeing that the Euler case had been affected by the presence of the flux limiter, it was decided to re-run these cases without it. As Fig. 6.13 shows, there was little or no difference in the results. This led to the conclusion that the outflow boundaries must be the source of the first order behavior. To prove that the influence of the boundary was driving the first order results, a final set of runs was made which specified the analytic solution on all boundaries. The results from this case (shown in Fig. 6.14) strongly indicate that it is in fact the first order nature of the boundary condition which was driving the previously observed behavior. The slight glitch at the highest resolutions resisted explanation until very recently, when this case was rerun using the Koren limiter. With the Koren limiter engaged, the results (in Fig. 6.15) show fully second order behavior throughout the range of grid. It appears that the bump that appears when either the default TVD limiter or no limiter at all is used is due to error building up in the domain that the scheme cannot naturally dissipate. The default Superbee limiter, which should counter this noise is, it appears, capable of introducing noise of its own into the solution (counter to its design). An equivalent set of three-dimensional grid runs was made using the first order boundary condition. As one would expect, the results (shown in Fig. 6.16) are very much in line with the 2-D case.

The multi-block results for the supersonic Navier-Stokes cases were somewhat mixed. With the buggy first order or the zeroth order boundary conditions, the multi-block results were not too different from the single block. As the boundary condition's effects are reduced, however, the problems with the inviscid-only block coupling algorithm become more evident. Interestingly, the 3-D run did not show as much variation, although with only one data point, nothing is conclusive. Up until now, only abutting, point-matched boundaries have been considered. Wind-US is also capable of computing overlapped boundary conditions with fringes of arbitrary size. In theory,

a point-matched double fringe overlapped zonal coupling configuration ought to enable fully second order behavior throughout the domain. To test this, the 3-D subsonic Navier-Stokes case was re-run after splitting the grids into eight blocks each. As the results in Fig. 6.17 show, second order behavior was predicted in this configuration. Note that for this case, it was necessary to run with "fat cells" at the boundaries in order to ensure that the overlapping regions were point-matched. This results in an increased error, as can be seen by comparing with Fig. 6.9. The L_2 norm of the error is, on average, increased by roughly a factor of two for the case with "fat cells".

For the facility unsteadiness work, it would be desirable to have the option of running even higher order schemes (at least in regions where the flow is smooth). Therefore, the third, fourth, and fifth order upwind-biased schemes were investigated. The first results obtained with the third order scheme (in Fig. 6.18) show, surprisingly, a second-order convergence pattern. Suspecting more limiter problems, the case was rerun without a TVD limiter. The results, shown in Fig. 6.19, indicate that the base scheme is correctly third order. The question arose, however, as to whether or not there was something inherently second order about the way limiters are implemented in Wind-US. To test this, the Koren limiter was used for another sequence of runs. This case showed (Fig. 6.20) that the problems were due to something specific to the default limiter, and that, provided the solution was smooth, the Koren limiter allows third order behavior.

For the fourth and fifth order schemes, no TVD limiting is available, so none of the problems seen with the second and third order schemes were expected. As shown in Fig. 6.21, however, while it appears that the coarsest grids show approximate fourth order convergence, a strongly second order behavior is seen on the finer grids. For the fifth order scheme, the second order behavior is even more dominant (see Fig. 6.22). The preliminary analysis of this problem indicated that it was due to a lack of numerical precision. The error level for these schemes is a factor of two smaller than for the third order scheme, and an order of magnitude less than the default second order scheme. Also, the behavior at the finer resolutions is very similar for both the fourth and fifth order schemes. Some efforts were made to increase the variability of the manufactured solution, in order to increase the error magnitude, but only the coarsest grids were affected. This indicated that numerical precision was at issue, but this could not be fully tested until a double precision version of the code became available FY2004.

When the fourth and fifth order cases were re-run using a double precision version of Wind-US, it was found that the solution error did indeed show some effects from precision. With the double precision code, it was possible to converge the solution at least a further six orders of magnitude. The enabled a clear separation of the residual error (due to lack of convergence) and the error due to the limitations of the numerical scheme. Unfortunately, the overall error levels remained virtually unchanged. The source of the second order behavior in the higher order schemes, therefore, remains a mystery.

Finally, some preliminary MMS runs have been made with a curvilinear grid. The grid (and converged density contours) are shown in Fig. 6.23. This grid was originally used for duct simulations. The topology is that of an H-C grid, with a singular axis running down the middle of the duct. As Fig. 6.24 shows, on this grid, the convergence appears to fall somewhere between first order and second. This is probably the best

that can be hoped for, since the physical space-based extrapolation does not take grid curvature into account.

6.6   Conclusions

The method of manufactured solutions has thus far been employed to verify the theoretical order of accuracy for several of the algorithms available in the Wind-US flow solver. Based on the results presented above, one can conclude that, absent intervention from the flux limiter or the build-up of spurious noise in the solution, the default interior scheme of Wind-US has been shown to be second order accurate on uniform grids for inviscid flow. Likewise, the third order scheme is clearly correctly implemented, although in that case, the Koren limiter must be used if TVD limiting is required. For the fourth and fifth order schemes, it appears that a double precision version of the code will be required to verify the order of accuracy. There are also strong indications that, for inviscid flow, the block-to-block coupling scheme is also second order (as advertised), at least for point-matched grids.

For the viscous cases, it has been shown that the interior viscous scheme is second order. The block coupling algorithm, as expected, does not perform well for abutting grids when significant viscous terms are present.

The experience with the supersonic Navier-Stokes case clearly shows the power of MMS to identify coding problems and verify that they have been fixed. It also served as a reminder that, no matter what the nominal order of the scheme, the results cannot exceed the accuracy of the boundary conditions when those boundary conditions are capable of influencing the interior grid.

Results from general curvilinear grids indicate that, on a smooth grid with reasonable grid resolution, the default scheme while not fully second order accurate, is at least better than first order.

Variable	ϕ_0	f_{ϕ_x}	ϕ_x	a_{ϕ_x}	c_x	f_{ϕ_y}	ϕ_y	a_{ϕ_y}	c_y
$\rho\ (kg/m^3)$	1	sin	0.15	1	$\frac{1}{3}$	cos	-0.1	0.5	0.5
$u\ (m/s)$	70	sin	5	1.5	1	cos	-7	0.6	0
$v\ (m/s)$	90	cos	-15	0.5	1.5	sin	8.5	$\frac{2}{3}$	1
$p\ (N/m^2)$	1×10^5	cos	0.2×10^5	2	0	sin	0.5×10^5	1	1.4

Table 6.1: Manufactured solution coefficients for 2-D subsonic Euler cases

Variable	ϕ_0	f_{ϕ_x}	ϕ_x	a_{ϕ_x}	c_x	f_{ϕ_y}	ϕ_y	a_{ϕ_y}	c_y
$w\ (kg/m^3)$	80	sin	10	$\frac{1}{3}$	0	sin	2	1.5	1.25

Variable	f_{ϕ_z}	ϕ_z	a_{ϕ_z}	c_z
$\rho\ (kg/m^3)$	sin	-0.12	1.5	0
$u\ (m/s)$	cos	-1.8	0.5	0.5
$v\ (m/s)$	sin	-3	1.25	0.75
$w\ (m/s)$	cos	3.5	1	0.25
$p\ (N/m^2)$	cos	-0.35×10^5	$\frac{1}{3}$	0.75

Table 6.2: Additional Manufactured solution coefficients for 3-D subsonic Euler cases

Variable	ϕ_0	f_{ϕ_x}	ϕ_x	a_{ϕ_x}	c_x	f_{ϕ_y}	ϕ_y	a_{ϕ_y}	c_y
$\rho\ (kg/m^3)$	1	sin	0.15	1	$\frac{1}{3}$	cos	-0.1	0.5	0.5
$u\ (m/s)$	800	sin	50	1.5	1	cos	-30	0.6	0
$v\ (m/s)$	800	cos	-75	0.5	1.5	sin	40	$\frac{2}{3}$	1
$p\ (N/m^2)$	1×10^5	cos	0.2×10^5	2	0	sin	0.5×10^5	1	1.4

Table 6.3: Manufactured solution coefficients for 2-D supersonic Euler cases

Variable	ϕ_0	f_{ϕ_x}	ϕ_x	a_{ϕ_x}	c_x	f_{ϕ_y}	ϕ_y	a_{ϕ_y}	c_y
$w\ (kg/m^3)$	800	sin	15	$\frac{1}{3}$	0	sin	-25	1.5	1.25

Variable	f_{ϕ_z}	ϕ_z	a_{ϕ_z}	c_z
$\rho\ (kg/m^3)$	sin	-0.12	1.5	0
$u\ (m/s)$	cos	-18	0.5	0.5
$v\ (m/s)$	sin	-30	1.25	0.75
$w\ (m/s)$	cos	35	1	0.25
$p\ (N/m^2)$	cos	-0.35×10^5	$\frac{1}{3}$	0.75

Table 6.4: Additional Manufactured solution coefficients for 3-D supersonic Euler cases

Variable	ϕ_0	f_{ϕ_x}	ϕ_x	a_{ϕ_x}	c_x	f_{ϕ_y}	ϕ_y	a_{ϕ_y}	c_y
$\rho\ \left(kg/m^3\right)$	1	sin	0.1	0.75	0	cos	0.15	1	0
$u\ (m/s)$	70	sin	4	$\frac{5}{3}$	0	cos	-12	1.5	0
$v\ (m/s)$	90	cos	-20	1.5	0	sin	4	1	0
$p\ \left(N/m^2\right)$	1×10^5	cos	-0.3×10^5	1	0	sin	0.2×10^5	1.25	0

Variable	$f_{\phi_{xy}}$	ϕ_{xy}	$a_{\phi_{xy}}$
$\rho\ \left(kg/m^3\right)$	cos	0.08	1.25
$u\ (m/s)$	cos	7	0.6
$v\ (m/s)$	cos	-11	0.9
$p\ \left(N/m^2\right)$	sin	-0.25×10^5	0.75

Table 6.5: Manufactured solution coefficients for 2-D subsonic Navier-Stokes cases

Variable	ϕ_0	f_{ϕ_x}	ϕ_x	a_{ϕ_x}	c_x	f_{ϕ_y}	ϕ_y	a_{ϕ_y}	c_y	$f_{\phi_{xy}}$	ϕ_{xy}	$a_{\phi_{xy}}$
$w\ \left(kg/m^3\right)$	80	sin	10	$\frac{1}{3}$	0	sin	2	1.5	0	sin	8	0.4

Variable	f_{ϕ_z}	ϕ_z	a_{ϕ_z}	c_z	$f_{\phi_{xz}}$	ϕ_{xz}	a_{xz}	$f_{\phi_{yz}}$	ϕ_{yz}	a_{yz}
$\rho\ \left(kg/m^3\right)$	sin	-0.12	1.5	0	sin	0.09	1.5	cos	0.09	1
$u\ (m/s)$	cos	-1.8	0.5	0	sin	6	0.8	sin	6	0.4
$v\ (m/s)$	sin	-3	1.25	0	cos	12	0.7	sin	12	0.8
$w\ (m/s)$	cos	3.5	1	0	sin	-8	0.6	cos	-8	0.8
$p\ \left(N/m^2\right)$	cos	-0.35×10^5	$\frac{1}{3}$	0	cos	0.3×10^5	1	cos	0.3×10^5	0.5

Table 6.6: Additional Manufactured solution coefficients for 3-D subsonic Navier-Stokes cases

Variable	ϕ_0	f_{ϕ_x}	ϕ_x	a_{ϕ_x}	c_x	f_{ϕ_y}	ϕ_y	a_{ϕ_y}	c_y
$\rho\ \left(kg/m^3\right)$	1	sin	0.1	0.75	0	cos	0.15	1	0
$u\ (m/s)$	800	sin	50	$\frac{5}{3}$	0	cos	-30	1.5	0
$v\ (m/s)$	800	cos	-75	1.5	0	sin	40	1	0
$p\ \left(N/m^2\right)$	1×10^5	cos	-0.3×10^5	1	0	sin	0.2×10^5	1.25	0

Variable	$f_{\phi_{xy}}$	ϕ_{xy}	$a_{\phi_{xy}}$
$\rho\ \left(kg/m^3\right)$	cos	0.08	1.25
$u\ (m/s)$	cos	70	0.6
$v\ (m/s)$	cos	-110	0.9
$p\ \left(N/m^2\right)$	sin	-0.25×10^5	0.75

Table 6.7: Manufactured solution coefficients for 2-D supersonic Navier-Stokes cases

Variable	ϕ_0	f_{ϕ_x}	ϕ_x	a_{ϕ_x}	c_x	f_{ϕ_y}	ϕ_y	a_{ϕ_y}	c_y	$f_{\phi_{xy}}$	ϕ_{xy}	$a_{\phi_{xy}}$
$w\ (kg/m^3)$	800	sin	15	$\frac{1}{3}$	0	sin	-25	1.5	0	sin	80	0.4

Variable	f_{ϕ_z}	ϕ_z	a_{ϕ_z}	c_z	$f_{\phi_{xz}}$	ϕ_{xz}	a_{xz}	$f_{\phi_{yz}}$	ϕ_{yz}	a_{yz}
$\rho\ (kg/m^3)$	sin	-0.12	1.5	0	sin	0.09	1.5	cos	0.09	1
$u\ (m/s)$	cos	-18	0.5	0	sin	60	0.8	sin	60	0.4
$v\ (m/s)$	sin	-30	1.25	0	cos	120	0.7	sin	120	0.8
$w\ (m/s)$	cos	35	1	0	sin	-80	0.6	cos	-80	0.8
$p\ (N/m^2)$	cos	-0.35×10^5	$\frac{1}{3}$	0	cos	0.3×10^5	1	cos	0.3×10^5	0.5

Table 6.8: Additional Manufactured solution coefficients for 3-D supersonic Navier-Stokes cases
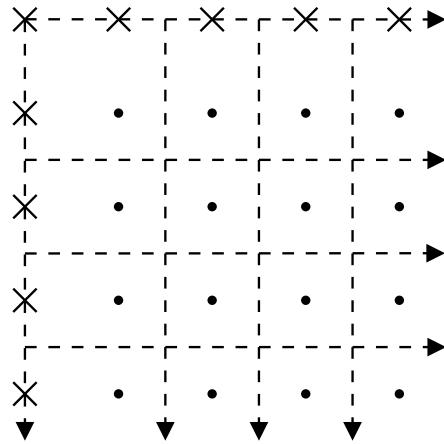
Figure 6.1: Grid nodes and control volumes on a uniform nodal mesh
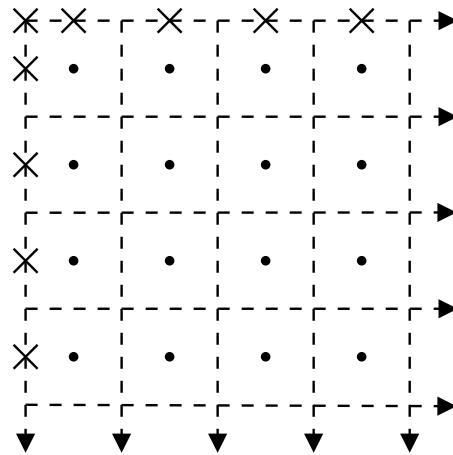
Figure 6.2: Grid nodes and control volumes on a nodal mesh modified to achieve uniform control volumes

Figure 6.3: Discretization error L_2 norms in the 2-D supersonic Euler case with varying grid resolution
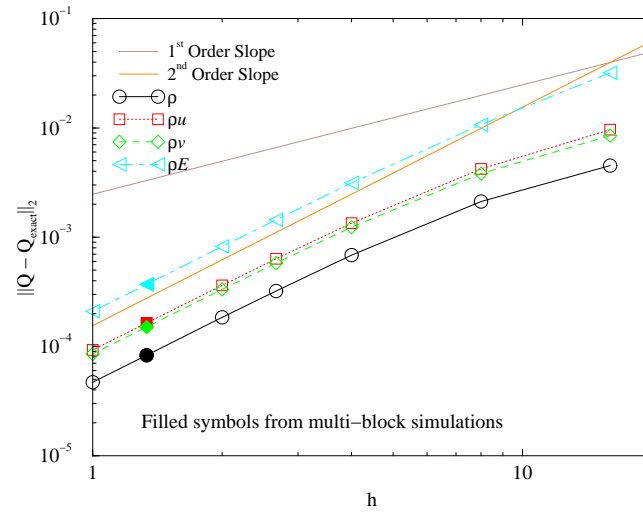
Figure 6.4: Discretization error L_2 norm in the 2-D supersonic Euler case with no TVD limiter for varying grid resolution

77
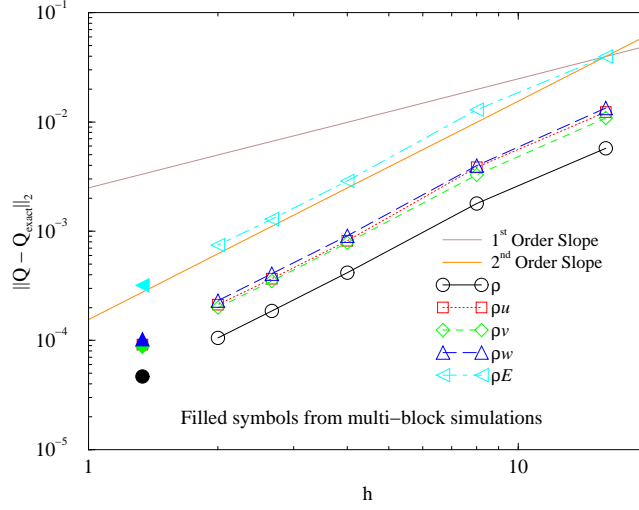
Figure 6.5: Discretization error L_2 norms in the 3-D supersonic Euler case with varying grid resolution
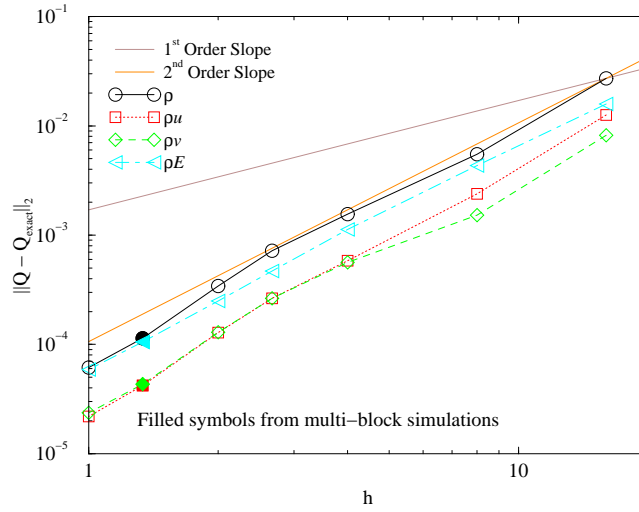
Figure 6.6: Discretization error L_2 norm in the 2-D subsonic Euler case with varying grid resolution

78
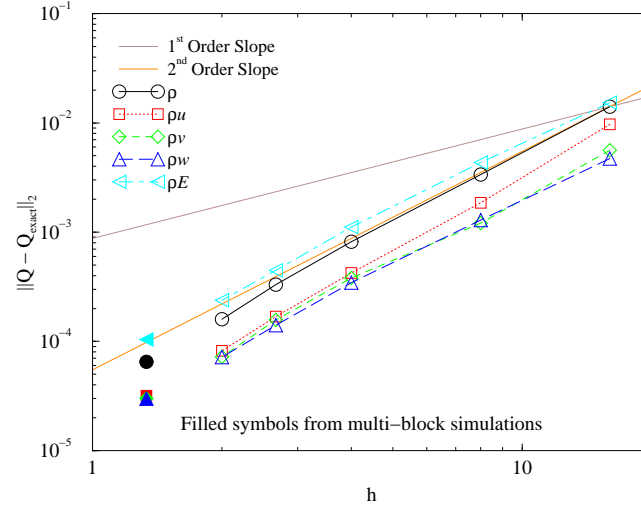
Figure 6.7: Discretization error L_2norm in the 3-D subsonic Euler case with varying grid resolution
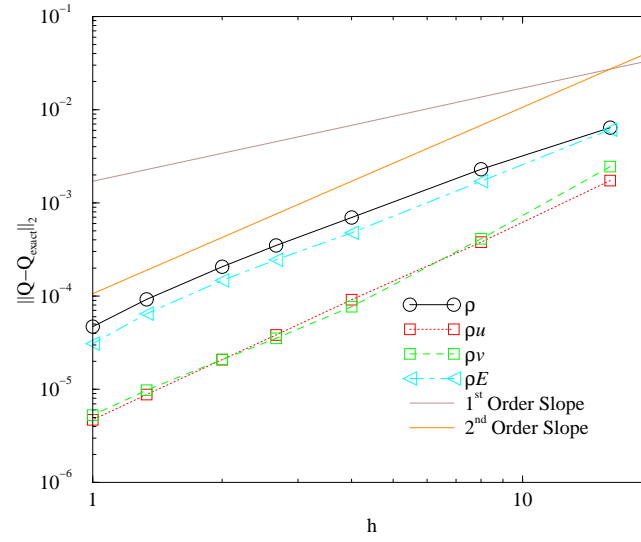
Figure 6.8: Discretization error L_2norm in the 2-D subsonic Navier-Stokes case with varying grid resolution
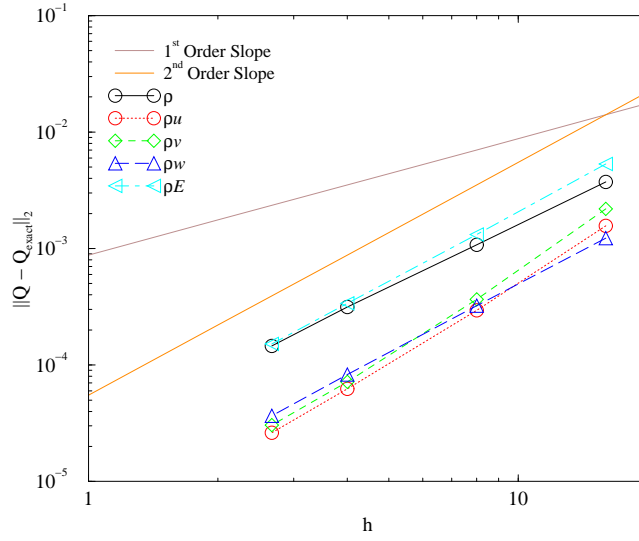
Figure 6.9: Discretization error L_2norm in the 3-D subsonic Navier-Stokes case with varying grid resolution
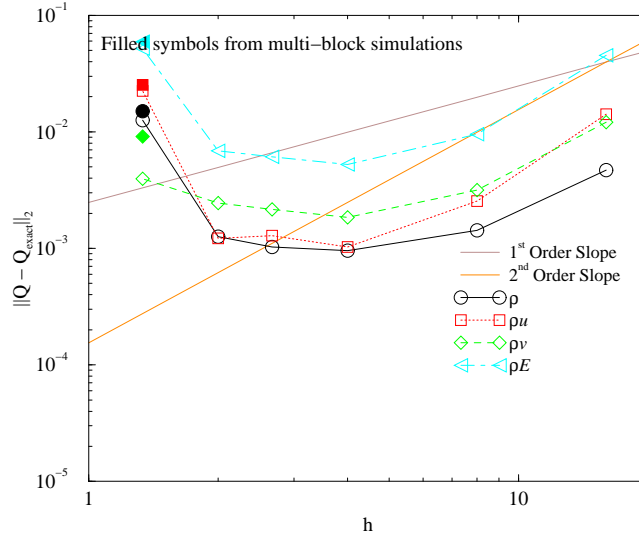
Figure 6.10: Discretization error L_2norm in the 2-D supersonic Navier-Stokes case using original "first order" extrapolation at outflow boundaries with varying grid resolution
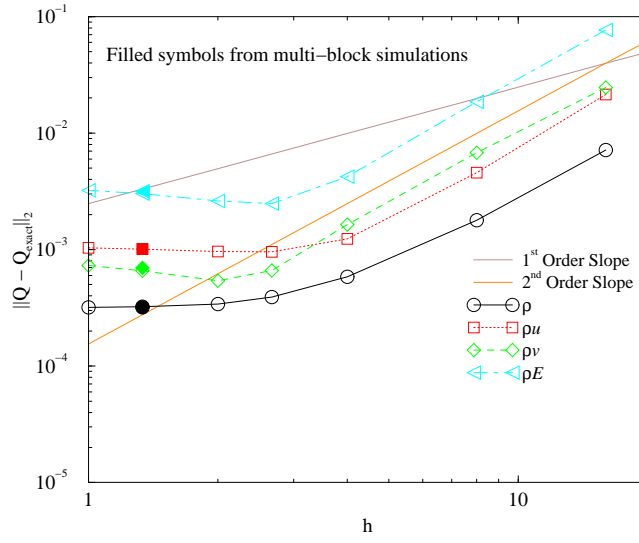
Figure 6.11: Discretization error L_2norm in the 2-D supersonic Navier-Stokes case using zero[th] order extrapolation at outflow boundaries with varying grid resolution
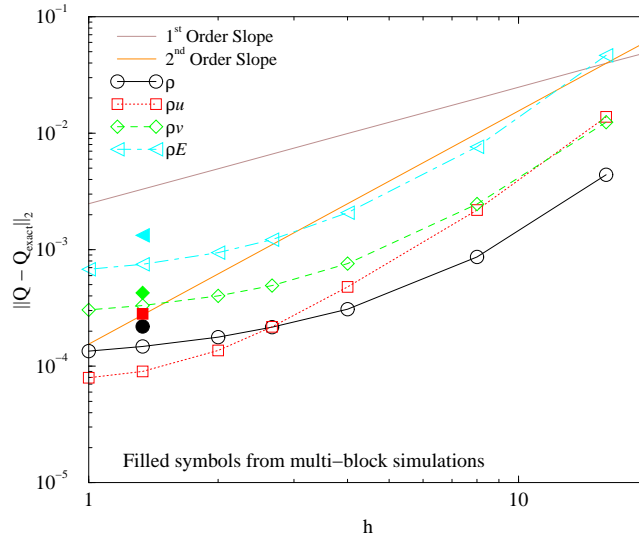
Figure 6.12: Discretization error L_2norm in the 2-D supersonic Navier-Stokes case using corrected first order extrapolation at outflow boundaries with varying grid resolution
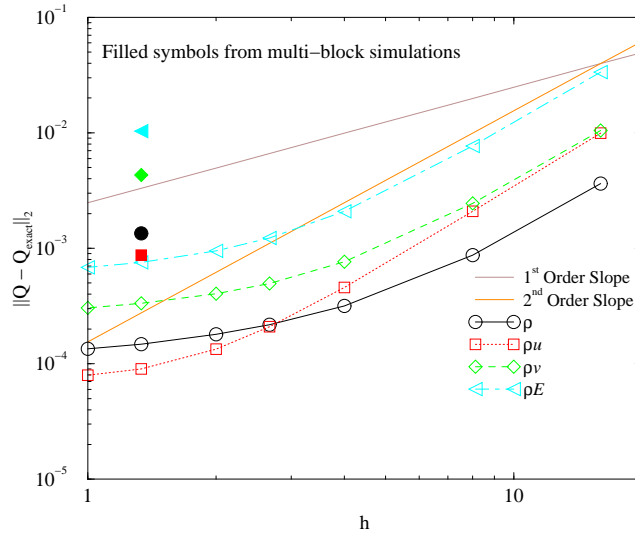
Figure 6.13: Discretization error L_2norm in the 2-D supersonic Navier-Stokes case using corrected first order extrapolation at outflow boundaries and no TVD limiter with varying grid resolution
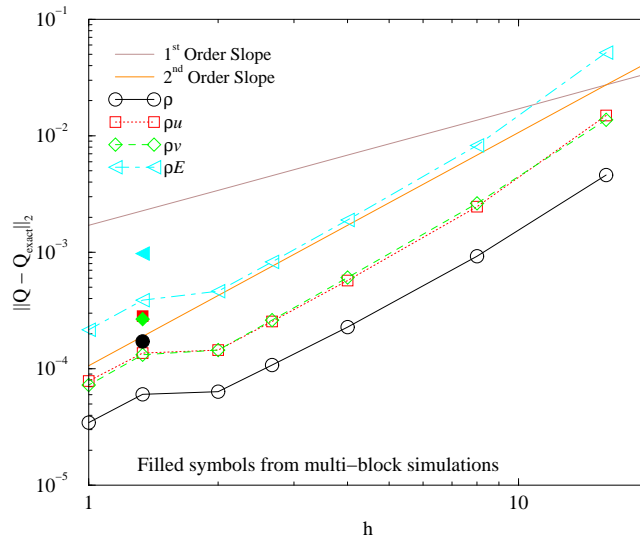
Figure 6.14: Discretization error L_2norm in the 2-D supersonic Navier-Stokes case using frozen outflow boundaries with varying grid resolution
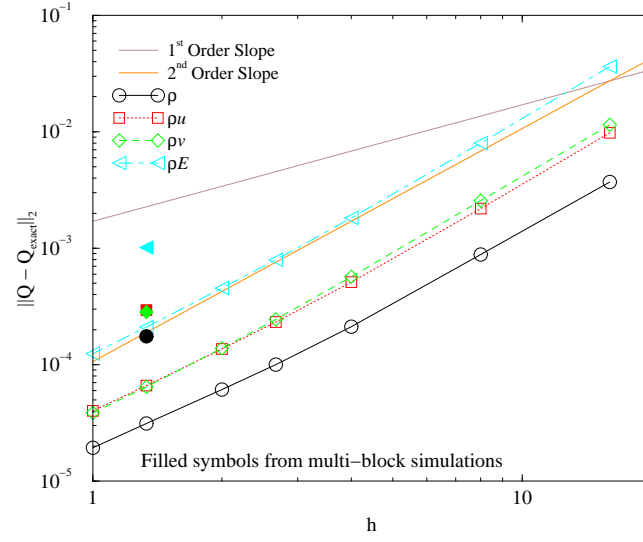
Figure 6.15: Discretization error L_2norm in the 2-D supersonic Navier-Stokes case using frozen outflow boundaries and the Koren limiter with varying grid resolution

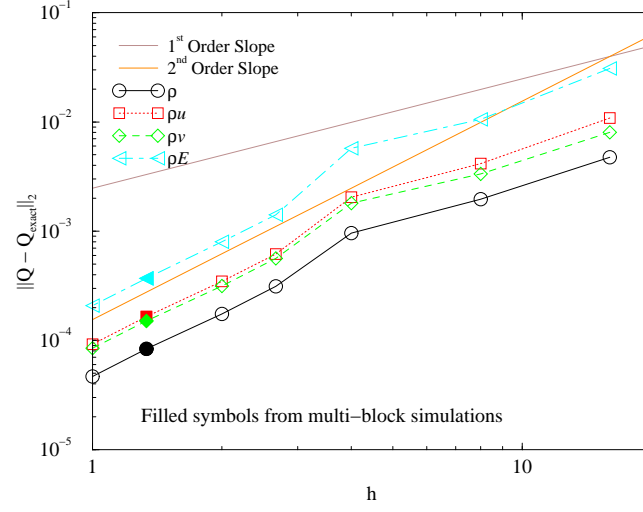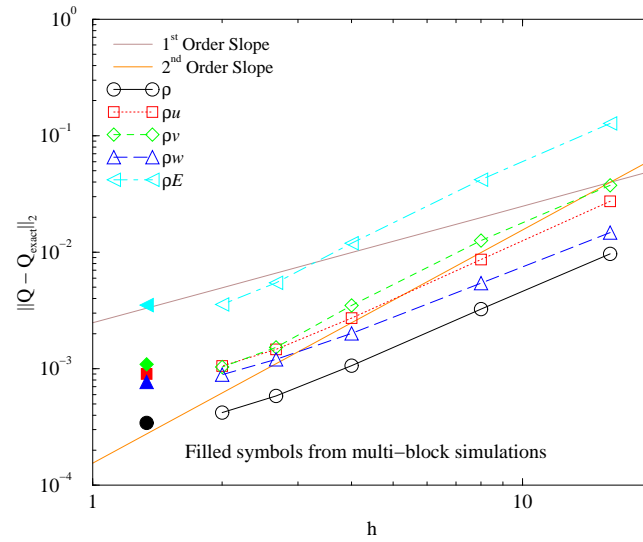Figure 6.16: Discretization error L_2norm in the 3-D supersonic Navier-Stokes case with varying grid resolution
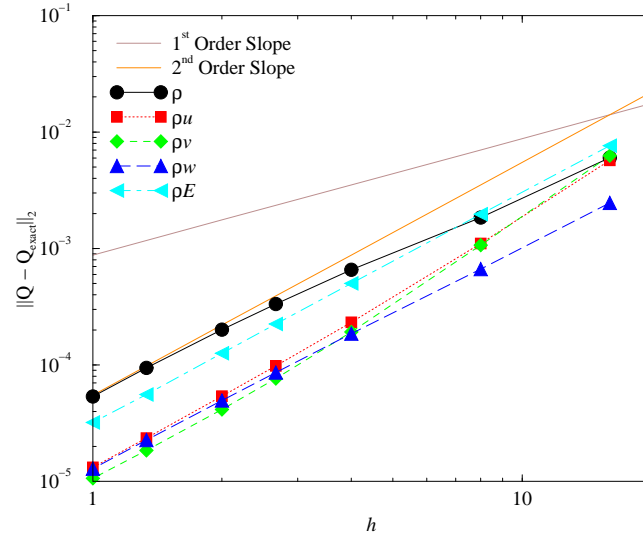
Figure 6.17: Discretization error L_2norm with varying grid resolution for the 3-D subsonic Navier-Stokes case using multi-block grids with double-fringe overlapping boundaries
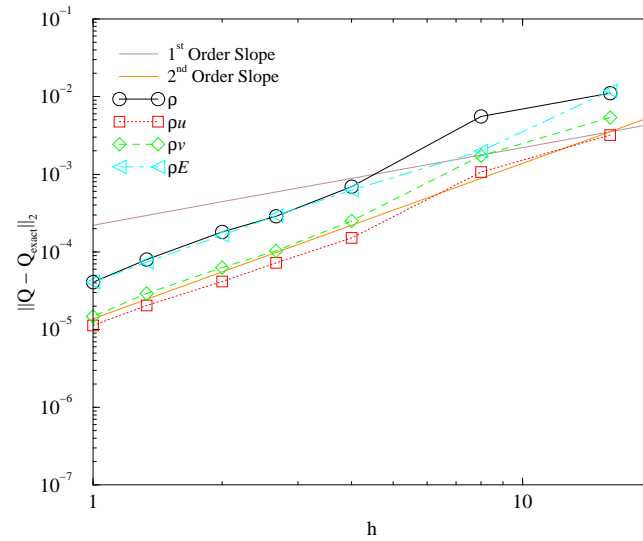
Figure 6.18: Discretization error L_2norm with varying grid resolution for the 2-D subsonic Euler case using a third order scheme

84
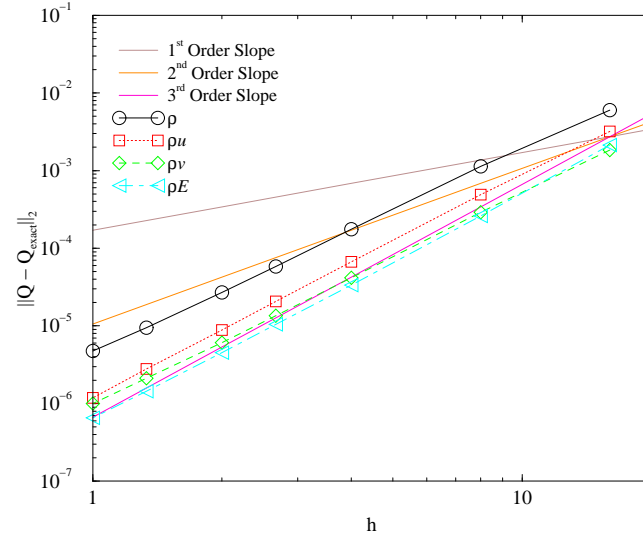
Figure 6.19: Discretization error L_2norm with varying grid resolution for the 2-D subsonic Euler case using a third order scheme with no limiter
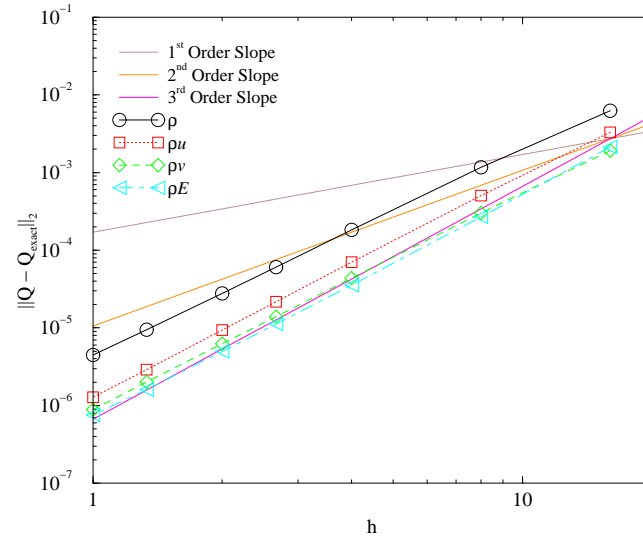
Figure 6.20: Discretization error L_2norm with varying grid resolution for the 2-D subsonic Euler case using a third order scheme with the Koren limiter
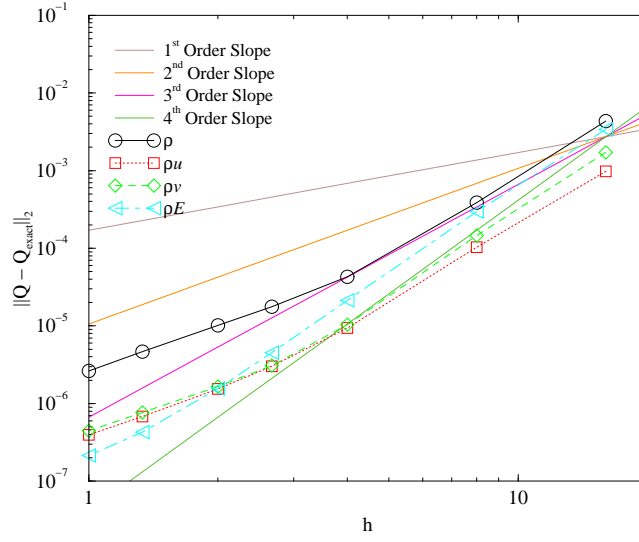
Figure 6.21: Discretization error L_2norm with varying grid resolution for the 2-D subsonic Euler case using a fourth order scheme
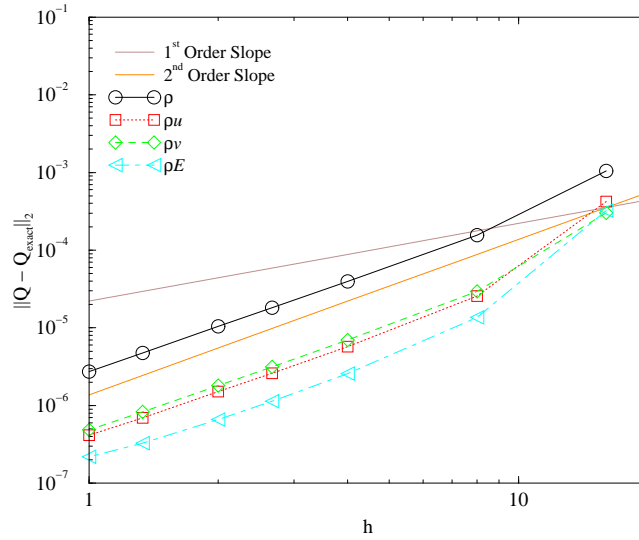
Figure 6.22: Discretization error L_2norm with varying grid resolution for the 2-D subsonic Euler case using a fifth order scheme
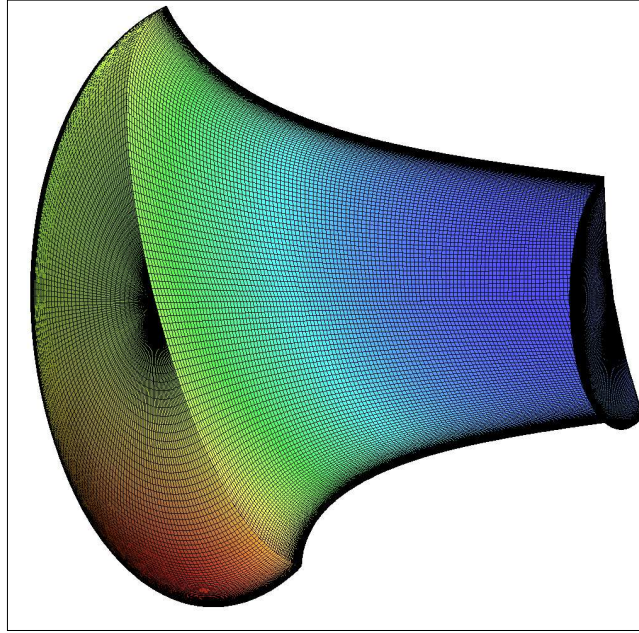
Figure 6.23: Grid with density contours for the subsonic Euler test case on a 3-D curvilinear grid
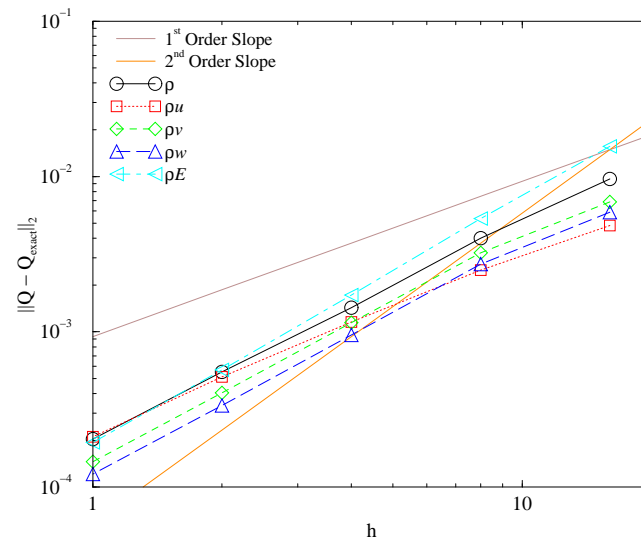
Figure 6.24: Discretization error L_2 norm with varying grid resolution for the 3-D subsonic Euler case using a curvilinear grid

Chapter 7

Significant Code Infrastructure Improvements

As stated above, the ultimate objective of this project is to obtain an improved capability to perform time accurate simulations of large ground test facilities. Because of the geometric complexity and large size of these facilities, this requirement can only be met with a full-featured production CFD solver with "higher" resolution features added to allow the transport of the unsteady features of interest over the required distance. Because of this, single-purpose research codes, while useful as a technology testbed, were not sufficient. Therefore, transfer of any new technology to a "production" CFD tool was essential for the success of the project. Much effort was invested into building up the capability of a production solver in order to pave the way for the desired large-scale unsteady wind tunnel simulations. As mentioned above, the Wind-US code was used for this work.

7.1 Second Order Implicit Time Marching

One of the factors which has limited Wind-US's applicability in the realm of unsteady flows has been the implicit time marching procedure. The default algorithm, which came from NASTD, was a first order backward Euler scheme. This scheme is unsuited to time accurate simulations, and, indeed, it was never intended that it be used in such a fashion. In NASTD, unsteady simulations always used one of the available Runge-Kutta explicit time marching procedures. For the current project, however, the ability to run time-accurate simulations of complex geometries with very large time steps is required, and this necessitates an implicit algorithm.

To illustrate the problems with the original implicit time marching algorithm in Wind, a simple inviscid vortex convection case has been run. This case was obtained from the suite of test cases that are distributed with the OVERFLOW solver[40]. A vortex in a uniform mean flow is simulated on a uniform 80x80 Cartesian grid (not including boundary points) covering 10 ft on each side. The boundary conditions are periodic so that as the vortex is swept out the back of the domain, it reappears at the

inflow. The freestream Mach number was 0.5, the total temperature was 525°R, and the total pressure was 0.937 psi. A non-dimensional time step of 0.1 was used, which translates to a dimensional step of 9.124×10^{-5} seconds and 200 time steps per flow-through time. The default second order Roe spatial scheme and ADI matrix inversion algorithms were employed.

Fig. 7.1 shows density contours for both the initial conditions and after five flow-through times. From the figure, it is obvious that the default scheme is inappropriate for unsteady time marching. By the end of five flow-through times, significant dissipation and dispersion errors are present.

As a first step toward improving the unsteady implicit capability, a Newton iteration procedure was added relatively early on in the process of developing Wind. This improved the time marching ability, but persistent problems were present in the implementation which have only recently been resolved (for Wind-US). Fig. 7.2 shows the results for the same test case using Newton iterations in conjunction with the first order time marching algorithm. For this case, five sub-iterations were used at each time level. The addition of Newton iterations reduces the dispersion error considerably, but the dissipation in the scheme is still unacceptably large.

A second order implicit time marching algorithm has now been implemented in the Wind-US code. This technique is applicable either with or without Newton iterations. At present, all of the implicit schemes in Wind, except for the MacCormack implicit scheme, can be used with this second order capability. Figure 7.3 shows results for the same case using the second order scheme without any Newton iterations. As the figure clearly shows, the dissipation is greatly reduced, but the dispersion error is still unacceptably large.

Finally, a run was performed using the second order algorithm with Newton iterations. Again, five sub-iterations were used at each time level. Figure 7.4 shows the resulting density contours. In this case, not only has the dissipation been dramatically reduced by the second order scheme, compared to the first order algorithm, but the Newton iteration procedure has dramatically reduced the dispersion error. This result, while still being more dissipative than the high resolution schemes typically used for the most demanding unsteady simulations, is clearly a significant improvement over the original algorithm in Wind-US. Note that the spatial differencing used for these tests was the default second order scheme. Wind-US has the ability to run schemes of up to a nominal fifth order in space.

7.2 Improved In o w Boundary Conditions

In an interior flow case, it is often convenient to specify total conditions at an inflow boundary. In the course of FY2003, a user of the Wind code reported problems in using the "hold totals" inflow boundary condition. As a result of this problem, the inflow condition was rewritten in a greatly improved form that is both more stable and more accurate than the previous version. While this project did not pay for that work, it does stand to benefit from it, and thus a brief overview is presented.

The idea of both the old and the new boundary conditions is the same. The user specifies a total temperature, total pressure and flow angle at the boundary (which can

vary from point to point). These quantities are held fixed while the R_2 Riemann invariant ($u_\perp - \frac{2c}{\gamma-1}$) is extrapolated from the interior. The previous implementation, however, used a Newton iteration to simultaneously solve for the temperature and velocity at the boundary point. This iterative procedure would at times not converge, resulting in instability in the overall solution. The new implementation first solves a quadratic equation for the speed of sound based on substituting the normal velocity between the T_0 and R_2 equations. This yields the temperature, and the velocity can then be found from the definition of R_2.

The new approach is generally the same as that taken in the OVERFLOW code[40]. In Wind-US, however, the Riemann invariant is extrapolated using a first order algorithm, rather than the more usual zeroth order. This seemingly simple change makes a noticeable improvement in the total pressure distribution interior to the boundary, as shown in Fig. 7.5 for a representative duct case. It is especially telling that one cannot even obtain a converged answer at all using the old boundary conditions unless one sets up the flow with some other inflow boundary treatment, whereas the new conditions are stable enough to be used from the start. As is typical of characteristic-based boundary conditions, there are fluctuations in the total conditions immediately downstream of the boundary. With the new implementation, however, the values eventually return to the freestream conditions, whereas with the previous boundary conditions (and indeed the new implementation as well, unless a first order extrapolation of the invariant is used) the flow never returns to the freestream conditions. This is illustrated in Fig. 7.6, which shows the normalized total pressure along the center line.

7.3 Compressible version of SST turbulence model

Although the majority of the flowfield in the 16-S tunnel test case is nearly incompressible, it is anticipated that, at least in some cases of facility unsteadiness, the effects of compressibility could become important. To address this concern, a density weighted version of the SST model was written to complement the original model, which used an incompressible formulation. This version is implemented in conservative form and includes the compressibility corrections of Suzen and Hoffmann[41]. In addition to the current application, these terms are expected to be especially helpful in the simulation of free shear layers at transonic speeds (and higher) and other flows where the effects of compressibility are expected to be significant. The compressibility corrections include a pressure dilatation model and a turbulent Mach number based model of compressible dissipation.

To demonstrate the effect of the various changes to the SST model, a simple axisymmetric jet case was performed. This case involves a "submerged" turbulent supersonic jet emanating from an axi-symmetric convergent-divergent Mach 2.2 nozzle. This nozzle was first studied by J. M. Eggers in 1962[42]. The working fluid was air, and the nozzle was operated at the pressure ratio corresponding to perfect expansion. The nozzle plenum conditions were set to a total temperature of $525°R$ and the total pressure was 162.2psia. The ambient temperature was $252°R$ and the ambient pressure was 14.7psia.

The simulated centerline axial velocity is plotted in Fig. 7.7 for four different cases

as well as the experimental data of Eggers. The first two curves on the plot (designated SST1 and SST2 on the legend) lie directly on top of each other. They are for the original version of the SST model and the new conservative version with no compressibility corrections added. As expected, they are overly dissipative of the velocity downstream of the potential core. The curve designated "SST2-CD" shows the effect of the compressible dissipation correction, while the curve labeled "SST2-CD-PD" shows the same case with pressure dilatation and compressible dissipation added in. With the addition of the compressibility corrections, the velocity decay is much better predicted aft of the potential core, but the length of the potential core is increasingly over-predicted. This is in line with the observations of other researchers.[43] Thus, this capability, while helpful in some cases, must be used with caution.

7.4   Unsteady Pseudo-Turbulent In o w BC

Real ground test facilities do not have perfectly uniform flow. The effect of unsteady inflow conditions is potentially significant. For instance, Soteriou and Ghoniem [44] show the development of an incompressible spatial mixing layer with and without perturbation at the inflow boundary. Compared to the perturbed case, the development of the mixing layer without perturbation is delayed significantly while the Kelvin-Helmholtz instability, activated by minute numerical errors, builds until the layer finally rolls up.

Researchers have taken several approaches to this problem. Sometimes, as in Soteriou and Ghoniem's unperturbed case, nothing is done to emulate turbulence at the inflow. For those who wish to account for inflow turbulence, perhaps the simplest approach is to add random "white noise" to the mean flow profiles at the inflow boundary. Comte *et al.* [45] did this for a plane mixing layer and again [46] for a plane wake. This approach has significant drawbacks, however, because this incoming "turbulence" has no correlation in space or time, which is unphysical.

Another approach is to perturb the velocity at one or more discrete frequencies. These frequencies are usually based on the most unstable frequency (and its subharmonics) as predicted by linear stability analysis. Examples of this approach, in addition to the previously mentioned incompressible work by Soteriou and Ghoniem[44], are compressible mixing layer computations by Sekar and Mukunda [47] and Lele [48]. This approach is quite effective, especially if one specifically desires to simulate a genuinely forced flow, such as in the experimental work by LeBoeuf [49]. The capability to do this already exists in the Wind-US code. Real turbulence, however, does not generally confine itself to a few discrete frequencies; therefore, if a more realistic inflow is desired, something more sophisticated must be done.

Another technique for introducing turbulent fluctuations at an inflow boundary is to use a separate temporal LES or DNS, running in parallel to the spatial case, to generate the inflow turbulence [50]. Where it is possible to use such an approach, it would seem to be an ideal solution. Unfortunately, it is computationally very expensive. A variation of this technique is sometimes used in channel flows in which the turbulence from a given point downstream (where the flow is assumed to be fully turbulent) is rescaled and introduced at the inflow boundary. This method can be quite successful, but is

limited in its application to cases where some form of scale similarity law can be used. It would be very difficult, if not impossible to apply such a rescaling method to a fully general case.

A final method (or family of methods) for adding turbulence at the inflow boundary attempts to emulate the full spectrum of turbulence up to the resolution of the grid. In this method, measured or approximated turbulent intensities at the inflow are combined with information on the turbulence energy spectrum (usually an assumed functional form) to derive time varying velocity perturbations. Such an approach has been used by Oh and Loth [51] for supersonic shear layers; Schwer, Tsuei, and Merkle [52] for low speed reacting mixing layers; and Lee, Lele, and Moin [53] for spatially developing isotropic turbulence. More recently, Batten, Goldberg, and Chakravarthy [54] have developed a related technique and applied it to a variety of problems.

The present work will use a variation of the method of Lee, Lele, and Moin. The current implementation is designed to be relatively general, but comparatively inexpensive. The drawback is that it lacks the sophistication of the more complex methods (such as Batten's or recent work by Keating and Piomelli[55]). The current method is best applied to flows where there is a strong initiator of turbulent growth within the flowfield itself, such that, while the incoming turbulent fluctuations may be an important trigger, the fine details of the incoming turbulence are not critical. An example of such a case is the aforementioned Samimy and Elliott mixing layer, where the presence of three dimensionality in the flow as it passes the end of the splitter plate appears sufficient to allow the development of a turbulent mixing layer.

Conceptually, the present approach to inflow turbulence may be described as computing a "box" of frozen turbulence which is convected by the mean flow into the computational domain (see figure 7.8).The first step in this process is to calculate a pseudo-random divergence-free isotropic velocity field which conforms to a prescribed energy spectrum. This field is computed initially in a cubic domain that large enough to encompass the inflow boundary and is assumed periodic in all directions. It is computed on a uniform Cartesian grid (the default is 32^3, but can be specified in the input file). Given the assumed energy spectrum, which is discussed below, and a sufficiently low peak wavenumber (based on box size), this level of resolution is sufficient to capture the majority of the energy-containing wavenumbers, but it does mean that in regions where grid points are highly concentrated, the computational domain is able to resolve much higher wavenumbers than are calculated in the inflow turbulence.

The method for computing this solenoidal isotropic field is as follows. One first computes a stream function energy distribution in spectral space:

$$E_\Psi\left(\vec{k}\right) = \frac{E\left(\vec{k}\right)}{\left|\vec{k}\right|^2} \tag{7.1}$$

In the above equation, $E(\vec{k})$ is the desired energy distribution of the velocity field. The use of the above expression results in a velocity field that approximately matches the desired spectrum. It is assumed that the turbulent energy is distributed evenly throughout each wavenumber shell. Thus $E(\vec{k})$ can be expressed as a function of the magnitude of the wavenumber vector ($k \equiv \left|\vec{k}\right|$). The assumed form of the energy spectrum is the

92

same as that which has been used previously for similar purposes by, among others, Lee, Lele, and Moin [56] [53]:

$$E(k) = k^4 \exp\left(-2\left(\frac{k}{k_p}\right)^2\right) \tag{7.2}$$

For convenience, the spectrum is normalized such that:

$$\int_0^\infty E_{norm}(k)\, dk \equiv 1 \tag{7.3}$$

Thus, for the functional form given in equation 7.2 above,

$$E_{norm}(k) = \frac{k^4 \exp\left(-2\left(\frac{k}{k_p}\right)^2\right)}{\frac{3}{64}\sqrt{2\pi}k_p^5} \tag{7.4}$$

The non-dimensional wavenumber at which this function reaches its peak, k_p, can be specified by the user either directly or as a dimensional value (per foot).

Next, the phase angles are chosen randomly (between $-\pi$ and π). Using this information, a stream function, $\hat{\Psi}_i\left(\vec{k}\right)$, may be computed in spectral space. Using a Fourier transform, this leads to a physical stream function, $\Psi_i(\vec{x})$, from which velocities can be computed.

$$u \equiv \frac{\partial \Psi_z}{\partial y} - \frac{\partial \Psi_y}{\partial z} \tag{7.5}$$

$$v \equiv \frac{\partial \Psi_x}{\partial z} - \frac{\partial \Psi_z}{\partial x} \tag{7.6}$$

$$w \equiv \frac{\partial \Psi_y}{\partial x} - \frac{\partial \Psi_x}{\partial y} \tag{7.7}$$

If the field is to be absolutely divergence free, it is necessary to perform this calculation using the same algorithm for taking derivatives as the Navier-Stokes solver will use. The velocity field thus calculated will be truly divergence-free only with respect to the derivative algorithm that was used to compute it. For example, a field that is divergence-free with respect to spectral derivatives is not solenoidal with respect to a fourth-order central difference derivative algorithm or any other non-spectral derivative scheme. In the current work, a fourth order central difference scheme is used for the derivatives. Since the code solves the compressible Navier-Stokes equations, the solenoidal component introduced by the turbulent inflow due to the use of a different numerical scheme on the interior should not cause problems.

Because the energy spectrum of the stream function was only approximate (for non-spectral derivatives), the velocity field must be re-scaled in order for its energy spectrum to match the target spectrum exactly. This is done by converting the physical velocity field back into spectral space, where its energy spectrum is calculated. The

spectral velocity field is then scaled so that the energy in each wavenumber shell will match the value predicted by the desired energy spectrum. The scaled field is then transformed back into physical space. As long as the derivative algorithm that is used is either spectral or a uniform operator in space (in this instance, a fourth-order central difference scheme), the scaled field will retain the solenoidal properties of the original.

In order to make use of the pseudo-turbulent velocity field thus created, it is assumed that the turbulence is convected into the domain at a constant mean velocity. This allows one to interpolate the velocity fluctuations from the uniform grid on which they were generated onto the actual inflow plane. This field, however, does not take into account the experimentally determined distribution of turbulent intensity, nor does it take into account the variation of resolved and unresolved turbulence due to differences in grid cell sizes.

Since the energy spectrum is known at the inflow plane, it is relatively simple to compute the fraction of energy that is resolved at a given grid location (from the mesh size) and modify the velocity perturbations accordingly. Also, if walls are present, the user can specify a desired boundary layer height, and the velocity fluctuations are scaled to roughly account for their presence.

For supersonic inflow, perturbations can be directly added to mean flow. For subsonic flow, a less direct method of injecting the perturbations must be used. First, components of velocity tangential to the boundary are directly specified. The normal perturbations, however, are introduced indirectly by modifying the local total temperature and total pressure, and using a characteristics-based boundary condition to compute the normal velocity and the thermodynamic variables.

In order to prevent the introduction of spurious periodicity to the solution, the random phase angles are updated at irregular intervals and the velocity field is recomputed. Changing all of the phase angles simultaneously would result in a pseudo-turbulent field which had no correlation to the one used just the previous iteration. Therefore, only the phase angles associated with one wavenumber shell are modified at any given time. Thus, at any given point where the phase angles are being modified, the changes are relatively small, with a strong correlation to the previous field. The changes are spaced in such a way, however, that in a given flow-through time of the pseudo-turbulent box, all of the wavenumber shells are thus "scrambled" at least once, resulting in a completely new realization.

Figure 7.9 gives some indication of the sort of unsteady field which results from the application of this boundary condition. Contours of the tangential (v) component of velocity are shown for supersonic and subsonic 2-D jet flows. The jet enters the domain on the left side, and covers the middle fifty percent of the boundary. The supersonic jet has a mean core Mach number of 1.209 compared to the surrounding air, which is moving at Mach number 1.009. The subsonic jet case has the freestream moving at $M = 0.7$ and the mean velocity of the jet at $M = 0.9$. While this case does not properly resolve the shear layers at the edge of the jet, it clearly shows the effect of the unsteady inflow, as well as the code's ability to carry that unsteady flow downstream.

7.5   Other Fixes and Enhancements

Additional fixes and improvements to the Wind-US code have been made during the course of this work. Although many, if not most, of them were not paid for by AFOSR, the Facility Unsteadiness Research project benefits from the improved computational capability. Some of the more relevant fixes are now noted in brief.

Wind-US (and Wind before it) had, at least nominally, simple steady-state screen models. Unfortunately, the implementation of these models had serious bugs that prevented them from functioning properly. These problems have now been fixed and the model appears to work as advertised. This provides an important starting point for any, more advanced, models which may be developed in future.

Persistent, but intermittent, problems have been encountered in the Wind code for quite some time in certain areas that were critical to the successful execution of this project. Specifically, the Newton iteration and block-to-block coupling algorithms had numerous problems related to memory addressing, parallel processing, and unanticipated special case situations. At irregular intervals, these would cause the code to fail without warning (and often without any error message at all). Thanks to a significant rewrite which allows Wind, and now Wind-US, to be run with very restrictive error checking under a debugger, these algorithms have been stabilized (and many other problems fixed as well).

For some time, there has been a desire for the capability to run Wind-US with double precision variables. A variety of applications, including the Facility Unsteadiness Research project, were seen as possible beneficiaries of such a capability, but the work involved in rewriting the code was seen as too great, and the task was never undertaken until recently, when an overall rewrite of the memory allocation to use FORTRAN 90/95 constructs was performed (mostly by Boeing). At that time, a capability was introduced to specify the precision of the variables at compile time. Although this capability is fully functional, work is still ongoing to ensure that the precision of the solution is not corrupted by lower precision constants or variables being used inadvertently during the solution process.

One area which has seen an immediate impact of the new capability is the Method of Manufactured Solutions verification process; it is now possible to converge residuals at least a further six orders of magnitude beyond what the single precision code can accomplish. This removes a significant unknown from the MMS process, because, especially for the higher order schemes, the error was often small enough that the precision of the code prevented a fully converged realization of the problem. An example of this is shown in Figure 7.10. The first plot shows the error in the total energy variable after the solution has been converged as much as possible using a single precision code. The second plot is the same case run with the double precision version. With the improved precision, although the overall error levels remain similar, the solution is much smoother, indicating that what is being observed is truly the error in the numerical scheme, rather than the results of precision limitations. Similar benefits are expected to accrue for long unsteady runs, where tens and hundreds of thousands of realizations are to be averaged in order to obtain the desired statistics. Without double precision variables, such calculations are subject to significant error.

Another area of work has been the verification and validation of the various ca-

pabilities implemented in Wind-US. Some of this work is documented elsewhere (in Chapter 6). A related issue that has been a persistent problem for NPARC Alliance developers has been the frequency with which a fix for one bug introduces a problem in another part of the code which heretofore worked. To address this problem, an effort was initiated to begin gathering, organizing, and computing baseline solutions for a set of test cases that would exercise as many features of the code as could be managed. The ultimate goal is to have suites of test cases which would cover the full range of physics, models, and code options available in the code. Along with the cases, scripts were written to automatically traverse a directory tree, run each case that is encountered, and compare with the baseline solution. Currently, cases have been identified which span a significant portion of the structured solver's capabilities. In addition, some unstructured cases have been identified, but the coverage is less complete in this area.

The test cases are divided into several "suites" of problems. The most commonly used one is a set of problems that run relatively quickly (in serial mode). The purpose of this suite is to test the basic mechanics of the code. A second test suite consists of cases which run in parallel in order to ensure that the algorithms still function in that mode. A third suite consists of cases which are much larger, and they test the capability of the code to handle complex file and memory requirements, as well as cases with many options interacting with each other. The above tests generally run only for a few iterations; another suite includes cases which are run to convergence. This ensures that the accuracy of the code results have not been compromised.

Note that, although there is some overlap, these suites are distinct from the "NPARC Alliance CFD Verification and Validation Website" (http://www.grc.nasa.gov/WWW/wind/valid/validation.html). The web site contains many good test cases, along with results. The Validation Website, however, treats each case as an individual exercise; there is no provision made for running groups of cases en masse. The "test suites" are an attempt to remedy that situation.

Other minor fixes and enhancements have focused on improving the ability to collect and process the massive quantities of data that a large scale unsteady simulation will generate. The end result of these enhancements is a code which can now (at last) begin to investigate unsteady flow in large, complex facilities.

7.6   WICS Bay Validation Case

The WICS (Weapons Internal Carriage and Separation) $L/D = 4.5$ weapons bay [31] for $M = 0.95$ and $Re = 2.5 \times 10^6/ft$ has been used as a check case to assist in the validation of many of the aforementioned improvements to Wind-US. This is the same case discussed earlier in Chapter 5, where it was run using the NXAIR code. The wind tunnel data were obtained in the AEDC four-foot transonic wind tunnel. The weapons bay was 18 in. long, 4 in. wide, and 4 in. deep. The computational geometry was a flat plate that extended 15 in. upstream of the bay to match the experiment and 25 in. downstream of the bay. The sides of the computational grid extended 50 in. on either side of the bay centerline. Wall functions were employed for all viscous walls. The wall spacing was chosen as 0.0075 in., which corresponds to a $y+$ of 50 on the upstream

plate. The grid system had 1,132,860 points broken into eight grids. A constant time step of 7.88×10^{-6} seconds was used in the calculation. These cases were run using the second order implicit scheme with Newton iterations discussed above. Results have been obtained for both the DES model and the hybrid turbulence model of Nichols and Nelson. The latter model used the compressible form of the Menter SST turbulence model discussed above, including the compressibility corrections.

The calculation was run for 3,000 steps to remove the initial transients and ensure that the flow was fully developed (displaying significant three-dimensionality). Data was then gathered for at least 8192 time steps (the final 8192 time steps being used for spectral analysis) similar to the practice used when running this case with NXAIR.

Figure 7.11 shows Mach number contours from simulations using the DES and Nichols and Nelson hybrid models (at different times). These results show similar behavior as those reported in Chapter 5 (Figure 5.16). Although the flowfield snapshots are taken from slightly different times in the simulation, they are qualitatively very similar. Similar levels of vorticity are observed in both simulations as well, as shown in Figure 7.12 (for the Z-component). As with the earlier NXAIR runs, the turbulent viscosity of the DES model is noticeably lower than that of the hybrid model (as shown in Figure 7.13). This reflects the fact that, away from walls, the DES model switches to a simple LES mode regardless of flow conditions, whereas the hybrid model attempts to estimate the ratio of resolved to unresolved turbulent kinetic energy at each point and bases the switch to LES mode on that. As a result, the hybrid model is detecting regions away from walls where the turbulent scales are small enough that the grid cannot resolve a substantial fraction of the turbulent kinetic energy. To compensate, the turbulent viscosity is increased. Despite this difference, both models predict remarkably similar flow structures. These similarities are not confined to spatial quantities. The sound pressure level spectra at two different points along the centerline of the cavity wall are plotted in Figure 7.14. Although some of the details differ, the overall levels and trends are virtually identical. Visually comparing these plots with the results of the NXAIR runs presented earlier indicates that both codes are predicting similar structures. The sound pressure level spectrum predicted by Wind-US would appear to have a somewhat larger magnitude than that predicted by NXAIR or observed in the experiment. This may reflect a genuine difference between the two codes, but it could equally well be due to differences in post-processing. Unfortunately, a direct comparison with the results from NXAIR and the experiment was not possible, as the original data was not available to the author.

Thus, once again, all else being equal, both the DES and Nichols and Nelson approaches to hybrid RANS/LES turbulence modeling yield functionally equivalent results. This is despite fairly significant differences in the predicted levels of turbulent viscosity. As before, it appears that for cases such as this, other factors, such as the time marching scheme, may be more important than the particular hybrid model used.
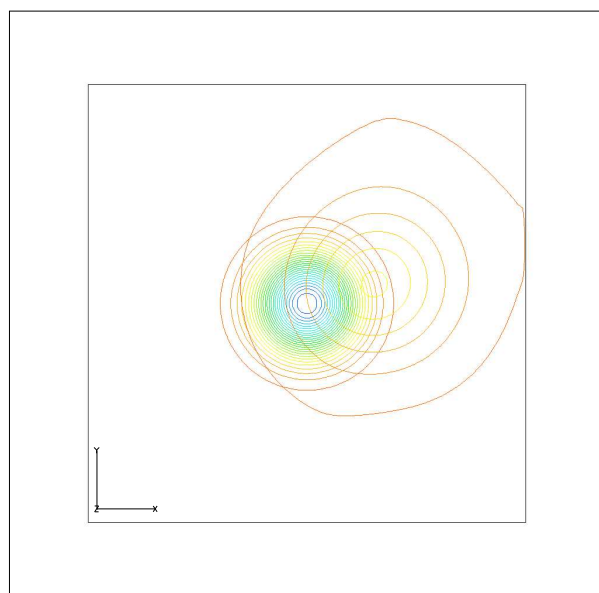
7.12

Figure 7.1: Initial and final density contours from an inviscid vortex convection simulation using first order time marching
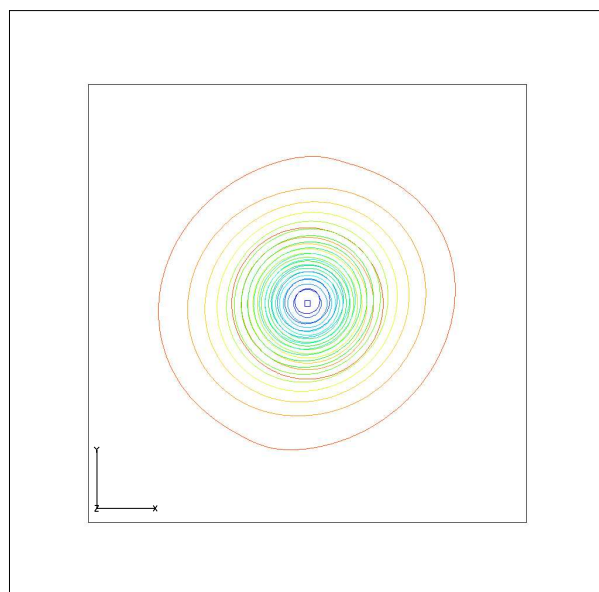

Figure 7.2: Initial and final density contours from an inviscid vortex convection simulation using first order time marching with Newton iteration
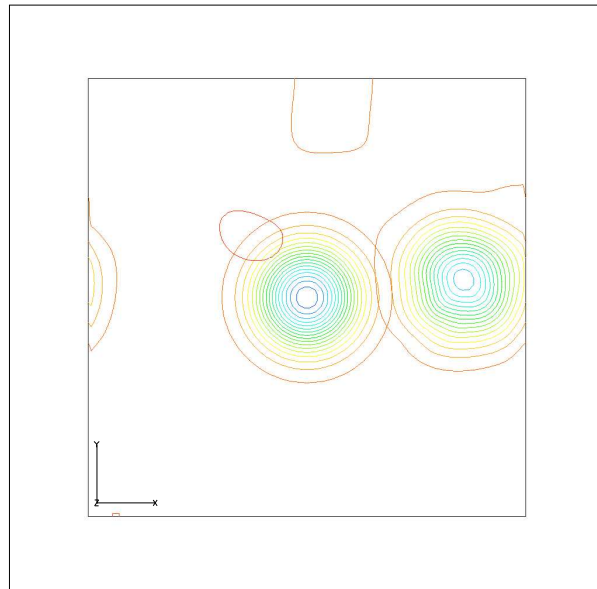
Figure 7.3: Initial and final density contours from an inviscid vortex convection simulation using second order time marching
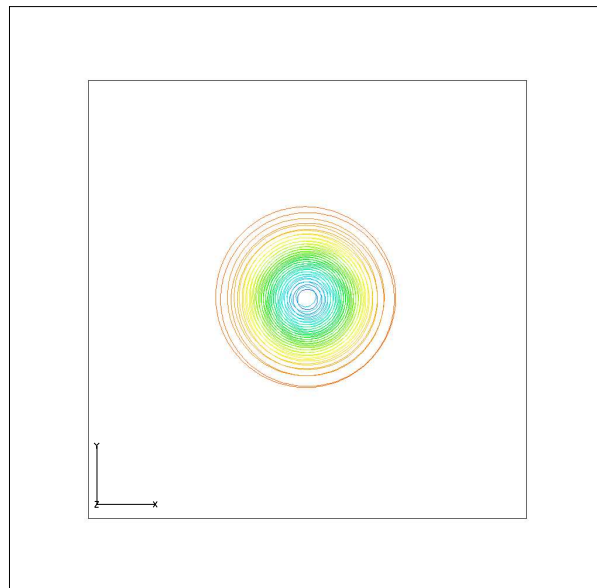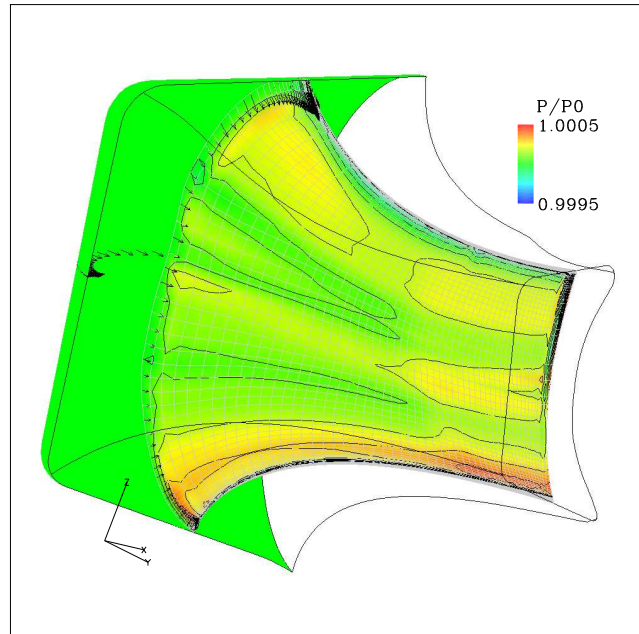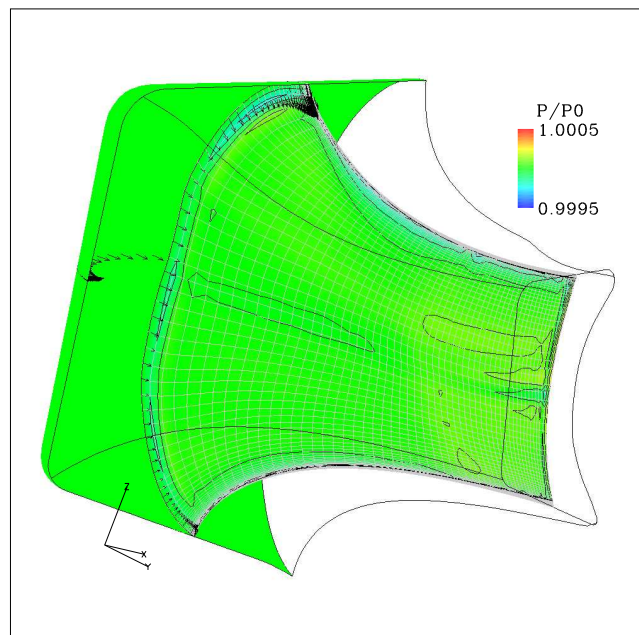

Figure 7.4: Initial and final density contours from an inviscid vortex convection simulation using second order time marching with Newton iterations

(a) Original Wind Infbw Boundary Condition

(b) Improved Wind-US Infbw Boundary Condition

100

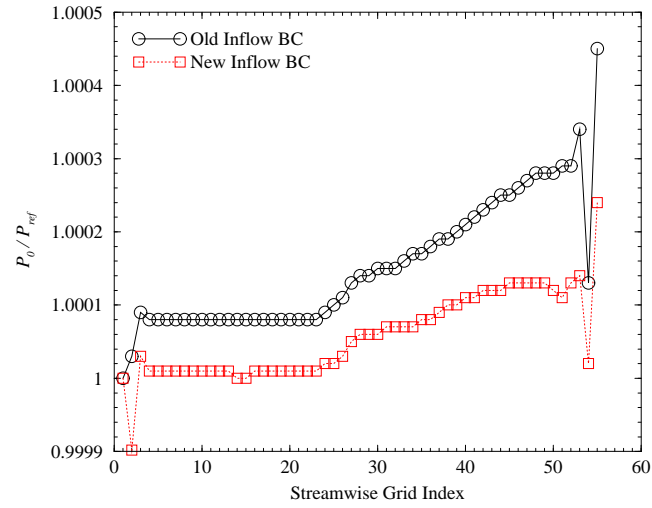Figure 7.5: Normalized total pressure field variations with inflow boundary condition treatment

Figure 7.6: Effect of inflow boundary condition treatment on normalized total pressure
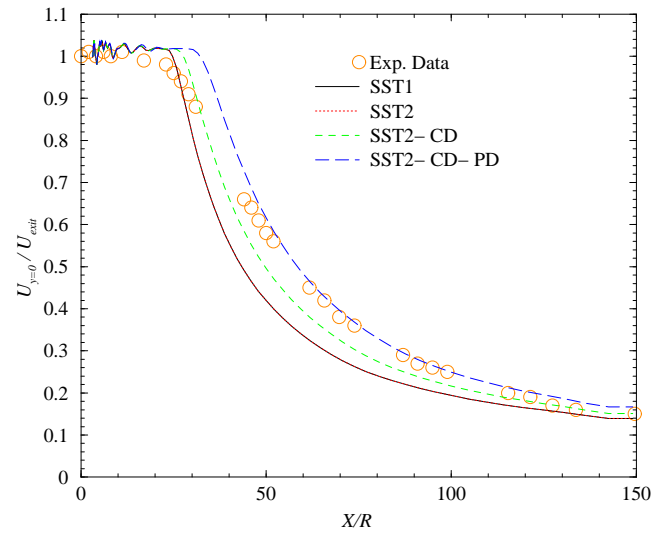

Figure 7.7: Effect of compressibility corrections on predictions of centerline velocity in an axi-symmetric nozzle
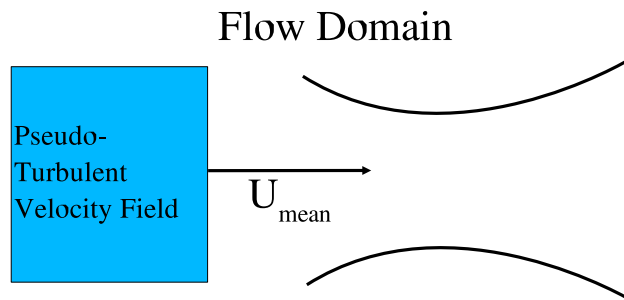
101

Figure 7.8: Schematic of the pseudo-turbulent unsteady inflow boundary condition

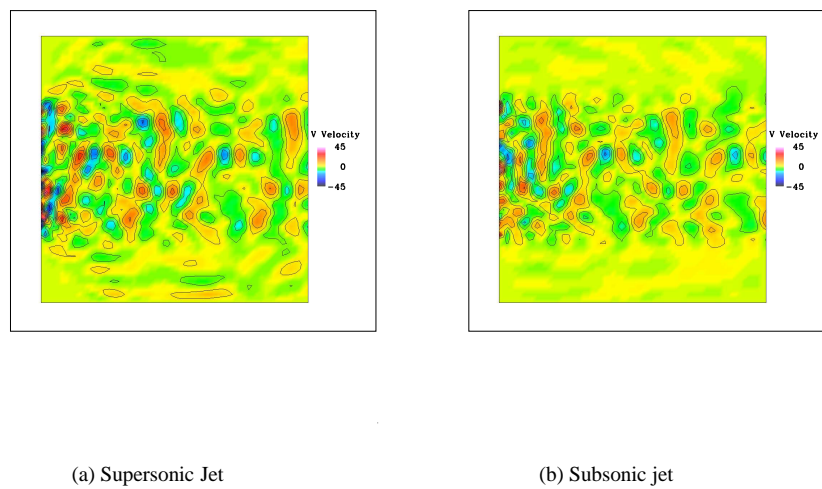
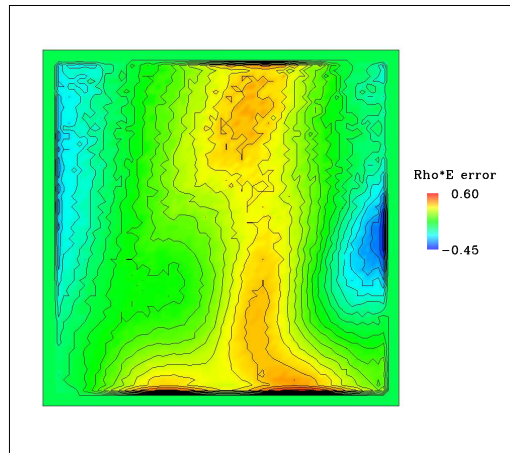(a) Supersonic Jet

(b) Subsonic jet

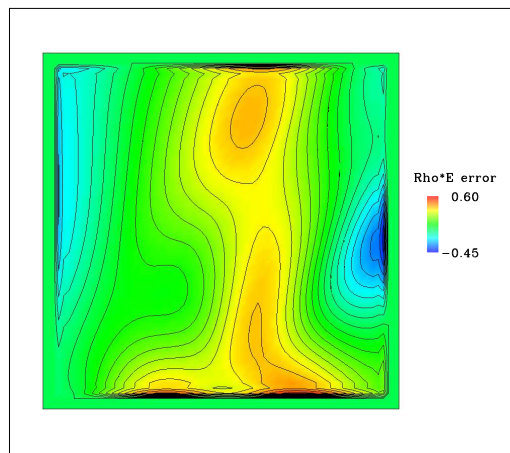Figure 7.9: V component of velocity in a 2-D turbulent jet case with pseudo-turbulent inflow (flow from left to right)

(a) Single Precision Solver

(b) Double precision solver

Figure 7.10: Effect of precision on the error in total energy in a Method of Manufactured Solutions case on a 64^3 grid

103
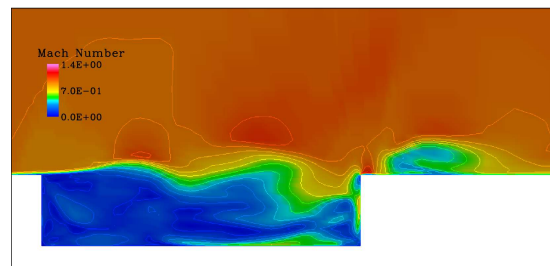
(a) Nichols and Nelson hybrid model
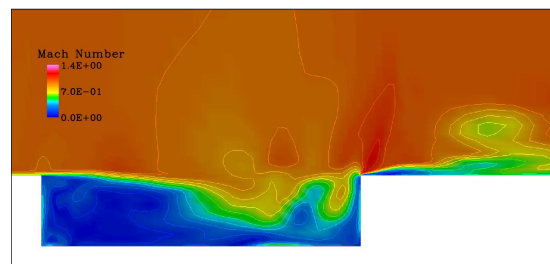
(b) DES model

Figure 7.11: Contours of Mach number in unsteady WICS bay simulations
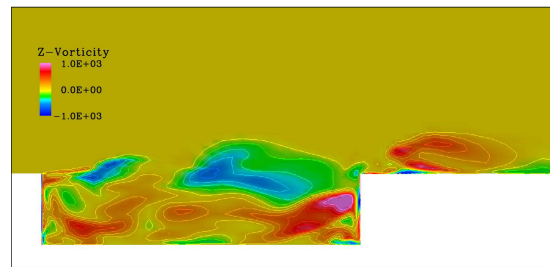
(a) Nichols and Nelson hybrid model
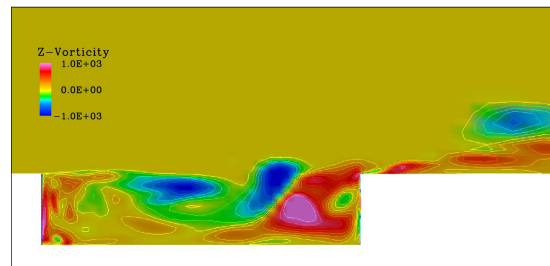
(b) DES model

Figure 7.12: Contours of the Z-component of vorticity in unsteady WICS bay simulations

(a) Nichols and Nelson hybrid model

(b) DES model

Figure 7.13: Contours of turbulent viscosity in unsteady WICS bay simulations

(a) Bottom wall X/L = 0.985

(b) Back Wall Z/L = 0.85

Figure 7.14: Sound pressure level along bay centerline in unsteady WICS bay simulations

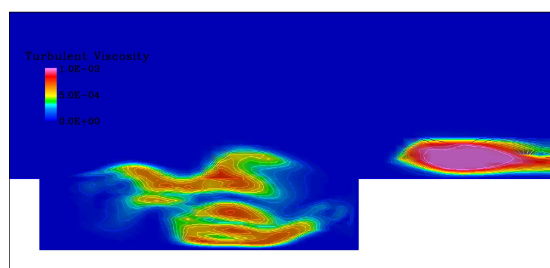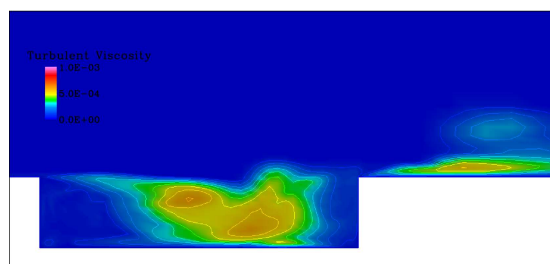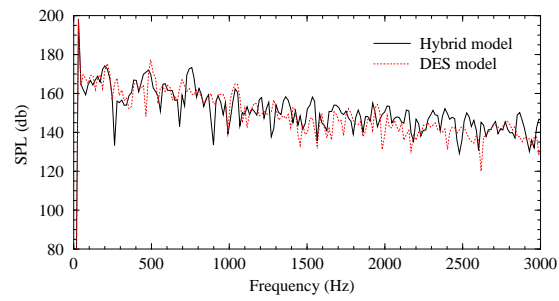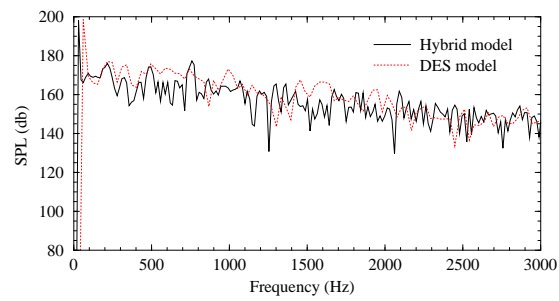# Chapter 8

Prediction of Diffuser Instability

It is believed that the major contributing factor to the unsteadiness experienced in the 16-S wind tunnel at AEDC is intermittent instability in the diffuser section between corner three and corner four (see Fig. 8.1). This sort of instability has been seen in the past in other facilities. It thus represents a class of facility problems that would have to be numerically resolvable in order to have a reasonably general facility unsteadiness simulation capability. The following cases have been undertaken in order to pave the way toward (the capability for) simulations of the full 16-S tunnel benchmark case.

8.1   Steady State Runs

Experimentally, flow in diffusers has been observed to be completely attached, intermittently separating, or continually separated, depending on the length of the diffuser and the spreading angle. The intention in this project is to simulate various data points (shown in Fig. 8.2) to determine if CFD can match the experimentally observed behavior. As a first step in this direction, several two-dimensional axi-symmetric steady-state cases have been run. The intention is to determine whether or not the Wind-US code has the capability to capture the most basic aspects of the physics. If the code cannot capture at least the steady-state aspects of these diffusers, then it is doubtful that an unsteady simulation could yield much useful information.

   The results from steady state runs were extremely encouraging. Cases four and five, which should be in the fully attached region, do in fact show fully attached flow as shown in Figs. 8.3 and 8.4. The cases which should have large separation regions, are also correctly predicted (see Figs. 8.5 and 8.6). Most interesting of all is the case that straddles the stall line; this case, when examined in detail (see Fig. 8.7), shows incipient separation, just as it should. Thus, Wind-US has been validated to at least be able to capture the basic steady-state flow features in these diffusers.

8.2   2-D Simpli ed   16-S Tunnel Model

In another effort to assess the ability of Wind-US to meet the requirements for this project, a simplified, 2-D grid of the 16-S tunnel was created. This grid runs from "valve 80" through the test section (see Fig. 8.1), but is purely two dimensional and does not include any turning vanes or screens. Obviously, in such a configurations, one expects separation at the corners, and the results will bear little relation to what occurs in the actual tunnel. The objective of this case, however, is not to model 16-S, per se, but to determine if the code can support unsteadiness sufficiently that the fluctuations due to the separation at corner four is detectable in the test section. The results using the default (second order in space) scheme indicate that some unsteadiness is being predicted, and that some of this unsteadiness appears to be surviving into the test section. The magnitude of pressure variation with time at points along the wall of the test section is on the order of 0.03 psi (out of approximately 1.5 psi). Figure 8.8 shows contours of the Z-component of vorticity for a case run with the DES model compared with a steady-state case run with Menter's SST model. The unsteady case clearly shows some vortices being shed at Corner 3, but these seem to be damped out rather quickly.

8.3   Axi-Symmetric Simpli ed   16-S Tunnel Model

A second simplified version of the 16-S tunnel was created in an effort to address the shortcomings of the above test case. The new version uses a 2-D axi-symmetric grid which consists of the diffuser leg, stilling chamber, and test section attached in a straight line. This is roughly equivalent to assuming that the turning vanes perform perfectly and turn the flow with no losses whatsoever. It also changes the nozzle and test section cross-sections from rectangular to circular. One immediate result of this is that the area ratios of the nozzle are no longer appropriate for Mach 1.6 flow and instead yield Mach numbers of roughly 1.9 in the test section.

Despite these drawbacks, if, as is believed, the diffuser is unstable, this case should be sufficient to capture some degree of unsteadiness and propagate it downstream to the test section (subject to the limitations of the numerics). Using this case, therefore, it should be possible to obtain an estimate of what a comparable 3-D case would require in terms of computational resources (due to grid resolution requirements and time step limitations).

Mach number contours for this case are shown in Figure 8.9. From this plot, it would seem that no noticeable unsteadiness is being predicted in this case. When the details of the flow in the diffuser section are examined, however, one can see, intermittently, separation bubbles forming, bursting, and then reforming. The intensity of the separation is not as extreme as that observed in the subscale tunnel experiment, but it is very encouraging nonetheless. The region of reverse flow during one of these episodes of separation is shown in Figure 8.10.

The contours of the Z-component of vorticity in Figure 8.11 show how the pseudo-turbulent fluctuations being injected at the inflow are propagating through the domain. Also visible are the larger vortical structures being shed from the diffuser wall and

propagated downstream. The scale of plot has been greatly truncated so as to highlight the freestream turbulence, which is relatively weak: inflow streamwise turbulent intensity is two percent of the freestream velocity. Also note that the behavior is different than observed in Figure 7.9 in that long streaks of vorticity can be seen in the streamwise direction. At least some of these differences are due to the pseudo-turbulent inflow being designed for either true 2-D or full 3-D simulations, not axi-symmetric flows such as this one. The varying circumference as one changes radial location will distort the development of the unsteady flow relative to what one would expect in a pure two-dimensional case.

The effect of these fluctuations has been measured at the end of the nozzle (start of the test section). Traces of streamwise velocity and static pressure at the centerline are shown in Figures 8.12 and 8.13, respectively. Since the overall fluctuations observed in the diffuser were smaller and less intense than that observed in the tunnel, it is no surprise that the magnitude of the fluctuations observed in the test section should be small as well. Nevertheless, it is highly encouraging to see that these relatively weak structures are in fact propagated through the stilling chamber and can be detected in the test section some two hundred feet downstream.
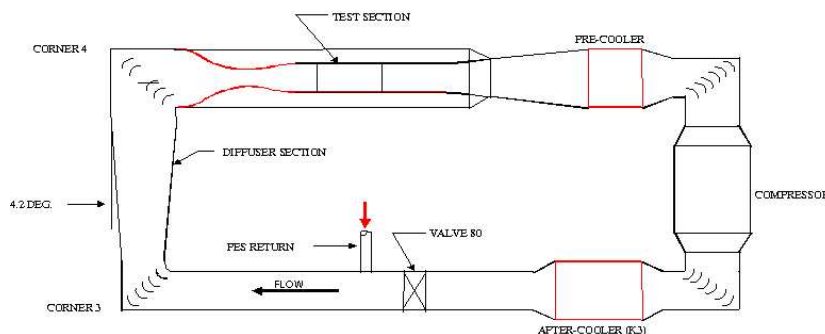

Figure 8.1: Schematic of the AEDC 16-S Wind Tunnel
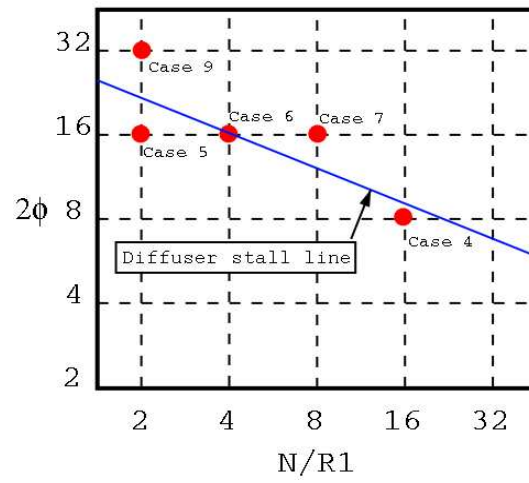
Figure 8.2: Observed Stability Characteristics of Diffusers

Figure 8.3: Contours of velocity magnitude predicted for the Case 4 diffuser

111
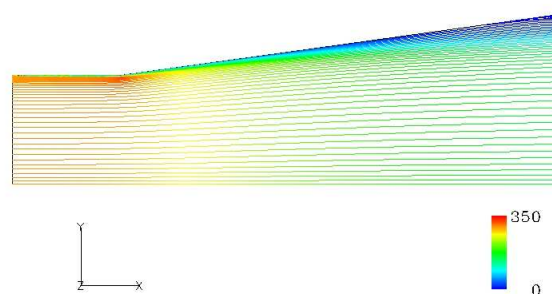
Figure 8.4: Contours of velocity magnitude predicted for the Case 5 diffuser

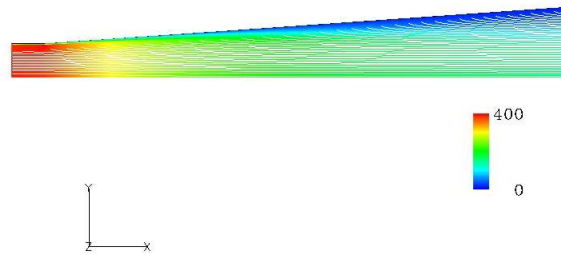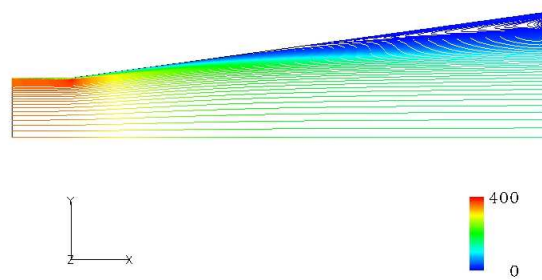Figure 8.5: Contours of velocity magnitude predicted for the Case 7 diffuser
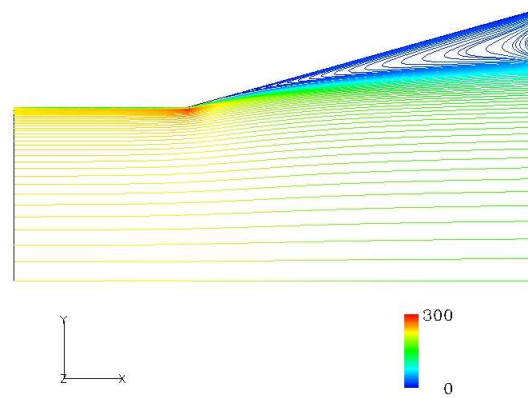
Figure 8.6: Contours of velocity magnitude predicted for the Case 9 diffuser
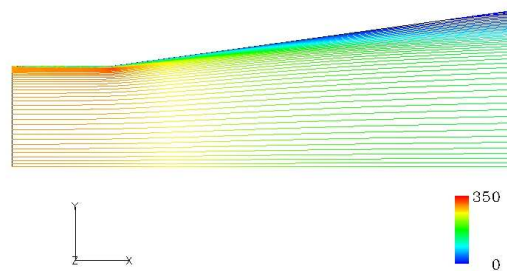
(a) Full domain
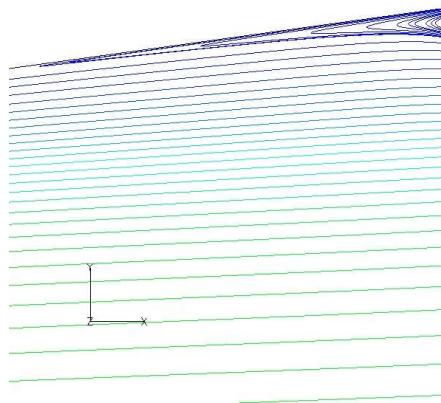
(b) Detail of separated region

Figure 8.7: Contours of velocity magnitude predicted for the Case 6 diffuser

114
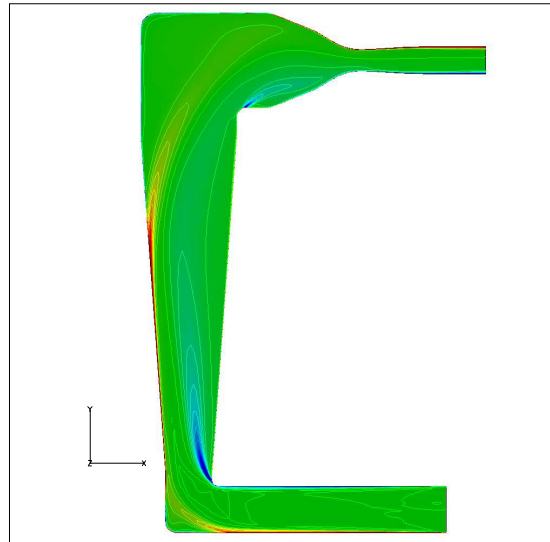
(a) Steady state run (SST model)
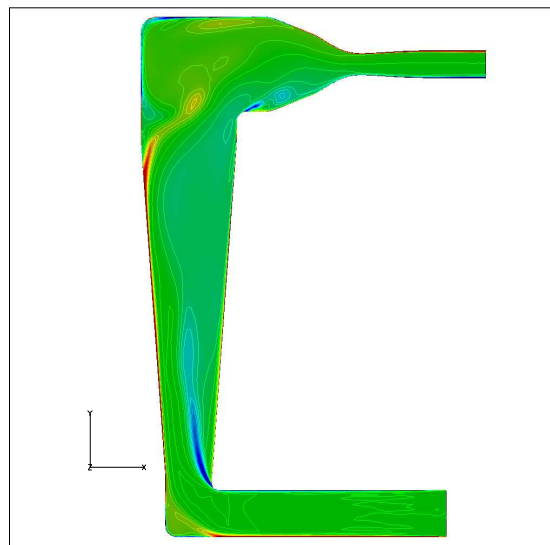
(b) Unsteady run (DES model)

Figure 8.8: Contours of Z vorticity in a simplified 2-D model of 16-S
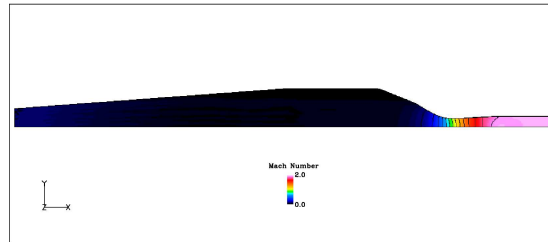
Figure 8.9: Contours of Mach number in a simplified axi-symmetric model of 16-S
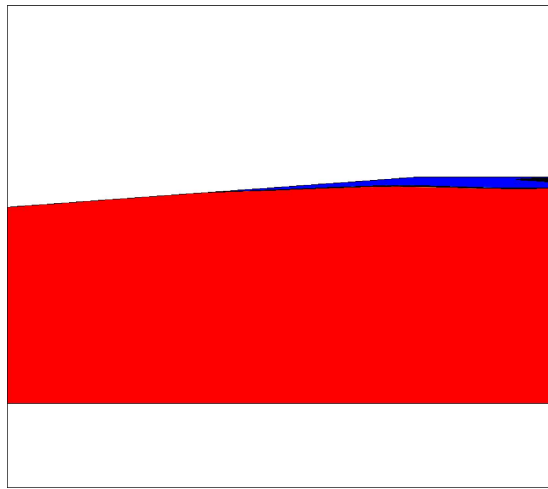
Figure 8.10: Regions of reverse flow (blue) at a given instant in a simplified axi-symmetric model of 16-S
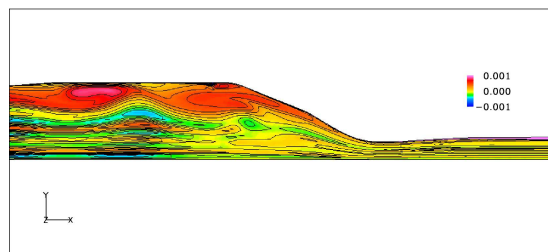
Figure 8.11: Contours of Z-vorticity in a simplified axi-symmetric model of 16-S

116
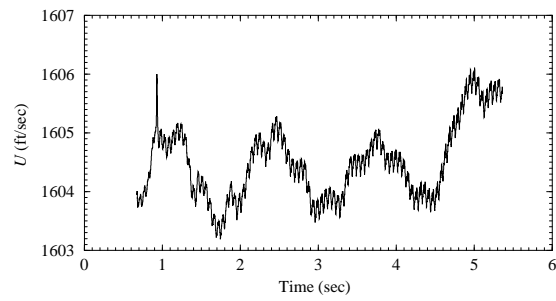
Figure 8.12: Trace of streamwise velocity in the test section of a simplified axi-symmetric model of 16-S
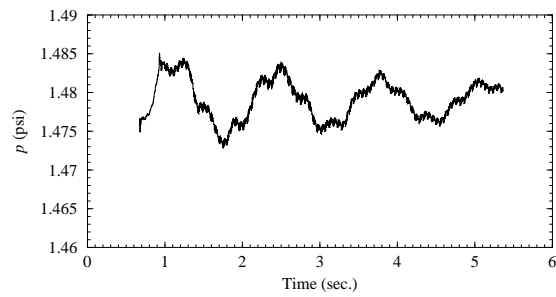
Figure 8.13: Trace of static pressure in the test section of a simplified axi-symmetric model of 16-S

117

Chapter 9

Conclusions and Recommendations

The Facility Unsteadiness Research project has resulted in a much-improved ability to use CFD to predict unsteadiness in large scale ground test facilities. The capabilities thus developed have been transitioned to the Wind-US code for wider use by the Air Force and other DoD-related organizations. This government code continues to be developed and maintained, providing some assurance that these capabilities will continue to be available to the DoD community.

This work has shown, among other things, that the basic ideas of hybrid RANS/LES turbulence models are at least in some sense correct. Specifically, by transitioning from a RANS modeling approach in regions that are under-resolved by the computational grid to an LES-type model where the grid is suitably dense, dramatic improvements are possible in the accuracy of unsteady simulations. This is true for the two models discussed in this work (DES and the hybrid model), but there is not reason to believe it would not also be true for other approaches. Furthermore, it appears that, at least for the mixing layer simulations discussed above, the differences between the two approaches were minimal, with no clear "winner" yet in sight. Combined with the analysis which showed that boundary location and statistical gathering methods have as much or more effect, it becomes obvious that expending more time and effort on tweaking hybrid models would be counterproductive, at least for the purposes of pursuing large scale unsteady simulations. The one exception to this would be in the area of the transition between RANS and LES modes. The difficulties encountered with the DES model when a dense computational grid is present, but little or no unsteadiness is encountered indicate that perhaps some modification to the switch between RANS and LES modes would be in order. The hybrid model of Nichols and Nelson has shown a somewhat more robust response to the same situation, but more work is required in order to determine if that was merely fortuitous or if it represents an advantage of this approach over that taken in the DES model.

The infrastructure improvements documented above that have taken place within the Wind-US code have resulted in a much more robust code and a better platform for

further development. The improved time marching, in particular, has resulted in at least an order of magnitude improvement in turn-around time for unsteady cases. The use of the Method of Manufactured Solutions and the various test suites has proved to be an extremely useful technique for maintaining confidence in the code as changes are made.

The diffuser test cases that were run have shown that the Wind-US code is capable of matching the observed separation in diffusers in a steady-state sense. The improved unsteady capability has also been put to use in simulations of the WICS bay and simplified versions of the 16-S wind tunnel geometry. The results from the WICS bay simulations are in reasonable agreement with the findings of other researchers.

The simplified 16-S simulations indicate that the instability can be captured in such a large facility and propagated for significant distances while remaining detectable. This suggests that with a full three-dimensional grid with somewhat more resolution in the center of the duct, the associated 3-D instability modes and 3-D pseudo-turbulent inflow fluctuations could resolve the large scale unsteadiness in facilities such as the 16-S tunnel. Using the technology developed and/or demonstrated in this work, a simulation of the diffuser, stilling chamber, nozzle, and test section would require a grid with an estimated 20-30 million grid points. Running such a large grid for the required 10^5 timesteps (in order to wash out initial conditions and gather sufficient data to allow statistically meaningful time averaging) would obviously require significant computational resources. Such resources exist, however, at the DoD's Major Shared Resource Centers, and similar sized cases are not unheard of. Thus, while time-accurate simulations of large facility unsteadiness are not yet within the reach of everyday production CFD, there is now evidence that suggests these simulations are within the reach of large computer facilities.

With this demonstrated basic unsteady capability in place, future work can now proceed toward refining it and implementing more specialized technologies needed for particular projects. For large scale test facility simulations in particular, the addition of verified high-resolution numerical schemes (better than the current fifth order upwind-biased schemes already present) would be greatly beneficial, as it would result in anywhere from two to eightfold improvement in grid resolution requirements for 3-D cases and thus substantially reduce the cost of such simulations.

Bibliography

[1] Hanjalic, K., Launder, B., and Schiestel, R., "Multiple-time-scale concepts in turbulent shear flows," *Turbulent Shear Flows 2*, Springer-Verlag, 1980, pp. 36–49.

[2] Kim, S.-W. and Chen, C.-P., "A multiple-time-scale turbulence model based on variable partitioning of turbulent kinetic energy spectrum," AIAA Paper 88–0221, 1988.

[3] Duncan, B. and Liou, W., "A Multiple-Scale Turbulence Model for Incompressible Flow," AIAA Paper 90–0086, 1993.

[4] Spalart, P. R. and Allmaras, S. R., "A One-Equation Turbulence Model for Aerodynamic Flows," AIAA Paper 92–0439, 1992.

[5] Spalart, P. R., Jou, W.-H., Strelets, M., and Allmaras, S. R., "Comments on the Feasibility of LES for Wings and on a Hybrid RANS/LES Approach," *Advances in DNS/LES- Proceedings of the First AFOSR International Conference on DNS/LES*, 1997.

[6] Menter, F. R. and Rumsey, C. L., "Assessment of Two-Equation Turbulence Models for Transonic Flows," AIAA Paper 1994–2343, 1994.

[7] Strelets, M., "Detached Eddy Simulation of Massively Separated Flows," AIAA Paper 2001-0879, 2001.

[8] Nichols, R. and Nelson, C., "Spatially filtered RANS turbulence model for unsteady flow," Memo for record, Arnold Engineering Development Center, 1999.

[9] Menter, F., "Two-equation eddy-viscosity turbulence models for engineering applications," *AIAA Journal*, Vol. 32, No. 8, 1994, pp. 1598–1605.

[10] Jones, W. P. and Launder, B. E., "The Prediction of Laminarization with a Two-Equation Model of Turbulence," *International Journal of Heat and Mass Transfer*, Vol. 15, 1972, pp. 301–314.

[11] Nelson, C. and Menon, S., "Unsteady Simulations of Compressible Spatial Mixing Layers," AIAA Paper 98–0786, 1998.

[12] Durbin, P. A., "A Perspective on Recent Developments in RANS Modeling," *Proceedings of the Fifth International Symposium on Engineering Turbulence Modeling and Measurements*, 2002, pp. 3–16.

[13] Piomelli, U., Balaras, E., Squires, K. D., and Spalart, P. R., "Interaction of the Inner and Outer Layers in Large-Eddy Simulations with Wall-Layer Models," *Proceedings of the Fifth International Symposium on Engineering Turbulence Modeling and Measurements*, 2002, pp. 307–316.

[14] Nichols, R. H. and Nelson, C. C., "Application of Hybrid RANS/LES Turbulence Models," AIAA Paper 2003–0083, 2003.

[15] Sarkar, S. and Balakrishnan, L., "Application of a Reynolds stress turbulence model to the compressible shear layer," Tech. Rep. ICASE 90-18, Institute for Computer Applications in Science and Engineering, 1990.

[16] Mankbadi, R., Hixon, R., and Povinelli, L., "Very Large Eddy Simulations of Jet Noise," AIAA Paper 2000–2008, 2000.

[17] Samimy, M. and Elliott, G. S., "Effects of Compressibility on the Characteristics of Free Shear Layers," *AIAA Journal*, Vol. 28, No. 3, 1990, pp. 439–445.

[18] Nelson, C., *Simulations of spatially evolving compressible turbulence using a local dynamic subgrid model*, Ph.D. thesis, Georgia Institute of Technology, 1997.

[19] Papamoschou, D. and Roshko, A., "The Compressible Turbulent Shear Layer: an Experimental Study," *Journal of Fluid Mechanics*, Vol. 197, 1988, pp. 453–477.

[20] Goebel, S. G. and Dutton, J. C., "Experimental Study of Compressible Turbulent Mixing Layers," *AIAA Journal*, Vol. 29, No. 4, 1991, pp. 538–546.

[21] Elliott, G., *A Study of Compressible Mixing Layers Using Laser Based Diagnostic Techniques*, Ph.D. thesis, The Ohio State University, 1993.

[22] Nichols, R. H., *The Effect of Particle Dynamics on Turbulence Measurements with the Laser Doppler Velocimeter*, Ph.D. thesis, University of Tennessee, Knoxville, 1986.

[23] Nelson, C. C. and Nichols, R. H., "Evaluation of Hybrid RANS/LES Turbulence Models Using an LES Code," AIAA Paper 2003–3552, 2003.

[24] Samimy, M., Erwin, D. E., and Elliott, G. S., "Compressibility and Shock Wave Interaction Effects on Free Shear Layers," *AIAA-89-2460*, 1989.

[25] Samimy, M. and Elliott, G. S., "Effects of Compressibility on the Structure of Free Shear Layers," *AIAA-88-3054A*, 1988.

[26] Nichols, R. and Tramel, R., "Applications of a Highly Efficient Numerical Method for Overset-Mesh Moving Body Problems," AIAA Paper 97–2255, 1997.

[27] Jones, G. W., Cincotta, J. J., and Walker, R. W., "Aerodynamic Forces on a Stationary and Oscillating Circular Cylinder at High Reynolds Number," NASA TR R-300, 1968.

[28] Roshko, A., "Experiments on the Flow Past a Circular Cylinder at Very High Reynolds Number," *Journal of Fluid Mechanics*, Vol. 10, No. 3, 1961, pp. 345–356.

[29] Schlichting, H., *Boundary Layer Theory*, McGraw-Hill, New York, 7th ed., 1979.

[30] Piziali, R. A., "2-D and 3-D Oscillating Wing Aerodynamics for a Range of Angles of Attack Including Stall," NASA TM 4632, NASA Ames Research Center, 1994.

[31] Dix, R. E. and Bauer, R. C., "Experimental and Theoretical Study of Cavity Acoustics," AEDC TR 99-4, Arnold Engineering Development Center, 2000.

[32] Roache, P. J. and Steinberg, S., "Symbolic Manipulation and Computational Fluid Dynamics," *AIAA Journal*, Vol. 22, No. 10, 1984, pp. 1390–1394.

[33] Roach, P. J., Knupp, P. M., Steinberg, S., and Blaine, R. L., "Experience with benchmark test cases for groundwater flow," *Benchmark Test Cases for Computational Fluid Dynamics*, edited by I. Celik and C. J. Freitas, No. H00598 in ASME FED 93, 1990, pp. 49–56.

[34] Oberkampf, W. L. and Blottner, F. G., "Issues in Computational Fluid Dynamics Code Verification/Validation," *AIAA Journal*, Vol. 36, No. 5, 1998, pp. 687–695.

[35] Salari, K. and Knupp, P., "Code verification by the method of manufactured solutions," Tech. Rep. SAND2000-1444, Sandia National Laboratories, 2000.

[36] Bush, R. H., "A Three Dimensional Zonal Navier-Stokes Code for Subsonic Through Hypersonic Propulsion Flowfields," *AIAA-88-2830*, 1988.

[37] Bush, R. H., Power, G. D., and Towne, C. E., "WIND: The Production Flow Solver of the NPARC Alliance," AIAA Paper 98–0935, 1998.

[38] Power, G. D. and Underwood, M. L., "WIND 2.0- Progress on an Applications-Oriented CFD Code," AIAA Paper 99–3212, 1999.

[39] Roy, C. J., Nelson, C. C., Smith, T. M., and Ober, C. C., "Verification of Euler/Navier-Stokes Codes Using the Method of Manufactured Solutions," *to appear in The International Journal of Numerical Methods in Fluids*, 2004.

[40] Buning, P. G., Jespersen, D. C., Pulliam, T. H., Klopfer, G. H., Chan, W. M., Slotnick, J. P., Krist, S. E., and Renze, K. J., *OVERFLOW User's Manual- Version 1.8q*, August 2000.

[41] Suzen, Y. B. and Hoffman, K. A., "Investigation of Supersonic Jet Exhaust Flow by One- and Two-Equation Turbulence Models," AIAA Paper 98–0322, 1998.

[42] Eggers, J. M., "Velocity Profiles and Eddy Viscosity Distributions Downstream of a Mach 2.22 Nozzle Exhausting to Quiescent Air," Tech. Rep. TN D–3601, NASA, 1966.

[43] Barber, T. J., Chiappetta, L. M., DeBonis, J. R., Georgiadis, N. J., and Yoder, D. A., "An Assessment of Parameters Influencing Prediction of Shear Layer Mixing," *AIAA-97-2639*, 1997.

[44] Soteriou, M. C. and Ghoniem, A. F., "Effects of the Free-Stream Density Ratio on Free and Forced Spatially Developing Shear Layers," *Physics of Fluids*, Vol. 7, No. 8, 1995, pp. 2036–2051.

[45] Comte, P., Lesieur, M., Laroche, H., and Normand, X., "Numerical Simulations of Turbulent Plane Shear Layers," *Turbulent Shear Flows 6*, Springer-Verlag, 1989, pp. 360–380.

[46] Comte, P., Fouillet, Y., Gonze, M.-A., Lesieur, M., Metais, O., and Normand, X., "Generation of Coherent Structures in Free Shear Layers," *Turbulence and Coherent Structures*, Kluwer Academic Publishers, 1991, pp. 45–73.

[47] Sekar, B. and Mukunda, H. S., "A Computational Study of Direct Simulation of High Speed Mixing Layers Without and With Chemical Heat Release," *Proceedings of the 23rd International Symposium on Combustion*, 1990, pp. 707–713.

[48] Lele, S. K., "Direct Numerical Simulation of Compressible Free Shear Flows," *AIAA-89-0374*, 1989.

[49] LeBoeuf, R. L., "Forced Free-Shear Layer Measurements," *Center for Turbulence Research- Annual Research Briefs 1994*, 1994, pp. 313–338.

[50] Akselvoll, K. and Moin, P., "Large-Eddy Simulation of Turbulent Confined Coannular Jets," *Journal of Fluid Mechanics*, Vol. 315, 1996, pp. 387–411.

[51] Oh, C. K. and Loth, E., "Unstructured Grid Simulations of Spatially Evolving Supersonic Shear Layers," *AIAA Journal*, Vol. 33, No. 7, 1995, pp. 1229–1238.

[52] Schwer, D. A., Tsuei, H.-H., and Merkle, C. L., "Computation and Validation of Spatially Reacting Mixing Layers," *AIAA-95-0261*, 1995.

[53] Lee, S., Lele, S. K., and Moin, P., "Simulation of Spatially Evolving Turbulence and the Applicability of Taylor's Hypothesis in Compressible Flow," *Physics of Fluids A*, Vol. 4, No. 7, 1992, pp. 1521–1530.

[54] Batten, P., Goldberg, U., and Chakravarthy, S., "Using Synthetic Turbulence to Interface RANS and LES," AIAA Paper 2003–0081, 2003.

[55] Keating, A. and Piomelli, O., "Sythetic Generation of Inflow Velocities for Large-Eddy Simulation," AIAA Paper 2004–2547, 2004.

[56] Lee, S., Lele, S. K., and Moin, P., "Eddy Shocklets in Decaying Compressible Turbulence," *Physics of Fluids A*, Vol. 3, No. 4, 1991, pp. 657–664.